Zenithal bistable display:
avenues for improved performance
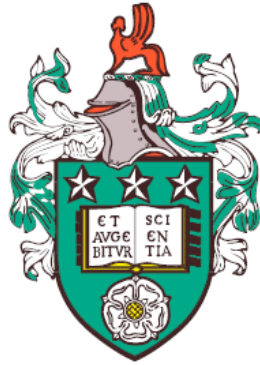
Sophie Ann Jones

University of Leeds

School of Physics and Astronomy

Submitted in accordance with the requirements for the degree of

Doctor of Philosophy

June 2019

The candidate confirms that the work submitted is her own, except where work which has formed part of jointly authored publications has been included. The contribution of the candidate and the other authors to this work has been explicitly indicated below. The candidate confirms that appropriate credit has been given within the thesis where reference has been made to the work of others.

Acknowledgements

This work would not have been possible without Professor Cliff Jones, for his support an endless ideas, and not least for his role in the invention of the device studied. Thanks to my industrial supervisor Dr Guy Bryan-Brown for his expertise and to DisplayData Ltd. for sponsoring my PhD.

This research was helped enormously by collaborations with researchers in other fields and outside the university. I would like to thank Professor Sally Day and Dr Anibal Fernandez at UCL for their their help with the computational aspect of this work. I would also like to thank Dr Richard Mandle and his colleagues at the University of York for the synthesis of materials used in the research. Special thanks to Dr Mark Rosamond from the School of Electronic and Electrical Engineering here at Leeds, who was instrumental in our fabrication of small scale gratings. Additional thanks to Drs Ben Johnson and Peng Bao for their help with experiments.

The soft matter physics group at Leeds is large and composed entirely of wonderful people, past and present, who are always on hand for helpful discussions, proof reading, and sanity checks. Thanks to the denizens of 9.64c, Edgar Simmons, Ethan Jull, Peter Wyatt, Rowan Morris, Shajeth Srigengan, Yunhao Liang, James Hawkins, Adam O'Connell, and Zachary Gradwell; to Drs Stephen Green, Ben Hanson, Matt Reynolds, Devesh Mistry, James Bailey, and Dan Baker; and to Dr Mamatha Nagaraj and Professor Helen Gleeson. Special thanks must go to Glenys Bowles, honorary group member, for her ceaseless support.

A final thank you to my family and friends for all of their encouragement these past three years.

Abstract

Four distinct, interconnected research projects were undertaken with the goal of improving performance in the zenithal bistable device with new display applications in mind. ZBD is a commercially successful bistable nematic liquid crystal device used in small scale retail signage. Some of the physics of the device are as yet unexplored or at least unreported due to the commercial nature of the technology. In addition, there remains much room to improve upon the existing device by refining materials and structure.

The device was examined and iterated upon through experimental and computational means. Test devices were fabricated through standard liquid crystal cell techniques, plus grating structure embossing and controlled surface treatment. New grating shapes were trialled, replicating from etched Si masters. Novel materials were introduced into high-performance display mixtures to lower operating voltages. Test samples of each: controlled surface treatment to the grating, new grating shapes, and new liquid crystal mixtures, were evaluated by their performance in bistable latching. Computational modelling software was used to examine, in detail, defect dynamics at the latching transitions.

Controllable anchoring strength at the micron-scale grating was achieved through vapour-phase silane deposition, tuneable within $0.5 - 2 \times 10^{-4}$ J/m^2. This was found to be well correlated with molecular silane density at the surface through X-ray photo-electron spectroscopy. Control of the anchoring strength at the grating surface provides

control over the device itself, with a direct impact on the latching voltages. The defect dynamics during latch were identified, including those dynamics responsible for unique latching behaviours found in experiments. These included a suppressed latch regime in continuous to defect latching, caused by the nucleation of further defect pairs; RMS latching, investigated through the removal of the flexoelectric terms in the modelling and compared to experiment; and the reverse latch, found while examining the speed of defect movement under electric field. These largely-computational results provide good correlation to experimental behaviour but are not numerically accurate. The addition of bent liquid crystal dimers to an existing display mixture indicated potential for lower operating voltages through flexoelectric doping. Successful latching was performed from one bistable state to the other in sub-micron scale gratings, although the latch in reverse was not seen. Latching was only achieved on 400 nm pitch gratings, and not 300 nm. Full bistability remains a possibility at this scale should the appropriate steps be taken.

The work of this thesis when taken together presents the zenithal bistable device as a technology with untapped potential. Fabrication methods for the device can be readily extended to other device structures for liquid crystals; physical phenomena can be intuited using the device as a defect playground; material developments can improve upon device performance; and new gratings at much lower scale represent a solution to optical losses which will open up new avenues for display and optical applications.

Contents

CONTENTS

List of Figures

Abbreviations

[ ]	Concentration (of material enclosed)
$\mathbb{1}$	3×3 identity matrix
5CB	4-Cyano-4'-pentylbiphenyl, a nematic liquid crystal
a	First Landau-de Gennes thermotropic coefficient
A	A fitting constant for latching impulses
ABD	Azimuthal bistable device
AFM	Atomic force microscopy
AP	Adhesion promoter
AR	Aspect ratio
b	Second Landau-de Gennes thermotropic coefficient
B	A fitting constant for latching impulses
BiNem	Commercial name for the 0-π bistable nematic device
c	Third Landau-de Gennes thermotropic coefficient
C	Continuous state of the zenithal bistable device
C8	Trichloro-octyl silane
d	Cell gap
D	Defect state of the zenithal bistable device
DC	Direct current
DI	Deionised (water)
e	Flexoelectric coefficients
E	Electric field
E-beam	Electron beam lithography
F	Free energy
FWHM	Full width half maximum
g	Grating vector
HAN	Hybrid aligned nematic

I-beam	Ion beam lithography
IPA	Isopropanol
ITO	Indium tin oxide
k	Fitting parameter
K	Elastic constant
LC	Liquid crystal
LCD	Liquid crystal display
l_s	Liquid slip parameter
M	Mass
MaCE, MacEtch	Metal-assisted chemical etching
n	Refractive index
$\boldsymbol{n}$	Nematic director
N_{tb}	Nematic twist bend phase
$\boldsymbol{P}$	Polarisation vector
PABN	Post-aligned bistable nematic device
PDMS	Polydimethylsiloxane
POM	Polarised optical microscopy
PPA, PPB	Photopolymer A and B, weak and strong proprietary photopolymers by DisplayData
PP2	Photopolymer 2
Q	Q-tensor, tensorial order parameter
QLC3D	Liquid crystal Q-tensor finite element modelling program
RIE	Reactive ion etching
RMS	Root mean square
S	Orientational order parameter
SEM	Scanning electron microscopy
STN	Super twist nematic
t	Time
T	Temperature
TFT	Thin film transistor
TMPTMA	Trimethylolpropane trimethacrylate

TN   Twisted nematic

T_{NI} Nematic to isotropic phase transition temperature

V   Voltage

VAN   Vertically aligned nematic

V_{th} Threshold voltage

W   Anchoring strength

XPS   X-ray photoelectron spectroscopy

ZBD   Zenithal bistable device

γ Rotational viscosity

Γ Retardation

$\Delta\epsilon$ Dielectric anisotropy

Δn Birefringence

ϵ Dielectric constant

ϵ_o Vacuum permittivity

λ Wavelength

τ Pulse duration

LIST OF FIGURES

Chapter 1

Introduction

1.1 Motivation

Liquid crystals (LCs) are materials at the forefront of switchable opto-electronics, displays in particular. Their adoption led to the viability of the flat panel and truly portable displays now ubiquitous in our lives, from TVs and laptops, to smart phones and watches. Nematic LCs are paramount to this technology, with wide operating temperatures, shock stability, and low voltage operation.

Bistability in nematic liquid crystal displays can compound this low voltage operation, offering shock-stable image storage for applications in which static images are prominent or else power consumption is a limiting factor. These include portable displays such as e-readers and smart watches as well as shelf edge labels. Many different technologies exist in this vein, the most commercially successful of these being the zenithal bistable display (ZBD).

The ZBD is a commercial technology distributed by DisplayData that uses a micron scale grating on one substrate to support two stable alignments. This grating enables bistability in the device but also leads to optical and electrical losses. It is the goal of this thesis to first, characterise operation of the device, and second, improve performance of the display. Specifically, the work was done to target a single polariser mode ZBD and devices which utilise two grating surfaces. If the technology can be suitably modified, these two device configurations

would provide superior optical quality for commercial devices.

Both experimental and computational methods were chosen to complete the work, in four distinct but interconnected projects. The primary mode of experiment was that of electrical evaluation of ZBD cells. This is performed on a standard polarised optical microscope using a display-oriented function generator. Device production is studied from the ground up, from grating fabrication to cell assembly. Finite element modelling using pre-written software provides a more detailed understanding of the latching dynamics.

1.2   Summary of results

Work described in this thesis concentrates on bistable latching in the zenithal bistable display. Four main projects can be identified in two aspects:

1. Device characterisation

This first aspect looks at the existing device in its commercial form. A wealth of literature exists on the development of this technology (see Chapter 3) but many specifics are omitted due to the commercial nature of the device. Homeotropic alignment at the grating surface gives the bistability profile of the device; part of the characterisation work presents a reliable method of treating grating surfaces of a known photopolymer. Making use of a known photopolymer opens up the technology to use by other researchers for further study. At the same time, this method sidesteps issues with proprietary materials and is also applicable to other liquid crystal technologies which require homeotropic anchoring at microstructures.

Computational modelling is also performed on the device. The program used was developed at UCL and is operable on standard computer hardware, forgoing the need for high powered computing. The modelling work focuses specifically

on defect dynamics in the device and unique latching modes. The defect dynamics are known theoretically, but the use of computational modelling allows for more thorough investigation of the intricacies in the physics. The unique latching modes discussed have been noted before, but have rarely been included in literature due to their status in the device: typically these modes are to be avoided in standard operation, so the literature regards how to mitigate their effects rather than understand their physical origin.

2. Device modification

The second aspect looks at two modifications to the device which present avenues for improvement in ZBD. Bent liquid crystal dimers are of particular interest in the literature at present due to investigations of the twist-bend nematic phase and of unique flexoelectric properties. Use of these bent dimers in LC mixtures has potential for lower operating voltages and indicates that further work into mixtures could give further improvements.

An exploration into the effect of modifying the grating surface is presented. The target is a reduction in diffraction and electrical losses in the device. Should these two drawbacks be removed or else mitigated, the ZBD technology will find new use in single polariser devices. This work represents the first step, and indicates a preferred direction for the work going forward.

1.3   Structure of the thesis

The thesis as a whole comprises four parts.

The first is the introduction; following this chapter, the first part commences with three chapters: the background physics of the work, followed by a review of the surrounding literature to provide further context going forward, and finally

an overview of the experimental methods that underpin the bulk of the work.

The second part is ZBD characterisation, exploring both experiment and modelling to further define the physics of the existing zenithal bistable device. It consists of two chapters, the first focusing on the characterisation of bistability through grating alignment, and the second on the defect dynamics during latching between the bistable states.

The third part comprises the methods used to improve the device, and examines their results. Once again, there are two chapters: in the first, the role of the LC material is explored; in the second, the scale of the grating is manipulated to target new device configurations.

Finally, the fourth part concludes the thesis and discusses further work which could build upon that presented here.

Chapter 2

Background and physics

This chapter will focus on the founding physical principles upon which the current zenithal bistable display operates, and upon which we may build improvements to the device. Initially, liquid crystal physics will be introduced. Following that, a general discussion of bistability and of the operation of ZBD will be included. Further details on its operation will be included in later chapters.

2.1 Liquid crystals

2.1.1 Phase and order

Liquid crystals are phases of matter which exhibit some of the order of crystalline solids but flow as liquids. This broad description encompasses a diverse subsection of matter providing a rich field of study. Most typically, LC materials adopt their phases either under changing solvent concentration (lyotropic) or temperature (thermotropic). The phases exist, caught between isotropic liquids and crystalline solids, due to a material's anisotropy. In thermotropic LCs, this is a shape anisotropy. Molecules which are rod-shaped (calamitic) or disc-shaped (discotic) may exhibit an intermediate LC phase on heating (Fig 2.1). These phases are further sub-categorised by their symmetry properties and their degree of crystalline order, the most simple being the nematic phase. In the nematic phase, molecules have no positional ordering but their long-axes on average lie

Figure 2.1: Two-dimensional illustration of the packing symmetries of liquid crystal mesogens in the isotropic liquid phase, the nematic phase, and the crystalline phase.

along the nematic "director" $\boldsymbol{n}$ with some degree of orientational order, S (2.1).

$$S = \left\langle \frac{3\cos^2\theta - 1}{2} \right\rangle \tag{2.1}$$

Here, θ is the angle deviation of the long axis from the director $\boldsymbol{n}$ [2]. The triangular brackets denote both spatial and temporal averaging over the ensemble. Typical values for S in the nematic phase across the temperature range are $0.4 - 0.8$. When heating through the nematic to the isotropic transition (T_{NI}), the order drops discontinuously to 0. A perfectly ordered crystalline solid has $S = 1$.

Order may also be represented by the tensor order parameter Q. This is a traceless, symmetric rank two tensor that describes both the average molecular alignment $\boldsymbol{n}$ and the order parameter S. For uniaxial systems it can be written as:

$$Q = S\left(\boldsymbol{n} \times \boldsymbol{n} - \frac{1}{3}\mathbb{1}\right), \tag{2.2}$$

where $\mathbb{1}$ is the 3×3 identity matrix.

Calamitic LCs may also exhibit smectic phases, which have layer ordering in addition to orientational order. Beyond nematic phases, these are commonly

studied phases in liquid crystals. However, they are unsuitable for use in ZBD and will not be discussed further. For the sake of simplicity, mention of liquid crystals in this thesis going forward will assume nematic phase calamitic liquid crystals unless otherwise specified.

2.1.1.1 Defects

In certain cases, such as in constrained geometries or unaligned cells, the nematic phase can include defects. These are points in an otherwise ordered nematic phase where the nematic order parameter S drops to zero. This prevents discontinuous elastic distortion in the phase and maintains topological continuity: defects reconcile regional director field changes with minimal elastic perturbation. When considered, defects are characterised by their strength and sign. The former indicates, when considering an imaginary orbit around the defect, how many times the director undertakes a full 2π rotation; the latter indicates whether this rotation was in the same sense (clockwise or anticlockwise) as the orbit [3].
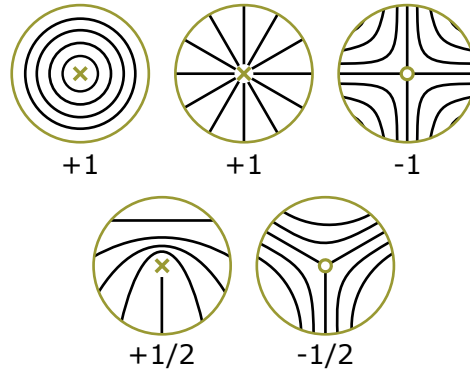
Figure 2.2: Diagram of the director distribution around ± 1 and $\pm\frac{1}{2}$ defects. The cores of the defects are indicated at the centre of the diagrams; lines correspond to average director orientation around the defects.

This thesis will be primarily concerned with the $\pm\frac{1}{2}$ defects, as shown in Figure 2.2 alongside ± 1 defects. When considering the half-power defects in two dimensions as shown, they are as point defects, whereas in three-dimensional reality they exist as line disclinations, with the line in question normal to the plane
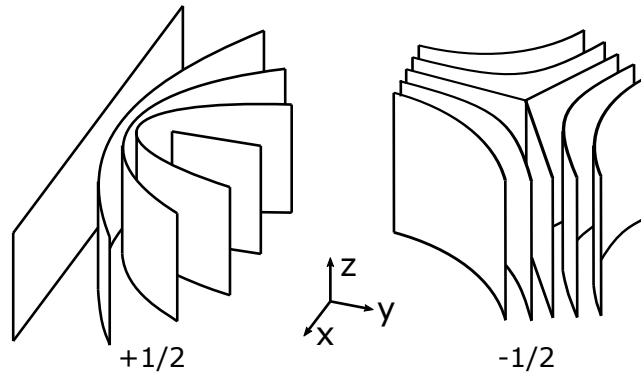
Figure 2.3: Sketch of the three-dimensional form of half-power defects, positive and negative. The defect core extends in the $\pm z$ direction, forming a disclination line. The director field is represented as sheets folded around the defect, confined on average to the xy plane.

of the page. An example of such a 3D case is presented in Figure 2.3.
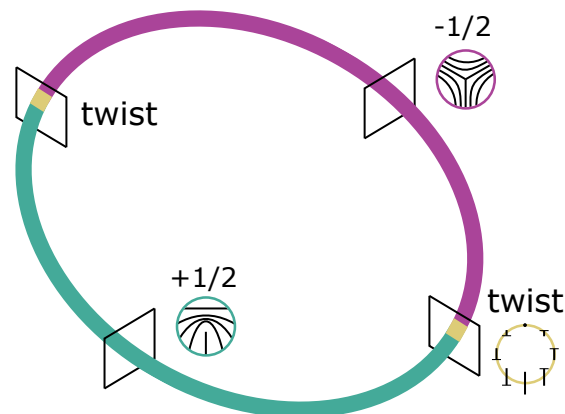
Figure 2.4: A disclination loop with two twisted transition regions (yellow) which transfer between $-\frac{1}{2}$ (purple) and $+\frac{1}{2}$ (teal).

Defects, as might be surmised by their positive or negative "charge," exist in most systems as pairs whose strengths sum to 0. If thermal or other energies are high enough in the system, pairs of defects will often come together and 'annihilate' - their individual director rotations cancel each other out. In 3D, defect

lines may also be connected as loops. A disclination loop of joined $\pm\frac{1}{2}$ defects is supported by two twists in the loop, transferring between the two strengths of defect and back again (Figure 2.4) [4].

2.1.2 Physical properties
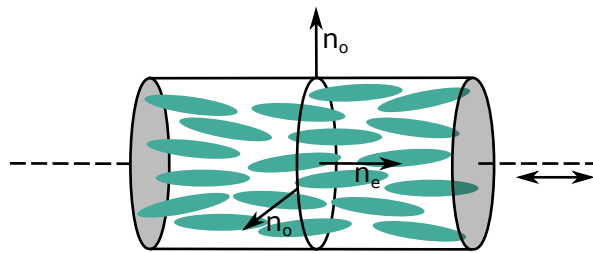
Figure 2.5: A schematic of the refractive indices in a nematic liquid crystal. The LC is uniaxial and so the optic axis coincides with the director

Key physical properties of liquid crystals, such as their optical, dielectric, and elastic behaviour, exhibit anisotropy determined by their molecular shape anisotropy.

A uniaxial liquid crystal has a single optic axis and two refractive indices, corresponding to the refractive indices experienced by light polarised perpendicular and parallel to the optic axis - the ordinary refractive index n_o and the extraordinary n_e respectively (Fig 2.5) [5]. The optical anisotropy $\Delta n = n_e - n_o$ is one of the major physical properties which lend LCs so nicely to the displays industry. A well-ordered nematic phase will have distinct optical character under different angles of incident polarised light. Manipulation of the optical behaviour of LCs is the key to their use in display devices.

Uniaxial LCs also have two differing electric permittivities due to the presence of a molecular dipole. When applied along the director, an electric field experiences the dielectric constant $\epsilon_{\parallel}$; perpendicular to the director it experiences $\epsilon_{\perp}$ [6]. Dielectric anisotropy $\Delta\epsilon = \epsilon_{\parallel} - \epsilon_{\perp}$ may be positive or negative and dictates

the liquid crystal's response to an applied electric field. An analogous magnetic anisotropy also exists. Reorientation of the LC director under an electric field is the primary mechanism of switching between different optical states in liquid crystal displays. In this thesis only materials of $\Delta\epsilon > 0$ are considered going forward.
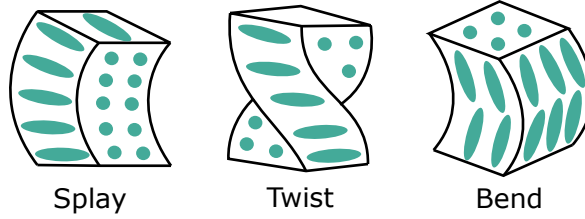
Splay   Twist   Bend

Figure 2.6: A diagram of three director distortions, splay, twist, and bend, whose energies are described by the elastic constants K_{11}, K_{22}, and K_{33} respectively.

Elasticity of liquid crystals relates to changes in director orientation. This differs from elasticity in crystalline solids, which relates to the displacement of molecules within the crystal lattice, and from elasticity in isotropic liquids, where it relates to density gradients. Three primary elastic constants describe this property in LCs: the splay elastic constant K_{11}, the twist elastic constant K_{22}, and the bend elastic constant K_{33} (Figure 2.6). The twist elastic constant is typically the smallest of the three. They are all on the order of pN. The elastic theory of liquid crystals was described by Oseen [7] and later developed by Frank [3].

Due to anisotropy, viscosity in liquid crystals is complex. In most cases, however, flow is ignored, partly due to complexity and partly due to the confined systems such as LCDs exhibiting minimal flow. There are still time dependencies associated with changes to director orientation, and so the primary measure of viscosity used is the rotational viscosity γ_1. This is found most readily when considering a liquid crystal acted on by an electric (or magnetic) field which causes director rotation when considering the response times of the system. There are two separate equations describing this behaviour, one for switching a pixel 'ON'

(response time) and another for 'OFF' (relaxation time). These will be presented in Section 2.1.5.

2.1.3   Mixtures

Different LC compounds may have wildly different properties. 5CB (4'-pentyl-4-cyanobiphenyl) was the first stable room-temperature nematic liquid crystal designed, and has a T_{NI} (nematic clearing point) of 35 °C. The analogous 7CB has $T_{NI} = 42$ °C. "Good" LC properties, as might be referenced in this thesis, are as optimised for display applications. In a nematic device, a broad nematic phase temperature range is essential. Preferable range may differ, but typically -20 °C-80 °C is a good baseline [8]. The material should be colourless, fast-switching, and have a high $\Delta\epsilon$. Unfortunately, a single LC compound cannot achieve each of these properties at once.

Liquid crystal mixtures are developed in such a way to optimise the ideal properties needed. Even a two-component mixture can give vast improvement to the operating temperatures of a single compound. For instance, many LC mixtures will comprise a eutectic system, meaning their melting temperature as a mixture is lower than that of either constituent part. This in turn extends the nematic temperature range. One common LC mixture is that of E7, which while 5CB is its main component, the addition of 7CB, 8OCB ($T_{NI} = 80$ °C), and 5TB ($T_{NI} = 239$ °C) gives the overall mixture a T_{NI} of 61 °C. 5CB may be isotropic in a warm room; E7 will remain nematic at ambient temperatures.

This thesis makes use primarily of the Merck liquid crystal mixture MLC6204-000, a display-quality liquid crystal mixture formulated for high $\Delta\varepsilon$- approximately 35 at 20 °C compared to 11 for 5CB [9]. Due to its commercial nature, the exact components are unknown, but the clearing point is 64 °C. It is designed to remain nematic down to -20 °C, with storage in a device to below -40 °C.

2.1.4   Alignment

By manipulating surface interaction at liquid crystal boundaries, such as at glass and plastic substrates in displays, it is possible to align the nematic director at the surface of a confined area. Clean glass will typically give homeotropic alignment; a polymer or other material deposited onto the substrates can give a controllable alignment, which may be planar (parallel to the surface) or homeotropic (perpendicular). Homeotropic anchoring in particular is usually given by a surfactant, with molecular tails pointed orthogonal to the cell surface plane. Any alignment has an associated anchoring strength, given in J/m or equivalently N/m^2. Distortions away from the given alignment direction will experience a restoring torque proportional to this value; to significantly reorient the director at a surface, this anchoring strength must overcome.
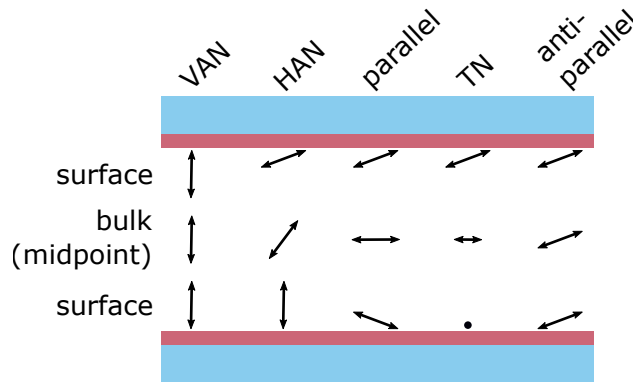
Figure 2.7: Schematic of different nematic director alignments in LC devices. Substrates are presented in blue, and alignment layers in pink. The planar alignments presented are all pretilted.

In the case of planar alignments, the polymer is typically rubbed with felt in order to choose the direction of alignment along the surface. This rubbing results in a pretilt of the director away from the surface in the direction of rubbing. Alignment of the director in the bulk will follow the surface alignment of both surfaces together, adopting an equilibrium alignment of minimum elastic

	Bright	Dark
HAN	45 °	0 °
VAN	n/a	all angles
parallel	45 °	0 °
TN	all angles	n/a
anti-parallel	45 °	0 °

Table 2.1: Table of bright and dark states for nematic director alignments through crossed linear polarisers. Angles are defined with respect to one polariser.

distortion across the cell. Configurations involving a homeotropic surface are vertically aligned nematic (VAN), consisting of two homeotropic substrates and hybrid aligned nematic (HAN), consisting of a homeotropic surface opposing a planar aligned surface. Two opposing planar substrates may be combined in three distinct configurations: parallel, orthogonal, or antiparallel to one another. These result in planar parallel, twisted nematic (TN), and planar antiparallel, respectively. A schematic of these is presented in Figure 2.7. With the addition of crossed polarisers to the device, these alignments may appear dark or bright (see Table 2.1).

Optimising the bright states for display performance requires targeted cell gaps. HAN, planar parallel, and planar anti-parallel devices require Δnd corresponding to the half waveplate condition $\Gamma = \pi$ where retardation Γ is given by

$$\Gamma = \frac{2\pi\Delta nd}{\lambda}. \tag{2.3}$$

Δn must be adjusted, in planar antiparallel to account for the pretilt, and in HAN to account for hybrid alignment (using $\Delta n/2$). In TN, Δnd targets the Gooch-Tarry maximum (this will be discussed in further detail in Chapter 5). Both the half waveplate condition and the Gooch-Tarry maximum depend on wavelength λ; for visible light calculations using 550 nm give a good bright state.
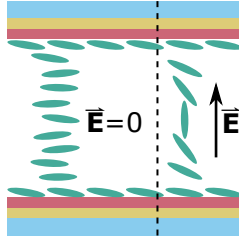
Figure 2.8: A schematic of director realignment on application of an electric field. The field is applied orthogonal to the plane of the cell substrates and so reorientates the director in a planar antiparallel cell to homeotropic in the bulk for positive $\Delta\epsilon$ materials.

Much of the work in this thesis is done using the contrast between the VAN and the HAN state when aligned 45 ° to the polarisers, as this is the simplest device form for ZBD testing. With reference to Table 2.1, the VAN state is dark and the HAN bright in this configuration, and so the switch between them can be identified.

2.1.5 Electrical reorientation

Due to the dielectric anisotropy of liquid crystals, the director field within the bulk of the cell may be reoriented by applying an electric field across the cell (Figure 2.8). The director of an LC with a positive dielectric anisotropy has lower free energy when aligned parallel to an applied electric field. If the field is of sufficient magnitude and applied counter to the static alignment of the LC within the cell, the director will begin to rotate to follow the field.

The LC viscoelasticity resists this rotation. For realignment to occur, the field must surpass a threshold related to the elastic constant K by

$$V_{th} = \pi\sqrt{\frac{K}{\epsilon_o\Delta\epsilon}},\qquad(2.4)$$

where ϵ_o is the permittivity of free space, V_{th} is the threshold voltage in volts, and $\Delta\epsilon$ is the dielectric anisotropy. The specific elastic constant depends on the ge-

ometry used and the sign of the dielectric anisotropy. For a homogeneous planar aligned positive $\Delta\varepsilon$, the splay elastic constant K_{11} is used. The onset of rotation of the director in the bulk above this threshold is known as the Fréedericksz transition [10, 11, 12].

Due to viscosity, this dielectric switching has an associated time-scale. The application of an electric field across the cell has response times related to these properties [8].

$$t_{on} = \frac{\gamma_1 d^2}{\epsilon_o \Delta\epsilon (V^2 - V_{th}^2)} \tag{2.5}$$

$$t_{off} = \frac{\gamma_1 d^2}{K \pi^2} \tag{2.6}$$

Equation 2.5 describes the response time t_{on} of the liquid crystal to an applied electric field V/d without flow. It relates to the dielectric anisotropy, the threshold voltage, the electrode spacing in the cell d, and the rotational viscosity γ_1. Equation 2.6 gives a restoration time t_{off} after which the director field has reoriented to its original undisturbed state. This is inversely proportional to the elastic constant K, and is not a function of the applied voltage. The K considered for this thesis is the bend elastic constant K_{33}; for high $\Delta\varepsilon$ materials in a planar cell relaxing from high fields this approximations holds. It remains satisfactory for materials with $0.5 < K_{11}/K_{33} < 1.5$. In many cases, this relaxation time is the limiting factor in device performance, as it cannot be controlled by simply using a higher voltage. This highlights the necessity for carefully formulating liquid crystal mixtures with the correct properties in the desired temperature range.

At the Fréedericksz transition, it is only the director in the centre of the cell that begins to rotate. As the applied field increases, the rotation angle of the bulk will increase with the field, resisted by the elasticity of the LC. At the cell boundaries, surface anchoring energies counteract the rotation. Unless the applied field is sufficiently high to break the surface anchoring (typically above the dielectric breakdown voltage), the director will remain aligned at the surface up to a coherence length.

2.1.6 Free energy

Considerations, and especially minimisations, of the liquid crystal free energy lend insights into the behaviour and stability of liquid crystal devices. Each aspect of the system contributes a term to the free energy, such as the elastic, electric, and surface terms. For a given volume ν and surface σ, the free energy can be written in the form:

$$F_{tot} = \int_{\nu} (F_{th} + F_{elastic} + F_{electric})\, d\nu + \int_{\sigma} F_{surf}\, d\sigma. \qquad (2.7)$$

The first three terms here comprise the bulk free energy, and the latter the surface energy. F_{th} is the Landau-de Gennes thermotropic free energy which can be expanded as:

$$F_{th} = \frac{1}{2}a(T)\operatorname{Tr}(Q^2) + \frac{1}{3}b(T)\operatorname{Tr}(Q^3) + \frac{1}{4}c(T)\operatorname{Tr}(Q^2)^2, \qquad (2.8)$$

where Q is the tensorial order parameter (Equation 2.2), and a, b, and c are the thermotropic coefficients. This expansion discounts terms $O(Q^5)$ and lower. $F_{elastic}$ is expanded in terms of the director:

$$F_{elastic} = \frac{1}{2}K_{11}(\boldsymbol{\nabla} \cdot \boldsymbol{n})^2 + \frac{1}{3}K_{22}(\boldsymbol{n} \cdot \boldsymbol{\nabla} \times \boldsymbol{n})^2 + \frac{1}{2}K_{33}(\boldsymbol{n} \times \boldsymbol{\nabla} \times \boldsymbol{n})^2 \qquad (2.9)$$

using the elastic constants as previously defined. The final bulk term is for external fields such as electric fields. When E is constant, we can write this case as:

$$F_{electric} = -\frac{\epsilon_o \Delta\epsilon}{2}(\boldsymbol{E} \cdot \boldsymbol{n})^2, \qquad (2.10)$$

where ϵ_o is the permittivity of free space and $\Delta\epsilon$ is the dielectric anisotropy as before. The final term represents surface interactions between the liquid crystal and the alignment layers. This is primarily governed by the anchoring at the surface, which is typically given in the Rapini-Papoular form:

$$F_{surf} = -\frac{1}{2}W(\boldsymbol{n} \cdot \boldsymbol{n}_o)^2. \qquad (2.11)$$

Here, W is the anchoring strength and $\boldsymbol{n}_o$ is the preferred direction at the alignment layer. Other free energy terms may be included, such as for flexoelectric

polarisation, depending on the system [13].

Minimisation of the free energy of a liquid crystal cell may give solutions for the static state director configurations and is key to properly modelling devices.

2.2 Displays and bistability

Liquid crystal displays utilise the differing optical characteristics of optic axis orientations to switch between dark and bright states on a pixel-by-pixel basis, thereby displaying an image. An example setup employs a TN geometry for the bright state, and switches towards the homeotropic in the bulk under electric field for the dark state.

Displays as they have been described thus far are monostable, meaning in the absence of an applied field the director field relaxes back to its original state. To maintain the second state requires a constant applied field, i.e. this state is not stable in the absence of an electric field. For certain applications, such as e-readers, billboard advertisements, or digital shelf-edge labels where a static image is displayed for some time, this represents a significant power consumption which might be otherwise avoided. Use of a bistable display, having two stable states which may be selected by electrical input, would alleviate this power drain. Multiple display technologies have been created to fill this niche, including e-ink, BiNem®, and the zenithal bistable device [14, 15, 16]. This thesis focuses on the latter, and development of bistable liquid crystal technology will be discussed in Chapter 3.

Bistability in ZBD is achieved through the use of a micron-scale grating replacing the alignment material on one substrate of the device. The grating is given a homeotropic surface treatment such that the LC director tends to align perpendicular to the grating surface. However, depending on the director distortion adopted around the grating, the director may give either a high ($\tilde{9}0$ °) or low tilt (0-55 °) above the grating referenced from the surface parallel (Figure 2.9)

17
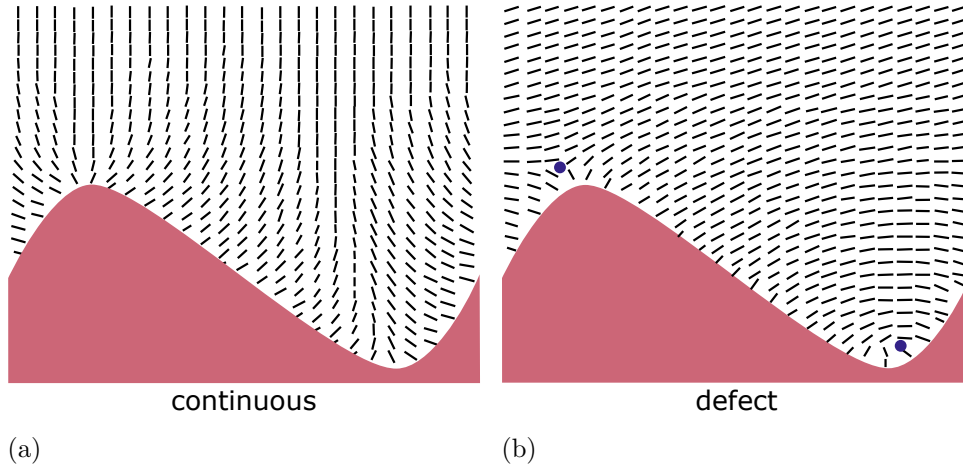
Figure 2.9: Two dimensional example of director distortion around a blazed sinusoidal grating. (a) is the continuous (C) state, and (b) is the defect (D) state. The location of the two defects is indicated by small circles in the D state diagram; the $-\frac{1}{2}$ defect at the top of the groove and the $+\frac{1}{2}$ at the bottom. Lines indicate the average director orientation.

[17], and each are of a similar energy. In the case of high tilt, this is given by continuous distortion of the director around the grating. For low tilt, director distortion includes defect pairs (Figure 2.2). These are a $+\frac{1}{2}$ defect situated at the bottom and a $-\frac{1}{2}$ defect at the top of the grating grooves. In three dimensions these defects are connected as a loop. The two states are abbreviated as the C and D state, respectively. The defects of the D state lower the overall distortion energy around the grating and are stabilised by the curvature of the grating. An energy barrier, which may be overcome by a suitable electrical impulse, separates the two states.

In order to stabilise the defect loops on the grating surface, slips were introduced [18]. The grating grooves extend only as far as around 5 µm at a time, at which point the grating is shifted by half a pitch. Two views which indicate the slips in the grating are given in Figure 2.10. When the grating 'slip' is referenced, it is to indicate the seam between two adjacent, pitch-shifted gratings.
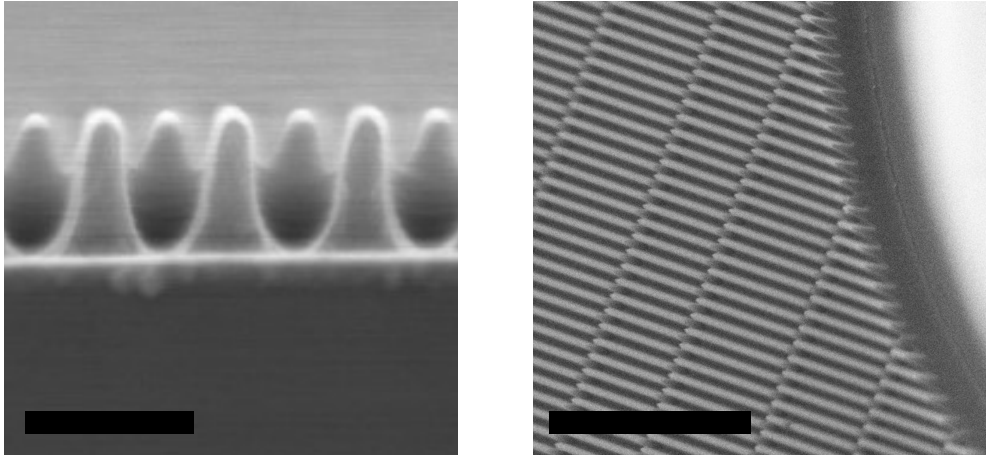
Figure 2.10: SEM images included to highlight grating slips in ZBD. In the first image, scale bar 1 µm, shifted grating peaks can be seen behind the focal grating in front. In the second, scale bar 10 µm, an angled top-down view is shown, highlighting the distances between slips.

(a)

(b)
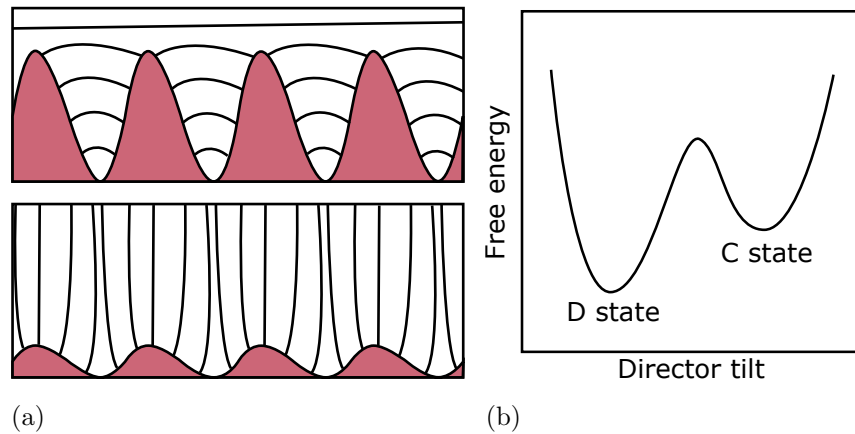
Figure 2.11: (a) Examples of alignment at a homeotropic grating in the case of D state monostability (top) and C state monostability (bottom). (b) An example of a free energy diagram which indicates a favourable D state and a reasonable energy barrier to achieve C state.

In order for the system to be bistable, the grating shape, liquid crystal properties, and the anchoring strength (surface interaction) must be carefully balanced.

19

With respect to the grating, too-shallow a grating will favour the C state, and too-deep a grating will favour the D state (Figure 2.11(a)). If the homeotropic anchoring strength is sufficiently weak, neither state will be supported, as degenerate homeotropic anchoring will lead instead to conically degenerate and eventually a planar (P) state oriented along the grating grooves. The highest anchoring strengths favour the C state, and lower favour the D state. In the commercial device, properties are controlled such that the D state is slightly, but consistently, of lower energy. In this way, a display will always adopt the D state without other input so that areas without or between electrodes are uniform. An example energy diagram of this setup is seen in Figure 2.11(b).

In monostable LCDs, a constant field is required to maintain the 'ON' state. Without a field, the display is in the 'OFF' state. In bistable displays, a mechanism switches between two 'latched' states which are mutually stable, meaning that on removal of the field the display remains in the selected state indefinitely. The switch needs to be performed in both directions, and so the standard dielectric response is not viable. Liquid crystal electrical response goes with E^2 (Equation 2.10) and so a 'reverse' effect based on polarity does not exist. Instead, the ZBD latches using a property of liquid crystals known as flexoelectricity.
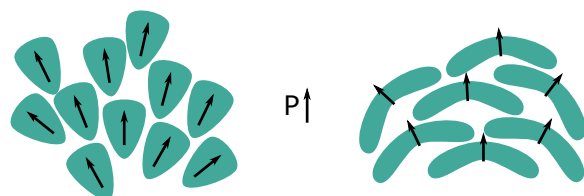
Figure 2.12: A schematic of how nematic packing of pear- and banana-shaped molecules can lead to a flexoelectric polarisation.

Flexoelectricity results from the coupling of a molecule's electric dipole and molecular asymmetry. More typically, perhaps, this is a property of molecular shapes such as 'banana' or 'pear,' where molecular packing results in an overall polarisation (Figure 2.12). No LC molecule is perfectly cylindrical, and so each material will exhibit at least small flexoelectricity. ZBD operates even with such
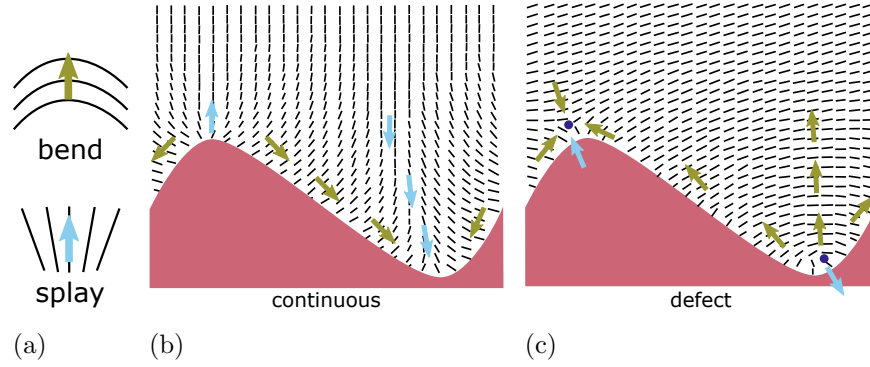
Figure 2.13: Diagram of local flexoelectric polarisation introduced by a distorting grating. (a) gives the directions of flexoelectric polarisation for $e_{11} > 0$ and $e_{33} < 0$ in regions of pure splay and bend. (b) indicates local flexoelectric polarisations in the C state, and (c) in the D state.

molecules - additional flexoelectric polarisation results from the molecular distortion around the grating (Figure 2.13). Flexoelectric response is polar, and hence is able to switch in both directions. The polarisations for each bistable state are in opposing directions, allowing the flexoelectric coupling to switch between them.

When considering free energy in a ZBD cell, an additional term must be added to the bulk terms in Equation 2.7 to account for the flexoelectric polarisation. This term is:

$$F_{flexo} = \boldsymbol{P} \cdot \boldsymbol{E}, \tag{2.12}$$

where the polarisation vector $\boldsymbol{P}$ is

$$\boldsymbol{P} = e_{11}(\boldsymbol{\nabla} \cdot \boldsymbol{n})\boldsymbol{n} + e_{33}(\nabla \times \boldsymbol{n}) \times \boldsymbol{n}. \tag{2.13}$$

More detailed consideration for the free energy in the ZBD device will be discussed in the next chapter.

2.3   Conclusion

Liquid crystal properties as they pertain to this thesis and the basis of bistability in ZBD were the main focus of this chapter. The principles of liquid crystal physics lead to the operation of liquid crystal displays. The basic principles of bistability in ZBD were introduced; these will be expanded on in the remaining introductory chapters to present understanding, and developed further in Part Two: Characterising ZBD. The following chapters will build upon the foundational physics established here.

Each results chapter following may present its own further physical and theoretical principles; the aim of this chapter was to establish the items which underpin the thesis as a whole. A review of the literature follows.

Chapter 3

Literature review

The following review of the literature surrounding the work of this thesis comprises an introduction to existing bistable nematic devices in turn, highlighting a few and introducing their fallbacks, and a historical literature review of the zenithal bistable display to date. Due to the nature of the individual research points of this thesis, their chapters will each include their own brief reviews when required.

3.1   Nematic bistability

Soon after the invention of liquid crystal displays, it was realised that the switching characteristics were too linear to electrically address all but the simplest images. For a pixel matrix of N rows and M columns, as N increases, the ratio of the RMS 'ON' voltage to the 'OFF' voltage must approach unity - this is known as the Alt-Pleshko limit [19]. This ratio is related to the steepness of the transmission-voltage curve for the device in passive matrix addressing. A sketched example curve is included in Figure 3.1. The steeper the curve, the more lines can be addressed, and the larger and more complex the image [8].

Running up against this limitation, three solutions were explored to bring LCDs to the prominence they have today. In the first, use of targeted materials (using optimised elastic constants) or of the display mode super-twisted nematic (STN) gave the required steep transmission-voltage curve for multiplexing in passive-matrix addressing [20, 21].
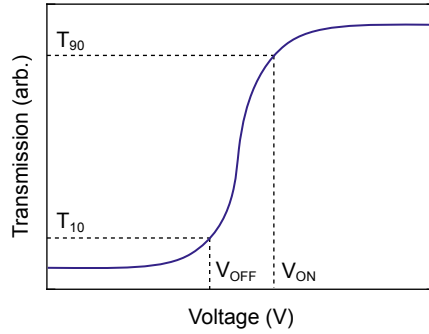
Figure 3.1: An example plot indicating the typical form of data of transmission versus voltage for a nematic pixel between crossed polarisers. The 'ON' and 'OFF' voltages are indicated, corresponding to 90 and 10 % transmission. Steeper curves result in closer thresholds V_{ON} and V_{OFF}.

As a second solution, active matrix addressing was developed. A thin film transistor (TFT) behind each pixel was utilised to individually switch the pixels to the correct state. This is the method used in phones, laptops, and TVs today. The third solution was to continue with passive matrix addressing but utilise bistable display configurations. Since This mode is less suited to larger displays and video speeds, and best suited to applications where image refresh is rare or power consumption is a limiting factor. Bistable displays are also more readily able to make use of lightweight plastic substrates; manufacture of TFTs on plastic substrates is limited by the necessity of high temperatures. Use of smectic and ferroelectric liquid crystals began the bistable LCDs field; however, nematic bistability is generally more attractive, due to the availability of display-quality mixtures for temperature range and other desirable properties and their increased stability under mechanical shock. Bistable nematic devices can also benefit from existing nematic research and manufacture infrastructure.

One of the first bistable nematic displays utilises anchoring breaking - the flexoelectrically controlled surface bistable device invented by Barberi, Giocondo, Martino-Lagarde and Durand in 1990 [22]. The planar (P) and oblique (O) states are supported by an evaporated SiO alignment layer. Switching between these

24

Bigrating

(a)

Strongly anchored

Weakly anchored

π-twist   0-twist

(b)

Planar (P)   Tilted (T)

(c)
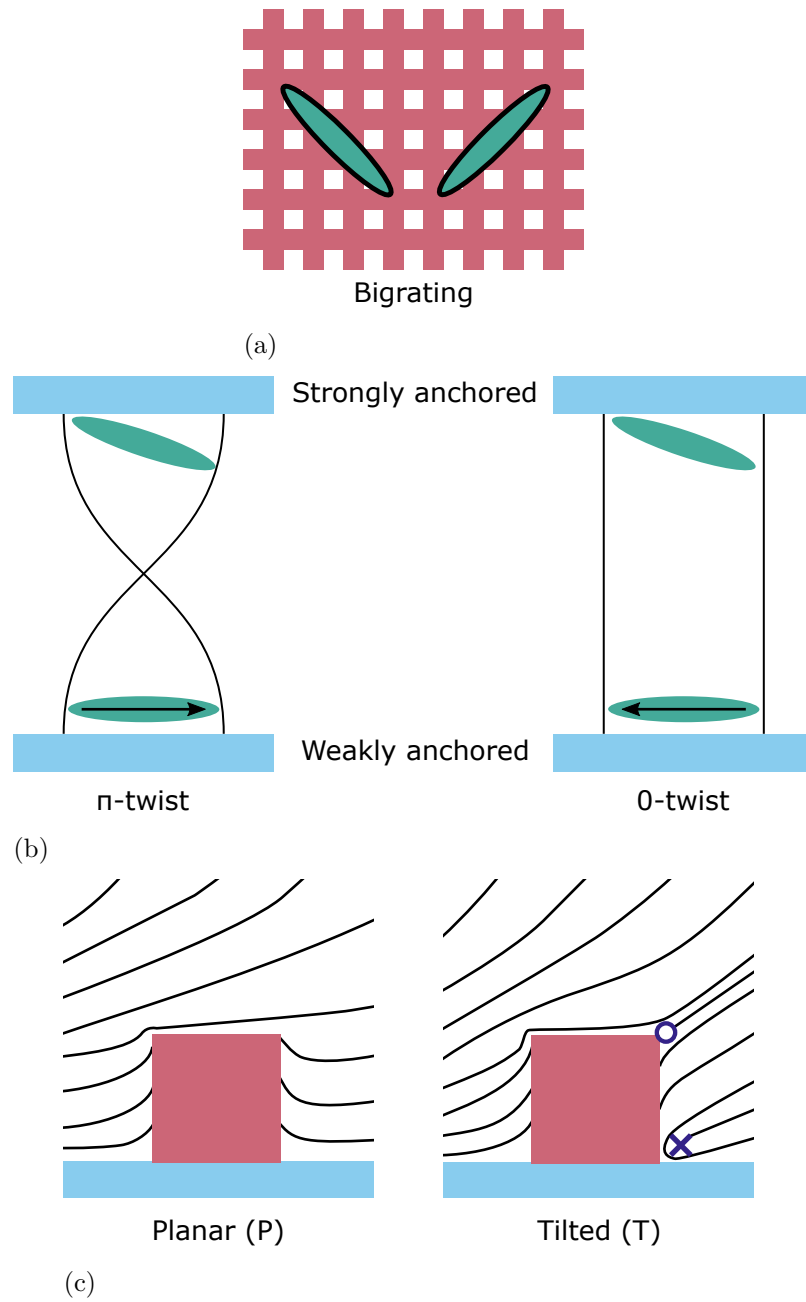
Figure 3.2: Bistable alignments for different nematic bistable devices. (a) ABD's two mutually stable alignments at ± 45 ° on a bigrating. (b) The π- and 0-twist states for BiNem®. (c) The tilted and planar states of PABN. The X represents a $+\frac{1}{2}$ defect, the circle a $-\frac{1}{2}$ defect.

states involves first breaking the anchoring, and then selecting the final state with dielectric and flexoelectric coupling using a negative $\Delta\varepsilon$ LC [23]. The P and O states have a constant azimuthal angle but opposite splay. The device offers all the benefits of bistability, but the surface treatment tolerances proved too tight for commercial manufacture. Use of negative $\Delta\varepsilon$ materials is common in these devices, which itself presents an issue; there is a lack of negative $\Delta\varepsilon$ with high dielectric anisotropy, limiting the devices' performance further. As an example, a high dielectric anisotropy can be considered $|\Delta\epsilon| \geq 10$ while recent research has produced negative materials with $|\Delta\epsilon| \sim 4$ [24, 25].

This device inspired the use of surface gratings to stabilise multiple nematic alignment states. The azimuthal bistable device (ABD) [26] uses a symmetric bigrating on one cell surface. By properly selecting the amplitude and pitch of the two aspects of the bigrating together, a bistable configuration can be achieved where ± 45 ° alignments at the surface are equal energetically (Figure 3.2(a)) [27, 20]. Azimuthal switching, as it happens in the plane parallel to the surfaces and hence perpendicular to the applied field, involves high electrical thresholds in excess of ± 19 V [20]. There's also the possibility of surface memory leading to image sticking. State selection proved to be unreliable due to the low pretilt, and ultimately this was not a commercially successful technology [21].

Following this device, the zenithal bistable device was first developed [16]. A single grating, rather than a bigrating, gives two stable states switchable through flexoelectric coupling. It is a commercially successful technology, with over 30 million units sold by DisplayData. Its development to date will be presented in detail in the following section.

The π-twisted bistable nematic device, known commercially as BiNem®, was developed at a similar time as ZBD. It uses surface anchoring breaking to give two stable states, similar to the Durand device. These are the uniform (U) and twisted (T) states, displaying a uniform planar director field and a 180 ° twisted director field respectively (Figure 3.2(b)). By applying an electric field, one of the surface anchorings is broken, and the final state selected via either elastic or

hydrodynamic coupling of the director field [15]. The hydrodynamic selection of the π-twisted state requires very thin cell gaps for efficiency, no more than 1 - 2 µm [28]. The devices had high optical contrast but ultimately were not commercially successful, due to the difficulties with the surface anchoring and the low cell gap tolerances [28, 29].

Following on from the success of the grating devices, Kitson and Geisow developed a bistable nematic device based on alignment around a periodic array of microstructure posts: the post-aligned bistable nematic (PABN) [30]. The posts are each 1 µm high at 1.4 µm pitch with planar degenrate anchoring [31]. The array can physically support eight individual alignment states, but many of these are not optically distinct - the two bistable states chosen for operation are the planar (P) state and the tilted (T) state (Figure 3.2(c)) [32]. The former is a continuous director distortion over the posts whereas the latter includes defect pairs at the top and bottom corners of one post edge. The tilted state is selected on cooling, and has the lower of the two states' birefringence. Selection between the states is performed using monopolar square pulses coupling to the negative $\Delta\varepsilon$ material. Unfortunately, the two states, while optically distinct, have low contrast between them, reducing the feasibility of the display device.

3.2   Zenithal bistable display

In the first paper published concerning ZBD, it was presented as a bistable display using a single-substrate surface relief grating with bistability between VAN and HAN states [33]. The grating was formed in photoresist using off-axis exposure in hard contact photolithography. This exposure angle, when varied, gave different pretilts to the resulting bulk alignment of the grating - pretilts of 0-55 ° have been demonstrated [17]. The device was shown to latch with pulse polarity by coupling to the flexoelectric polarisation induced by the grating [33]. Further down the line, TN/HAN operation was demonstrated [34]. This configuration has far superior contrast to that of VAN/HAN - 130:1 in transmissive mode at normal incidence compared to 20:1. The viewing angle is particularly good in

reflection since the HAN state self compensates in that geometry. Excellent optical properties have been achieved even without compensators [35]. Here, the control of the pretilt was essential, as adopting a lower D-state pretilt gave access to excellent viewing angle at commercially available cell gaps, typically 5-7 µm.

Improvements were made to the latching protocol, moving from monopolar to bipolar pulses [1]. In both cases, the voltage applied must be above a threshold dependent on the pulse duration in order to latch to the desired state. For voltages significantly higher than the threshold, the device may experience a reverse latch out of the desired state, which restricts the latching window. Use of a bipolar pulse both lowers the threshold latching fields and improves the latching window by offsetting the reverse latch threshold. This reverse latching is attributed to ionic effects and is worsened at longer pulse lengths; bipolar pulses provide DC balancing reducing ionic segregation.

Simple, high throughput grating manufacture was later demonstrated using embossing [36, 37, 38]. The grating produced using photolithography is electroformed in nickel to give a master, from which the grating profile is transferred to resin-on-film. This film is used to emboss onto substrates over large areas. The two bistable states, C and D, were also further stabilised through the introduction of grating slips: 180 ° phase shifts of the grating at micron intervals (Figure 2.10) [18]. In this way, the defect loops of the D state are pinned at the slips, stabilising regions of D held next to C state, i.e. at pixel or greyscale boundaries.

Novel device geometries provide avenues for multistable ZBDs, such as the use of trapezoidal grating profile or two grating substrates (double ZBD) [17]. The trapezoidal grating has four defect pinning sites where sinusoidal has only two, leading to multistability. In the right configuration, two opposing gratings (double ZBD) can give rise to pi-cell like operation (targeting fast switching times), with four stable states and a fifth metastable state. These are the HAN1, HAN2, VAN, and Bend states, and the Splay state, respectively. Double ZBD also opens up bistable TN/VAN operation for ideal transmission and optical contrast [17].

Commercially, the ZBD has outlasted every other bistable nematic device. The technology has all of the standard benefits of nematic bistability: low power consumption, multiplexibility, mechanical and temporal stability [16, 33]. Multiple possible display configurations lend the device to transflective displays and single polariser reflective displays [39]. ZBD has been demonstrated to achieve latching at lower than 20 V faster than 80 µs and operate across a wide temperature range (-20 to 80 °C) [1]. This latching speed means a full e-book page could be written in as little as 10 ms. ZBD also boasts higher tolerances on cell gap than other displays, ±0.25 µm versus ±0.05 µm for STNs [17]. The eventual niche which ZBD fell into was that of shelf-edge retail signage, where bistability reduces operating power over standard LCD labels and is quickly cost effective over printed physical labels [17]. Using remote updating at radio frequency, the battery included in the device can last seven years [17, 18]. This communications protocol combined with the ease of manufacture were the deciding factors to the ZBD's success over other bistable technologies.
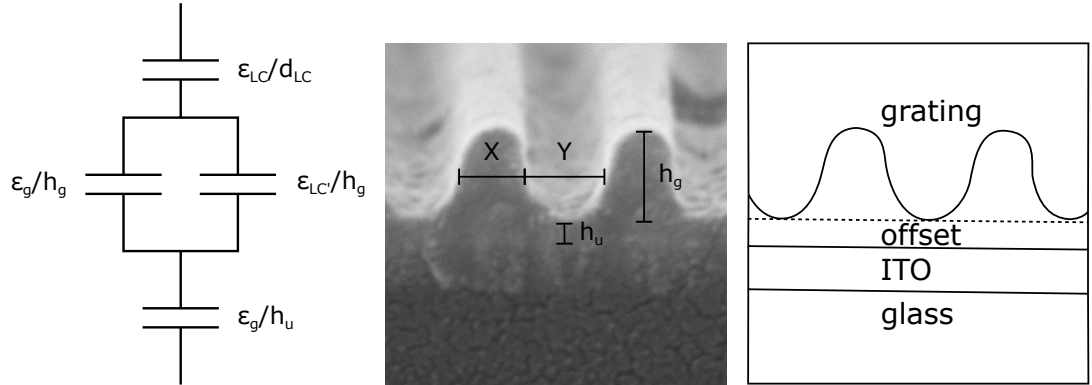
Figure 3.3: (a) An equivalent circuit based on the different dielectric layers present at the grating surface in a ZBD. (b) A labelled diagram of an example grating. (c) A labelled schematic of grating, offset, ITO, and glass. Within the diagrams, ϵ refers to dielectric perimittivity, d to cell gap, and h to structure height. The subscripts refer to: LC, the bulk liquid crystal, LC', the inter-grating liquid crystal, g the grating, and u the offset.

The physics of the device have been studied over the years, providing the basis

for the work in this thesis. A simple theoretical model of zenithal bistability not including the grating, but instead modelling a single bistable planar surface, was developed initially [13]. This treatment sees the flexoelectric effect acting, in essence, as an alteration to the surface free energy, stabilising and destabilising the two states based on the anchoring strength and applied electric field. In [1], the authors present a form for the field E_{LC} by considering the equivalent circuit for the device (Figure 3.3):

$$E_{LC} \approx \frac{V}{d_{LC} + \left(\frac{h_u}{\epsilon_g} + \frac{h_g}{\epsilon_g G + \epsilon_{LC}(1-G)} \right)}, \tag{3.1}$$

where $G = \frac{X}{X+Y}$ (unitless) and X and Y (m) are the FWHM of the peak and groove of the grating, respectively, as seen in Figure 3.3(b). Other parameters are as defined in the same figure. The same paper presents the first latching impulse equation:

$$\tau_{CD} \sim \frac{\gamma_1}{P_S E_{CD}}, \tag{3.2}$$

where P_S is the surface polarisation associated with the grating and E_{CD} is the threshold latching field. It was proposed at the time that the surface polarisation P_S could include contributions from multiple sources, such as flexo-, ordo-electric, dielectric, and ionic effects. γ_1 is the rotational viscosity, as discussed in Chapter 2. An expanded latch equation was found when comparing a more complex model to experimental results in [40].

$$\tau_i = \frac{\gamma_1 l_{s,i} d}{(e_{11} + e_{33})(V_i - V_{th,i})}, \quad i = CD, DC \tag{3.3}$$

New parameters have been introduced, including l_s the liquid slip in units of length, and the flexoelectric sum $(e_{11} + e_{33})$. This indicates that the surface polarisation from [1] is a result of the flexoelectric effect, and may be rewritten as $P_S = (e_{11} + e_{33})/l_s$. V_i (V) is the threshold latch voltage for the pulse duration τ_i (s) and $V_{th,i}$ (V) is a global threshold voltage below which no latch occurs for any τ. The final iteration of this form of the latching equation is presented in full
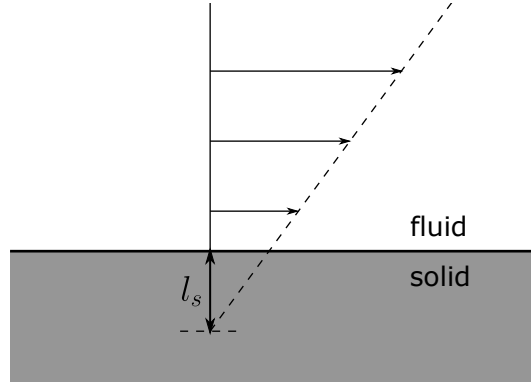
Figure 3.4: A diagram showing the extrapolation of flow to the liquid slip length.

in [18], where the form of the grating is also included:

$$
V_{CD} = \frac{\gamma_1 l_s d}{(e_{11} + e_{33})\tau}
$$
$$
+ \frac{2W_\theta}{(e_{11} + e_{33}) + \sqrt{\epsilon_o \Delta \epsilon K_{33}}} \left(d + h_u \left(\frac{\epsilon_\parallel}{\epsilon_g} - 1 \right) + h_g \left(\frac{(\epsilon_\parallel - \epsilon_g)X}{\epsilon_g X + \epsilon_\parallel Y} \right) \right).
$$
$$(3.4)$$

ϵ_o is the permittivity of free space. This is the first time we see a latching equation include the dependence on anchoring strength W_θ, despite it being demonstrated before [40]. Work in this thesis is carried out using the above equation simplified by two assumptions: first, that the grating offset is negligible $h_u \approx 0$, and second, that the grating height is significantly less than the cell gap $h_g << d$. This leads to the latching threshold equation seen in [41]:

$$
\tau = \frac{\gamma_1 l_s d}{(e_{11} + e_{33})(V_{CD} - V_{th})},
$$
$$
V_{th} = \frac{2W_\theta d}{(e_{11} + e_{33}) + \sqrt{\epsilon_o \Delta \epsilon K_{33}}}.
$$
$$(3.5)$$

The liquid slip l_s introduced in [13] is viscosity-related term which indicates the depth within a surface at which a no-slip boundary could be extrapolated when there exists slip at the surface 3.4. In the vast majority of cases, a no-slip boundary at the surface is assumed and the liquid slip is not considered. When

it is, it typically remains small, on the order of nm [42].

In recent years, a number of non-display optical devices making use of the ZBD technology have been proposed and theoretically examined. These include: beam splitter switches, made by setting out ZBD with a diffracting and non-diffracting mode by index matching the LC n_e to the grating polymer [43]; switchable beam steering using a similar approach but with a blazed triangular grating to maximise (minimise) the $m = 1$ ($m = -1$) mode [44]; a switchable circular polariser based on double ZBD [45]; and a switchable guided-mode resonant filter [46]. The proposed devices are an attractive goal for the ZBD technology. The first two listed are most feasible, as they only make use of a single grating. The latter two propose a configuration using double ZBD and dual-frequency LC materials. While double ZBD operation has been demonstrated [17], associated dielectric and optical losses with the extra grating and tricky switching mechanisms make commercial production mostly unviable with current technology. Dielectric losses are also an issue with the use of dual frequency LCs, as discussed in [33].
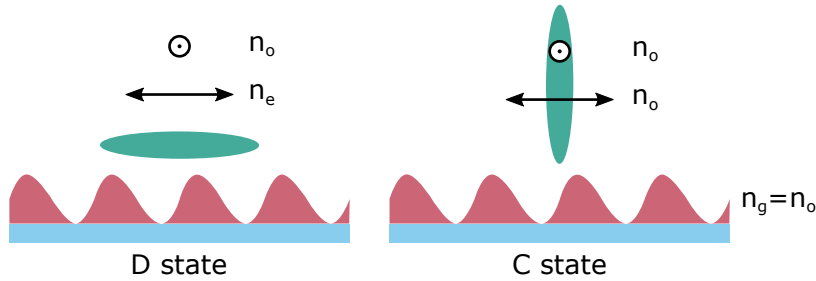
Figure 3.5: Schematic of how index matching can overcome the diffraction problem of ZBD. Indicated are the LC refractive indices seen by different polarisations of light.

These proposed optical applications for ZBD make note of a key issue in the technology: the diffractive properties native to the grating. Its pitch and amplitude mean it diffracts visible wavelengths. This is counteracted in commercial ZBD by index matching the LC to the grating photopolymer (Figure 3.5). That is, the liquid crystal used must have n_o matched to the refractive index of the

grating to ensure uniform reflectivity and colouration [37]. This must be true for both bistable states, or else one will be diffracting. The polariser at the grating surface is oriented to offset this effect also, but for single polariser mode this is no longer possible.

This thesis will build upon the work before it. Because of the commercial nature of the device, much of the physics has not been explored in detail. In the first of four results chapters, the latching thresholds will be looked at in detail, providing further experimental evidence for the relationship given in Equation 3.5 [18, 41]. A method of reliably giving homeotropic alignment to the grating polymer will be presented and characterised. The second results chapter, which explores defect dynamics using computational modelling, builds upon the previous theoretical and modelling works [13, 40, 47]. Quirks of the physical performance of the device, only obvious after detailed study, are explored and defined. Recent materials work in the liquid crystal community includes much in the way of bent materials, the twist-bend nematic phase, and the flexoelectric effect. Targetting strongly-flexoelectric materials in ZBD is a logical next step when considering the importance of material choice in the device [1, 40] and of the flexoelectric effect [13]. In the third results chapter, we explore the use of bent molecules in ZBD with the aim of improving the electrical performance of the device. Finally, new grating shapes are examined. By targetting low-pitch gratings, the aim is to offset optical and dielectric losses of the gratings, which not only will improve performance in the standard device through contrast and operating voltages, but will hopefully make feasible commercial double ZBD.

Chapter 4

Experimental methods

The goal of this chapter is to demonstrate experimental methods that underpin the four results chapters that follow on directly from this one. Each experiment is conducted within a LC cell, the fabrication of which is presented first. Next, polarising optical microscopy is introduced, as the experiments are primarily electro-optic. Application and evaluation of ZBD latch pulses is presented finally. One results chapter, Chapter 6, deals primarily in computational modelling. Methods for the modelling are presented therein, as they do not apply to the further chapters. Similarly, methods for the fabrication of new grating shapes are presented within the requisite chapter, Chapter 8.

4.1 Cell fabrication

Fabricating a liquid crystal cell provides a controlled experimental environment for much of the work in this thesis. Careful fabrication of the cell increases reproducibility and confidence in cell parameters, such as cell spacing d, alignment, and uniformity.

A liquid crystal cell at its base components consists of two planes of glass held at a known separation and filled with liquid crystal. Electrodes are also needed to apply electric fields to the LC and are used to conduct most of the experiments in this thesis. As such, the cells are constructed using glass coated with $O(100 \text{ nm})$

35

4. EXPERIMENTAL METHODS

indium tin oxide (ITO): a transparent electrode. In order to control the electrode area, the ITO is etched to experiment specifications. For our purposes, a spade-shaped electrode is used giving a 1 cm^2 total area (a diagram showing the etched electrode can be seen later in this section, in Figure 4.4). The pattern is defined either by Kapton tape for individual cells or by photoresist using a mask for bulk fabrication and etched in an acid solution. Onto the prepared electrode layer is deposited the alignment layer. In ZBD, the alignment of each cell surface is different. One surface uses an un-rubbed polymer coating to give homeotropic alignment by standard methods; the other features a micron-scale alignment grating embossed to cover the electrode. Alignment on the grating surface will be discussed in Chapter 5.

Depending on the experiment for which they are built, cells may be constructed individually or through a batch process. Much of the processing is the same; glass cutting and assembly/spacer method will differ. In general, batch processing results in higher throughput and more consistent products, but is not always possible. The following is the processing method for batch cell assembly.

Before assembly, the glass is thoroughly cleaned to remove any foreign matter which could *a*) contaminate the LC material and *b*) disrupt the alignment across the cell. This proceeds as follows:

- Sonication in deionized (DI) water and soap (30 minutes),

- DI water rinse (three times, more if suds remain),

- Sonication in DI water (20 minutes),

- Air gun dry,

- Sonication in methanol (20 minutes),

- Air gun dry,

- Sonication in isopropanol (IPA) (20 minutes),

- Air gun dry,

- UV-O_3 treatment (5 minutes).

The final UV-ozone treatment is completed directly before surface treatment or assembly. From the IPA step or earlier, this process is completed within a clean room. The samples remain within the clean room until assembly is complete, when the empty cells are removed for filling and analysis.

4.1.1 Substrate one: homeotropic

Surface treatment using polyimide alignment coatings is performed using a spincoater. Alignment for the work in this thesis is homeotropic. The polyimide, Nissan chemical's SE1211, is thinned first with n,n-dimethylformamide to 20 % by weight. A single drop of the polymer is applied to the clean glass, held onto the spincoater using a vacuum, and an initial spin begins at 500 rpm. After 10 s, the spincoater accelerates to 3000 rpm for 2 min. This results in a thin film coating of the chosen polyimide on the order of tens of nanometres. The glass is then baked at 180 °C for 60 min to evaporate any excess solvent and bond the coating to the glass. Unlike planar alignment layers, the resulting surface does not need to be rubbed to define direction before use.

This glass plate is applied to the glue robot, part of what is termed the Tippler Machine: a home-built kit which is controlled by programs built onto a Raspberry Pi computer (Figure 4.1). A vacuum plate holds the glass in place as the glue pattern of the selected program is applied. Movement of the vacuum stage accounts for the y axis, and movement of the glue arm accounts for the x axis. Since the cells will be capillary filled, the glue pattern needs to have gaps at both ends (see Figure 4.4(a)). For patterned electrodes, the glue should remain outside the electrode area so as not to disrupt the electric field. The glue applied is Struct Bond XN-21-F, a thermal-curing glue. Glue lines are applied narrower than 1 mm.
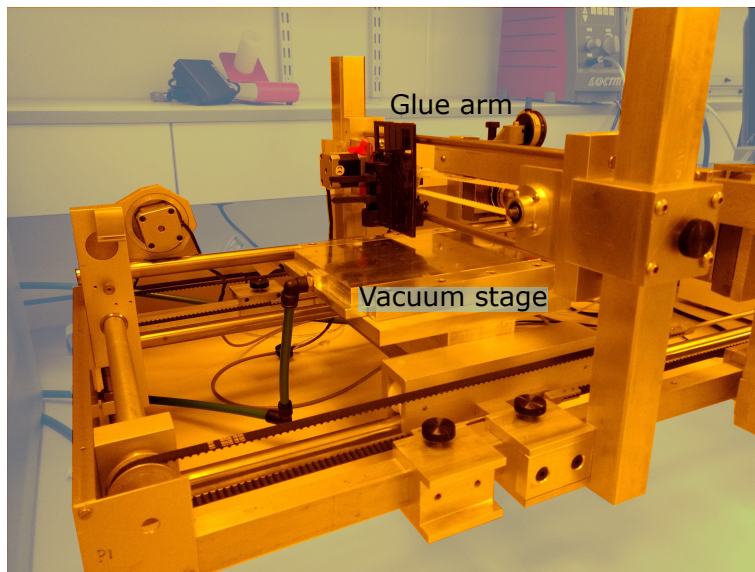
(a)
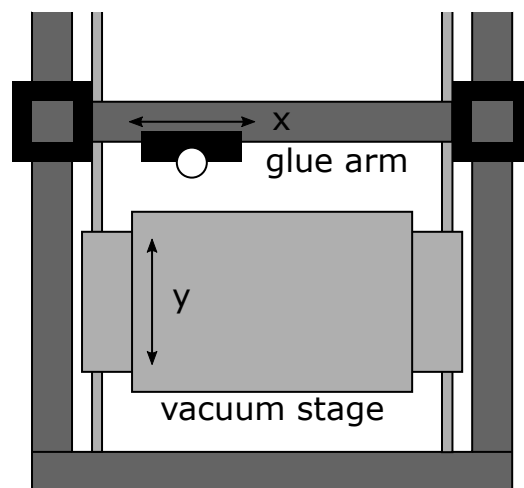
(b)

Figure 4.1: (a) Annotated photograph of the Tippler machine, focused on the gluing aspect. During operation a glue syringe is added to the glue arm and the substrate applied to the vacuum plate. (b) Schemtic of the Tippler machine, top down, indicating the x and y axes for writing the glue pattern.

4.1.2 Substrate two: grating

The grating is applied onto the glass substrate through embossing. An inverse grating composed of resin on a flexible carrier film is used to define the grating shape in UV-curable photopolymer. First, onto the cleaned glass is deposited a methacrylate-based adhesion promoter. The adhesion promoter ensures that the grating material, once cured, adheres strictly more to the adhesion-promoted regions than to bare ITO glass or the resin on the backing film used to emboss the grating. In order to give the correct grating area - fully covering the electrode but not overlapping the glue regions - the adhesion promoter is printed down using an ink jet printer to the required area. The substrate is heated to 70 °C and then to 90 °C, each for 30 s, to evaporate excess and bond the AP to the glass.

Before embossing, in conjunction with the adhesion promotion step performed on the glass substrate, the film master is passivated in a UV-O_3 cleaner. The ozone is needed here, not the UV. After running the cleaner for 5 min, the UV source is turned off and the film added. The passivation process involves the ozone reacting with trailing acrylate groups in the resin. This prevents them from bonding to the methacrylate-based photopolymer, further helping release the grating from the film after curing.

The final grating is composed of embossed photopolymer. Unless otherwise stated, this was one of six 'strengths' of photopolymer derived from the mixture of two proprietary homeotropically-aligning photopolymers developed by Display-Data. These strengths correspond to the anchoring energy of the materials, as will be shown in Chapter 5.

Embossing proceeds on a purpose-built machine. This is performed by a 5 cm diameter steel roller covered in 5 mm thick rubber coating of shore hardness 70 (shore A scale [48]) atop a flat steel carrier plate for the samples. The embossing process is summarised in Figure 4.2. The substrate is placed onto the embossing machine and the pressure and speed set. For the homeotropic photopolymers, these were set to 4 bar pressure (800 N downward force) and speed setting 25,

(a)

(b)

(c)
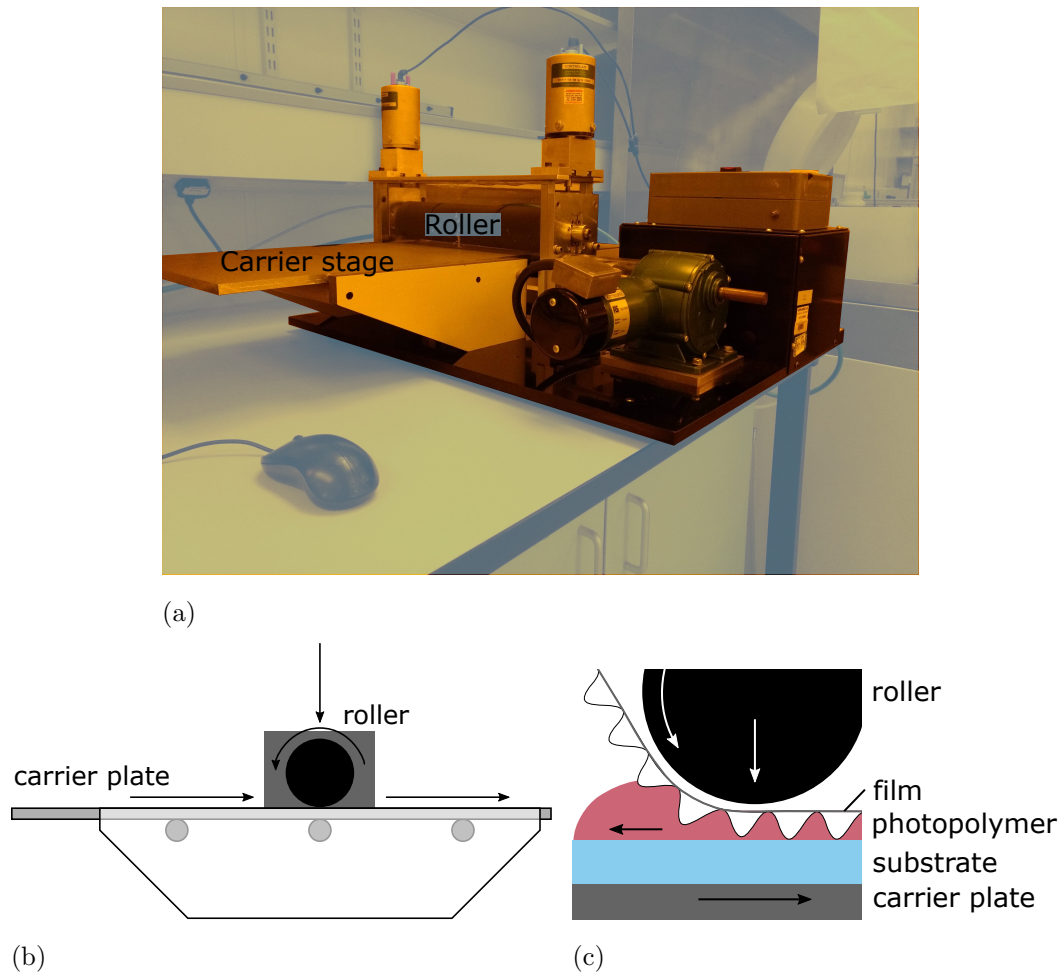
Figure 4.2: (a) Annotated photograph of the embossing machine. (b) Side-on schematic of the embossing machine. (c) Diagram of embossing showing an enlarged grating on film deforming around the roller. Also shown is the fluid front of the photopolymer being pushed out from under the grating master.

or 0.4 cm/s. Photopolymer is placed using a pipette at the leading edge of the glass, and the film added grating-side-down on top. The carrier plate then moves through the embossing roller, taking the substrate with it. Once the grating is embossed excess photopolymer is carefully wiped away and the plate taken to the UV curer. It is exposed for 4 min at 2.5 mW/cm^2 and the film removed. An example of the resulting embossed area can be seen in Figure 4.3.
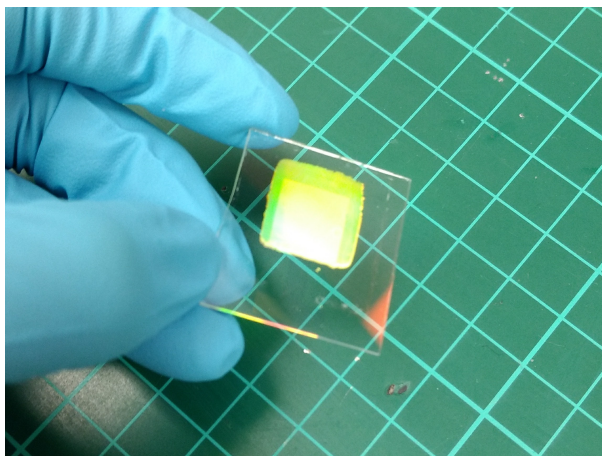
Figure 4.3: Photograph of a single electrode spade and embossed grating for single-cell fabrication.

Spacer beads are applied to the grating side. The glass plate is placed within the spacer bead deposition box, which is fronted by a magnetic-sealing door and includes a single inlet pipe. With the door sealed shut, a measured amount of spacer beads are deposited into the inlet pipe; most commonly, 4 mg of 5 µm diameter silica beads is used. A consistent density of spacer beads is the aim; should the experiment require thinner cells, less mass of smaller beads is used, and the reverse for thicker cells. Compressed air is then forced into the chamber to distribute the beads. At least ten minutes should elapse before the chamber is disturbed to allow time for the beads to settle. This chamber is also grounded to prevent the build up of static charge affecting bead distribution. For the experiments in this thesis, cells of nominally 7, 5, and 2 µm spacing were produced.

Both glass plates are now brought together, aligned by eye, with the glue face on top (Figure 4.4(b)). The plate coated in spacer beads should remain as level and undisturbed as possible. Once together, the unit is covered in a single layer of aluminium foil and placed inside a vacuum bag. The air is evacuated and the bag sealed. In this way, enough pressure is applied to the plates to bring them together, but not enough to crush the spacer beads, and so the cell spacing is selected at the spacer bead diameter (Figure 4.4(c)). The grating photopolymer is soft enough that the glass spacer beads will push through it to contact the

(a) (b) (c)
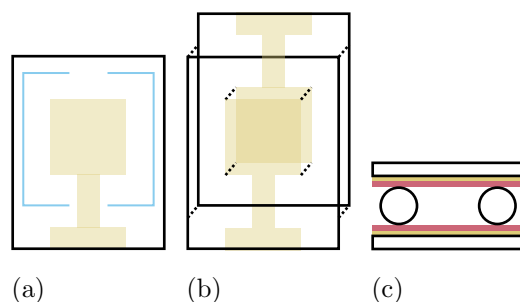
Figure 4.4: Stages of cell fabrication. a) shows a single spade electrode, represented in yellow (actual size) and indicates the glue pattern for capillary filling. b) demonstrates the assembly of a single cell, overlapping the central electrode with opposing bonding ledges for wires. c) indicates the uniform spacing given by the use of spacer beads. Here the electrode is shown in yellow and the alignment layer in pink.

glass on the other side. Without the foil, one could observe the fringes between the plates to determine if the cells were level at a glance. However, the vacuum bags which are compatible with the vacuum bag machine available begin to melt at the glue cure temperature, and so the foil is added to protect the cells.

The combined plates are now cured at 130 °C for two hours. Since the softening bags release the pressure of the vacuum over time, metal weights are added to maintain pressure throughout the process.

Once the glue is cured, the assembled glass plates can leave the clean room for singulation: a glass scribe wheel on an x-y stage is used to score the glass on both sides to define the cell boundaries, and each cell is carefully prised apart from the unit. Individual cells are then sealed in bags to protect from contamination, ready for use when needed.

When individual cells are made, instead of using spacer beads, typically spacer film or spacer glue is used. Both of these methods use a UV-curing glue rather than thermal; the first achieves defined spacing through thin sheets of polyester, the second through spacer beads mixed into the glue.
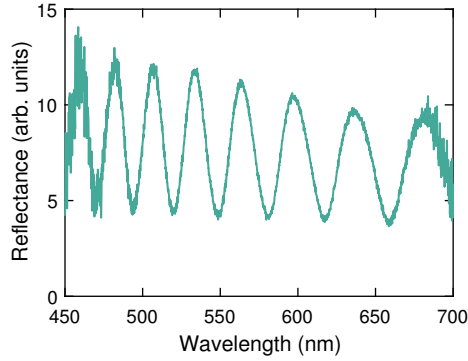
Figure 4.5: Example spectra found for a corner of a nominally 5 µm cell.

The cell gap is defined by the spacers used but may deviate from expectations or vary within the cell. Therefore, before filling, the cell gap is measured using reflection spectrometry, using an Ocean Optics HR4000 high resolution spectrometer. Interference spectra indicate the cell spacing from the formula:

$$d = \frac{m\lambda_1\lambda_2}{2(\lambda_2 - \lambda_1)}. \tag{4.1}$$

Here, d is the cell gap, λ_1 and λ_2 are the first and last peaks observed in the visible range, and m is the number of peaks between them (Figure 4.5). To find the average overall cell gap, five points are measured around the cell and the mean and standard deviation of those values are taken. The mean deviation for ZBD cells measured in this way was 0.7 µm. This uncertainty far outstrips contributions from noise in the spectra or precision in the spectrometer. In ZBD cells, unfortunately, the presence of the grating in the centre of the cell means that the central cell gap measurement cannot be taken.

This method does not take into account the alignment layers and ITO on the glass. Due to their small relative thickness to the cell gap, their effects are considered negligible. However, this assumption begins to fail at low cell gaps.

4.2 Polarising Optical Microscopy

4.2.1 Basic principles
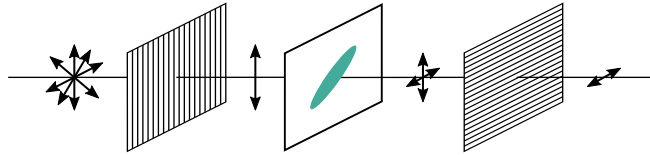
Figure 4.6: Schematic view of the light path in polarised optical microscopy, showing incident unpolarised light shone through a linear polariser, birefringent sample, and linear analyser in turn.

Optical observations form part of most experiments in this thesis. Wherever optical observations were included, they were conducted using a polarised optical microscope (POM). This setup is almost identical to a standard optical microscope with two notable differences: use of a rotation stage in place of a translation stage, and linear polarisers sandwiching the sample in the light path (Figure 4.6).

An optical microscope may be operated in two modes: reflection and transmission. For this thesis, transmission mode is used. Here, the light source is operated beneath the sample, which the light passes through before reaching the objectives. Polarisers sit above and below the sample stage (polariser beneath and analyser above). These are able to rotate and their angles are noted. Typically, they are oriented orthogonal to each other as 'crossed polarisers.' In this configuration, only birefringence is visible through the objectives, and the rest of the field appears dark: optical extinction. Birefringent material may also appear dark through crossed polarisers if its optic axis is aligned parallel to one of the polarisers or orthogonal to the sample plane, such as a homeotropically aligned LC.
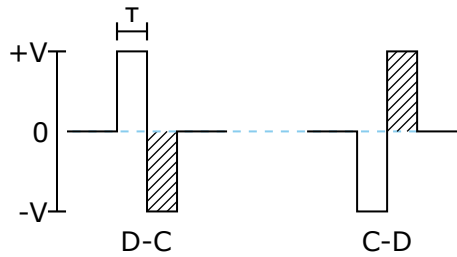
Figure 4.7: Schematic of the bipolar latching pulses for C-D and D-C latching. Labels are included for the amplitude V and the pulse duration τ. The duty cycle for the pulses is 1/2000 with reference to the single pulse duration τ.

4.2.2 ZBD impulse measurements

Much of the work done to characterise the operation of the zenithal bistable device is done under POM using a Leica DM 2700P model microscope. The device is evaluated as per the impulse value required to latch between states; that is, the values of pulse duration τ and pulse amplitude V taken together. This is typically referred to as the τV curve: two data sets, one each for the CD and DC latches, are presented on horizontal voltage and vertical time axes. The sign of the voltage component is taken from the trailing pulse of the waveform: positive for latching from C state to D, and negative for D to C (Figure 4.7).

The bipolar pulses are written in the software for the waveform generator, the WFG500 from FLC electronics. One channel has the C-D pulse programmed, and the other the D-C. Both waveforms have a 1/2000 duty cycle and can be programmed to loop continuously or else be applied as bursts on command. The channels are connected alternately to the cell using a switch box connected to wires soldered to the ITO electrodes on the cells. Electric fields are applied and removed in tandem with POM for in-situ observations.

Each data point is found by setting a constant pulse duration, such as 500 μs, and scanning different pulse voltages in intervals of 0.05 V, checking after each to see if the pixel has latched or not (Figure 4.8). The cell is held at a constant temperature throughout the test using a temperature controller. The first datum to be noted is the voltage at which a partial latch is seen. Sections of the grating
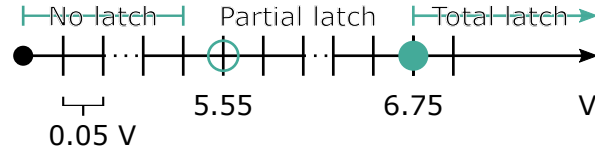
Figure 4.8: Snapshot of a τV curve for $\tau = 500$ μs, indicating the 0.05 V intervals at which the latch state is evaluated, and the data points gathered for the first onset of latch and the full latch point.
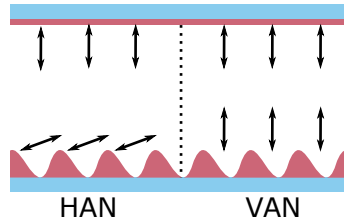
Figure 4.9: Average director alignment at both surfaces of a ZBD cell operating in a HAN/VAN configuration.

profile within the field of view will latch at a lower voltage than others due to nanoscale differences in the grating profile and variations in the cell gap (Equation 3.4. After the partial latch, the pulses are increased in voltage until the full pixel latches into the desired state. The full latch point is the data point used in the τV curve.

The distinction between the two states is made possible due to POM. The primary display mode used in the test cells is HAN/VAN, where the C state corresponds to VAN and D to HAN (Figure 4.9). With the grating vector oriented at 45 ° to crossed polars, the HAN/D state is bright and the VAN/C state dark, and so the latch can be distinguished (Figure 4.10).

4.3 Conclusion

Here ends the introductory matter of the thesis. Experimental methods were presented in overview; for the majority of experiments, cells were constructed and filled for use in electro-optic impulse characterisation using POM and a waveform
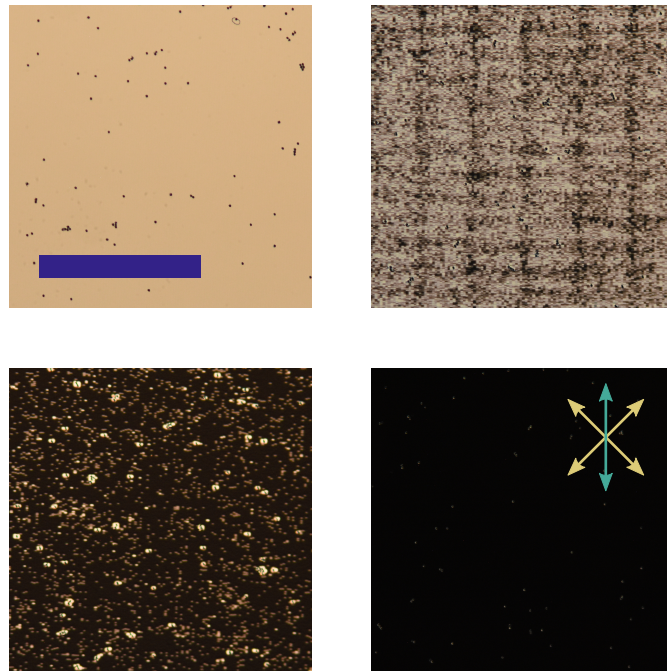
Figure 4.10: Microscopy images of the two latch states and two partial latch images. Scale bar indicates 500 µm, yellow arrows indicate crossed polarisers, and the teal arrow indicates the grating vector at 45 °to the polarisers. The top left image shows the D state, top right a D-state majority partial latch, bottom left a C-state majority partial latch, and bottom right the C state. Spacer beads are also seen in the field of view.

generator. More specifics, when required, will be presented in the following four results chapters. The first two comprise Part 2 of the thesis: Characterising ZBD.

Chapter 5

Characterisation of bistability in ZBD

5.1 Electrical characterisation of ZBD

As previously outlined in Chapter 4, the primary method of assessment for the zenithal bistable device is a probe of its electrical performance, namely the threshold impulse values which allow selection of either bistable state. These data across a range of voltages and pulse widths are collected together as τV curves. This range is defined first by the choice of pulse durations, which in this work were between 100 µs and 5 ms, which then correspond to the threshold voltages.
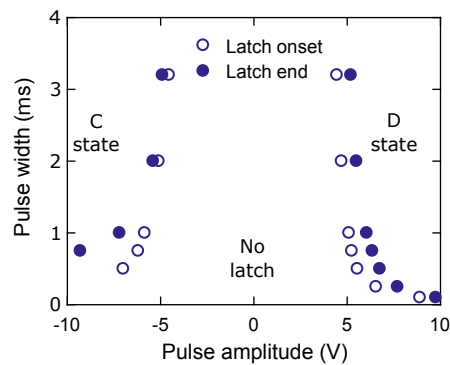
Figure 5.1: Full τV curve for the display mixture MLC6204-000 at 30 ˚C.
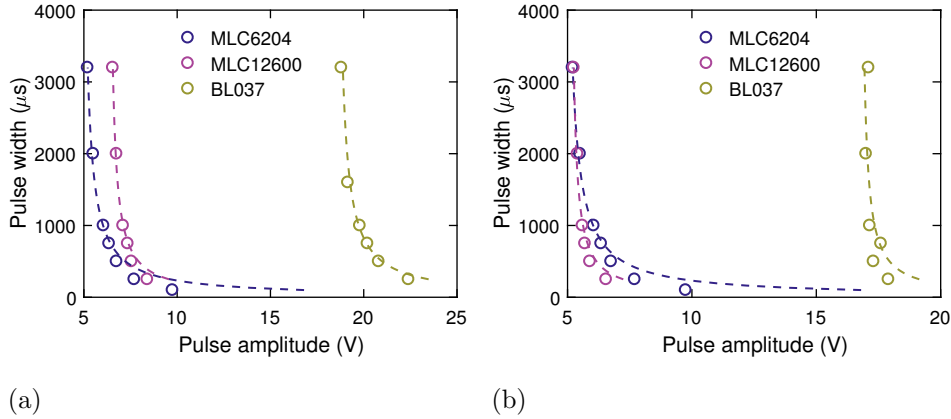
Figure 5.2: Comparison of C-D latching in three display materials: MLC6204-000, MLC12600-000, and BL037. Data were taken at a) $T = 30$ °C and b) $T = 0.9T_{NI}$ (K). The dashed lines represent a reciprocal fit of the data. There is an uncertainty of the latching voltages of ± 0.05 V.

In full, these curves include data for the onset of latch and for latch completion, both for C-D (positive) and D-C (negative) latching. An example is given in Figure 5.1. The sign for the voltage here refers to the trailing pulse of the bipolar waveform.

The most influential parameter in the performance of the ZBD, assuming commercial grating shape, is the choice of the liquid crystal material. This choice determines the operating temperature range as well as the values for the τV curve. In Figure 5.2 a comparison is shown for three materials: two mixtures optimised for their dielectric anisotropy MLC6204-000 and MLC12600-000, both greater than 20 when measured at 30 °C, and a third, BL037, optimised for optical anisotropy of around 0.3 at the same temperature. To compare, the dielectric anisotropy of BL037 is around 10 and the optical anisotropies of MLC6204 and MLC12600 are each around 0.1. Measured properties for these materials are summarised in Table 5.1. Included in the plots is a reciprocal fit of the form $\tau = \frac{A}{V-B}$, where A and B are the fitted parameters and τ and V are as defined previously. We know from [40] that the reciprocal relationship can be further

50

defined by the following equations:

$$\tau = \frac{\gamma_1 l_s d}{(e_1 + e_3)(V - V_{th})} \tag{5.1}$$

and

$$V_{th} = \frac{2W_\theta d}{(e_1 + e_3) + \sqrt{\epsilon_o \Delta \epsilon K_{33}}}. \tag{5.2}$$

Here, γ_1 is the rotational viscosity of the liquid crystal, l_s is a surface viscosity term known as the liquid slip, d is the cell spacing, $(e_1 + e_3)$ is the flexoelectric sum, and V_{th} is the threshold voltage, which is dependent on the anchoring strength W_θ, the permittivity of free space ϵ_o, the dielectric anisotropy $\Delta \epsilon$, and the bend elastic constant K_{33}. These equations have been simplified from their original forms under two assumptions: first, that the grating height is small relative to the overall cell gap, and second that the offset of the grating from the cell surface is negligible. Under most conditions, we find these assumptions to be valid.

The two MLC mixtures perform similarly at the two temperatures, whereas BL037 is seen to require significantly higher latching voltages. This is, coarsely, the most immediate measure of how 'good' the bistable display is: how low is its threshold operating voltage for a given cell gap? As we can see in Equation 5.2, this value is directly affected by the anchoring strength at the grating surface and the cell gap. Increased flexoelectric sum, dielectric anisotropy, and bend elastic constants will also decrease this value. A lower value for the second fitting value, which determines the shape of the reciprocal curve and is defined by $\frac{\gamma_1 l_s d}{(e_1 + e_3)}$ (as per Equation 5.1), is also important for performance, most notably when differentiating between LCs with similar values for V_{th}. Optimising this value requires balancing the flexoelectric sum against the viscosity.

Cell gaps at the display stage, once the LC material has been chosen, are decided by the optics. ZBD devices for commercial use are operated in the TN/HAN configuration, and cell gaps as such are targeted for maximum transmission at wavelengths of $\lambda = 550$ nm. This will give an optically white state for TN. The

5. CHARACTERISATION OF BISTABILITY IN ZBD

transmission maxima are found using the Gooch-Tarry expression for crossed polarisers:

$$T = 1 - \frac{\sin^2\left(\frac{\pi}{2}\sqrt{1 + \left(\frac{2\Delta n.d}{\lambda}\right)^2}\right)}{1 + \left(\frac{2\Delta n.d}{\lambda}\right)^2}.$$ (5.3)

At the designated wavelength $\Delta n.d$ should be selected such that the expression is maximised. Typically, one of only the first two minima in cell gap is used. This in turn minimises the threshold voltage, which is linear in cell gap [1].

	T_{NI} (°C)	30 °C		0.9*T_{NI}	
		Δn	$\Delta \varepsilon$	Δn	$\Delta \varepsilon$
BL037	113	0.3	13	0.27	11
MLC12600	94	0.09	22	0.08	17
MLC6204	64	0.11	26	0.11	26

Table 5.1: Material parameters at 30 °C and at 0.9*T_{NI} (K) for the three display mixtures. Optical anisotropy was measured using a Berek compensator and dielectric anisotropy was measured using a dielectrics bridge. Both have an associated uncertainty of 10 %.

By offsetting the fitted threshold values for each material by the measured cell gap to give threshold field, we are able to extrapolate new threshold voltages at the cell gaps for Gooch-Tarry maxima. These values are presented in Figure 5.3 based on the parameters given in Table 5.1. We see that the increased birefringence of BL037, while it does allow us to access lower cell gaps, does not offer any improvement in operating voltages at its cell gap maxima. At each temperature, MLC6204 offers the best combination of appropriate cell gap and lower voltage operation. Practically, cell gaps greater than 2 µm are best to target.

Choice of material is ultimately dominated by the threshold voltage, and therefore high dielectric anisotropy, bend elastic constant, and flexoelectric sum are paramount for the LC. For bistable applications, rotational viscosity is ultimately less important as fast response times are not crucial. When choosing

Figure 5.3: Plot of the calculated Gooch-Tarry curves for the display materials at a) 30 °C and b) $0.9*T_{NI}$ (K). Included are tags demonstrating the extrapolated threshold voltages for the cell gaps at maximum transmission up to 8 µm.

between two similar materials, birefringence may be used to discriminate between them; however higher birefringence will not compensate for the remaining governing properties of the device.

5.2 Investigating the role of anchoring strength

When evaluating the results of fitting the τV curves to the equations 5.1 and 5.2, it becomes possible to use bistable latching to determine parameters of note. Liquid crystal parameters may be evaluated in any number of ways; however, the LC-surface interaction terms (anchoring strength W_θ and liquid slip l_s) are of unique interest. Should the LC and device parameters be well-known, we can use the fitting to find these two parameters. Homeotropic anchoring strength measurements at nano- and micro-scale structures pose unique difficulty, and the liquid slip parameter is rarely mentioned or measured with regards to liquid crystal devices. The following results and discussion were presented previously in the journal Langmuir [41].

53

5. CHARACTERISATION OF BISTABILITY IN ZBD

Anchoring strength at the surface boundary allows for controllable alignment of the liquid crystal material, which is essential for LC optical applications. Stronger anchoring is typically prized for displays. However, bi- and multi-stable display devices often operate by breaking the surface anchoring or else manipulating it, requiring weak and intermediate strengths instead. These technologies include the zenithal bistable display [33], the azimuthal bistable nematic [22, 26], the π-twisted bistable nematic (or BiNem®) [15], and ferroelectric liquid crystal displays [49, 50]. Many methods of measuring the anchoring strength have been developed through the years; they vary in intricacy and both homeotropic anchoring and anchoring at non-planar surfaces are historically more difficult to measure. The most straightforward method of measurement comes from finding the correlation length associated with electrical or magnetic reorientation of the director field [51, 52, 53]; however, using this method in a homeotropic device requires negative dielectric materials with large anisotropy, since it is these materials which will reorient under applied fields in homeotropic devices. In the absence of external fields, the anchoring strength can be measured through characterisation of the director profile through dynamic light scattering [54, 55]. This often utilises specific cell geometries, such as a wedge cell [56]. By using the fitting from ZBD latching curves to measure the anchoring, standard positive materials and the unmodified display device may be used.

Instead of the aforementioned display mixtures, these experiments were conducted with the ubiquitous nematic LC 4-cyano-4'-pentylbiphenyl, also known as 5CB. It was the first stable room-temperature nematic liquid crystal and a wealth of characterisation data is available in literature. Crucially for our tests, data exists of the flexoelectric sum, including temperature dependence. Flexoelectric behaviour is notoriously difficult to measure accurately due to challenges de-coupling the effects from the dielectric and ionic responses of liquid crystals. When it is measured, there are large uncertainties involved and rarely are measurements taken for nematic mixtures. Literature values for 5CB at 25 °C used were: $(e_{11} + e_{33}) = 14.5$ pC/m [57], $\gamma_1 = 0.099$ N s/m^2 [58], $\Delta\epsilon = 13.15$, and $K_{33} = 8.25$ pN [9].

A full investigation of the anchoring behaviour follows. Homeotropic anchoring at the grating surface was achieved by two means: the first was using a proprietary homeotropically-aligning photopolymer (used with permission from DisplayData Ltd) to compose the grating; the second was using a three-component photopolymer and surface treating the grating after fabrication for controllable alignment.

5.2.1   Anchoring strength and polymer concentration

In the case of the proprietary photopolymers, two such were mixed to investigate their effect on anchoring as a function of concentration. The weaker-anchoring component will be referred to as photopolymer A (PPA), and the stronger component photopolymer B (PPB). Anchoring strength was then determined by evaluating fitting parameters and removing known values such as device and LC parameters. Further results where then investigated as a function of temperature.

Cells were constructed with gratings composed of five different photopolymer mixtures: 100 % PPA, 27 % PPB, 40 % PPB, 59.5 % PPB, and 100 % PPB (polymer concentrations measured by weight, PPB in PPA). The cells were held at 25 ± 0.1 °C and had cells gaps of nominally 7 µm. Presented in Figure 5.4 are two examples of the τV curves taken and the fitted curves based on Equation 5.1.

Anchoring strength as measured is seen to be linear with polymer concentration (Figure 5.5). That is, as higher concentrations of PPB are added to the grating composition, the anchoring strength is seen to increase linearly. As measured here, much of the mixtures are what would be considered intermediate anchoring (of the order 10^{-5} J/m^2), while the pure PPB would be considered strongly anchoring.

Cells of two photopolymer compositions were then re-examined at different temperatures and new devices of different cell gaps were tested. As it is a surface interaction term, the anchoring strength was expected to depend on temperature.
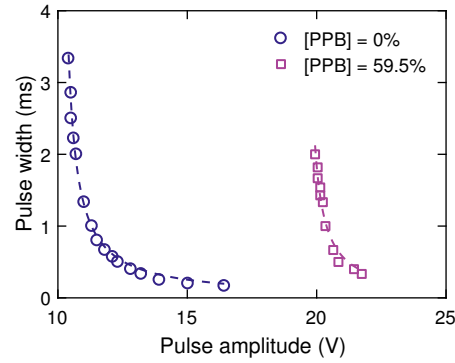
Figure 5.4: An example of two fits of CD latch from 5CB: the first of the lowest anchoring strength, the second of an intermediate strength. The fits are of the form given in 5.1.
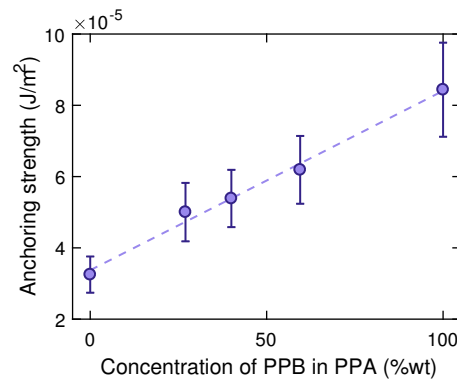
Figure 5.5: Plot of anchoring strength versus photopolymer concentration for the homeotropically-aligning photopolymers. The linear fit shown is $W_\theta = 3.4 \times 10^{-5} + 5.0 \times 10^{-7}[PPB]$.
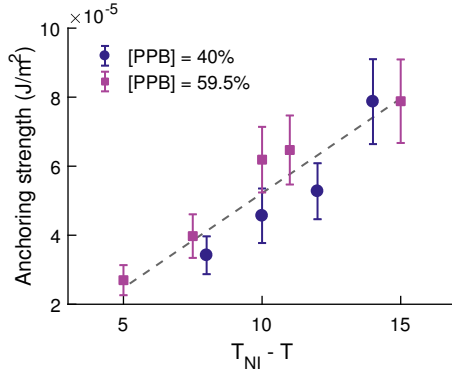
Figure 5.6: Plot of anchoring strength versus reduced temperature, $T_{NI} - T$. An empirical linear trend for the combined data, of $W_\theta = 5.5 \times 10^{-6} \times (T_{NI} - T) - 2.7 \times 10^{-6}$, is included as a guide.

As for cell gap, the parameter is included in the calculations, and so fluctuations here would have to be considered carefully to preclude any issues with the theoretical framework.

Anchoring strength was found to decrease with increasing temperature (Figure 5.6). Unfortunately, 5CB has a narrow nematic range (18 - 35 °C). ZBD operating temperatures narrow the experimental range further - both the lowest and highest anchoring strength polymer samples had such narrow bistable ranges that they could not be utilised to give significant data with respect to temperature. However, evidence from these two samples is sufficient to conclude an approximately-linear temperature dependence. In the figure a linear fit is shown for the combined data of both photopolymer concentrations, giving a slope of $(5.5 \pm 0.8) \times 10^{-6}$ J/(m²°C) which can be accepted within error for both datasets. This suggests that the temperature dependence of anchoring strength - the slope of the trendline - is the same across the different strength polymer mixtures, and that only their ranges differ. This suggests that the temperature dependence of the anchoring strength is a result of the LC material component of the LC-surface interaction, and that the surface itself is responsible for the overall range in each case, i.e. the intercept.
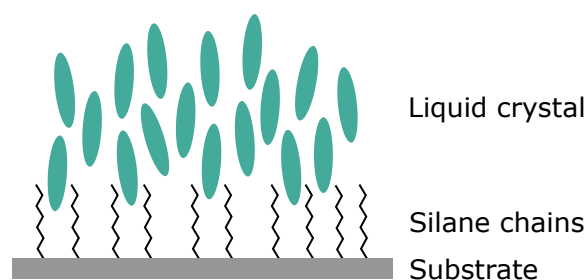
Figure 5.7: An illustration of homeotropic alignment using silane on a planar substrate.

5.2.2 Anchoring strength of silanated gratings

The second homeotropic alignment technique investigated was that of silane surface treatment of a three component photopolymer grating. Once treated, pendant chains from the silane provide homeotropic anchoring at the grating surface. This is illustrated for a planar surface in Figure 5.7. The grating surface was treated with trichloro-octyl silane (C8) vapour, varying exposure times. As this quantity was determined by the experimental setup and thus specific to local laboratory conditions, the treatment was further quantified through surface studies using X-ray photoelectron spectroscopy (XPS) and atomic force microscopy (AFM).

The photopolymer PP2 is a mixture of acrylate monomers Sartomer 508 (57 % by weight) and Sartomer 349 (38 % by weight) with 5 % of the photoinitiator Genocure LTM. Due to the presence of precursor impurities in the grating components (hydroxy-terminated monoesters), the silane has uniform covalent bonding sites across the grating surface. Chemical structures of the photopolymer components and the precurser impurities are given in Figure 5.8.

Gratings were exposed to controlled amounts of C8 silane vapour by varying the exposure time. Before exposure, the gratings were cleaned in a UV-O$_3$ chamber for 5 minutes. From here, surface treatment proceeded using the silane rig, shown in Figure 5.9. Substrates with exposed gratings were placed onto a sample holder rotating at approximately 10 rpm within a dessication chamber.

(a)

(b)   (c)

(d)

(e)
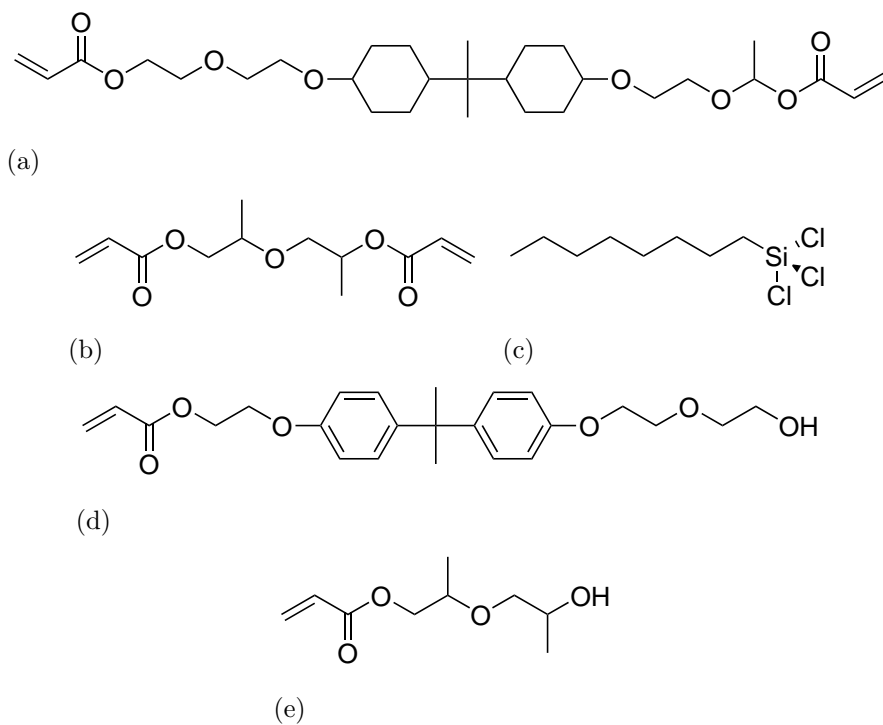
Figure 5.8: Chemical structures for the monomers of photopolymer 2 (PP2): (a) Sartomer 349, (b) Sartomer 508, and (c) the surfactant trichloro-octyl silane (C8). Also presented are the monoester impurities of Sartomer 349 and 508, (d) and (e), respectively. These impurities were measured at 4.9 and 6.8 % by weight within the components as sold.
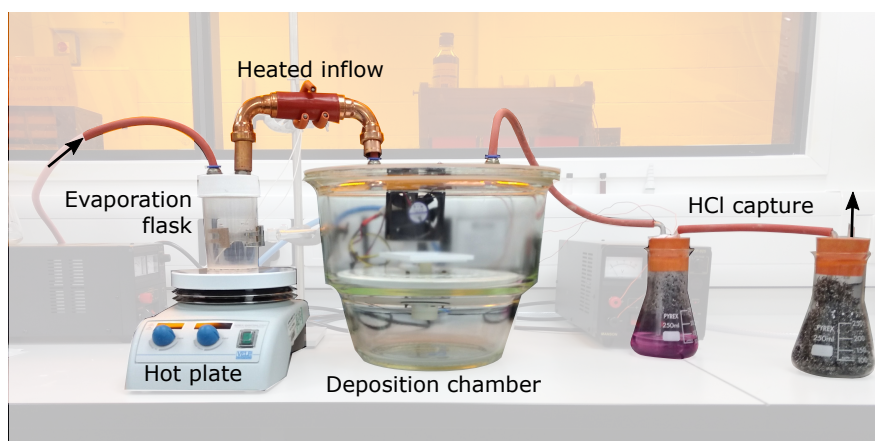
Figure 5.9: Photograph of the silane rig used for surface treatment. Arrows are included to indicate airflow direction within the system.

Connected to this chamber was an evaporation beaker, heated to 80 °C, wherein 20 µL of C8 silane was evaporated. Compressed air at 0.8 bar pressure flowed through the system at 0.01 m³/s, carrying silane vapour from the flask to the dessication chamber. The inflow pipe is passed through a heated copper pipe (held at approximately 80 °C) to prevent premature condensation of the vapour. An 8 cm diameter fan further circulates the air within the deposition chamber to maintain uniformity. Finally the remaining vapour exits the chamber through a chlorine capture system, consisting of indicator solution and steel wool. This prevents excess chlorine gas building up in the laboratory and prevents corrosion of any exposed metal from condensing HCl vapour.

After the elapsed time, the substrate is baked at 180 °C for one hour to complete the reaction. The silane rig is cleaned thoroughly with acetone and isopropanol to prevent build up of surfactant, which would alter the chamber's surface area. Cell assembly then progresses as normal. Once cells are singulated, their τV curves are evaluated.

Anchoring strength was found not to increase linearly with time (Figure 5.10). Instead, a saturation effect was seen, where the anchoring strength began to approach a critical value. This relationship followed a hyperbolic tangent relation
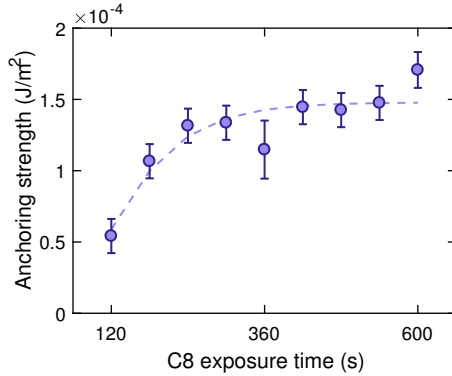
Figure 5.10: Plot of anchoring strength versus exposure time for silanated gratings as measured through evaluation of fitted τV curves. The fitting shown follows the form of equation 5.4 with $W_{max} = (1.5 \pm 0.1) \times 10^{-4}$ J/m^2, $t_0 = 57 \pm 10$ s, and $k = 151 \pm 30$ s.

as:

$$W_\theta = W_{max} \tanh \left(\frac{t - t_0}{k} \right).$$

(5.4)

We see the anchoring strength approach a maximum W_{max} with treatment time t. The threshold for homeotropic anchoring is given by t_0, and k is a fitting constant.

Silanation of the grating gives much higher anchoring strength than that of the PPA/PPB mixtures. This corresponds to much higher latching voltages for the device; for instance, the 600 s exposure time represents an operating voltage of around 45 V for 5CB in a 7 µm cell. However, stronger anchoring is of more general interest in conventional display devices. The intermediate anchoring seen in the proprietary photopolymers can be replicated by restricting the treatment to 150 s and below.

5.2.2.1   Surface characterisation

The surface treatment is performed using off-the-shelf components in a handmade rig, and relies on bonding directly to the photopolymer surface. As such, it is necessary to characterise the surface treatment after the fact, to confirm the silane reaction mechanism and to evaluate the relationship between exposure time and
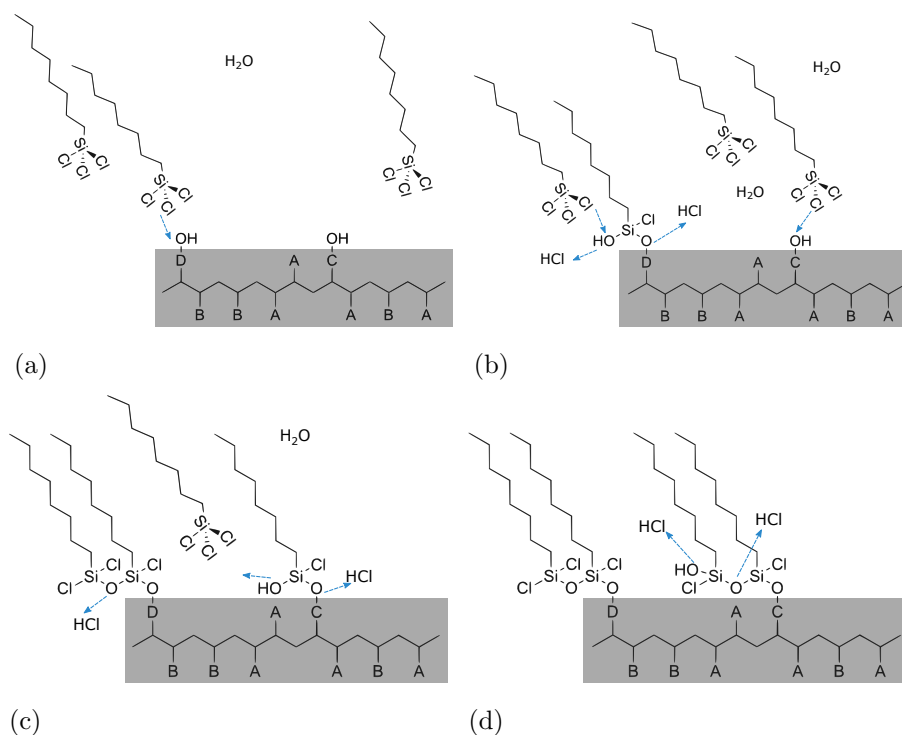
Figure 5.11: Schematic representation of the silanation reaction, progressing from monolayer formation to condensation. The photopolymer surface is simplified as a polymer backbone with branches: A is the Sartomer 349 residual structure, B is the Sartomer 508 residual structure, C is the hydroxyl-bearing Sartomer 349 monoester residual structure, and D is the same for Sartomer 508. These structures appear in full in Figure 5.8.

silane coverage.

In a conventional silane treatment chamber, quantities of silane and water are introduced to the sample under vacuum. Before treatment, the sample is pretreated with oxygen plasma in order to seed OH binding sites on the surface [59]. These surface groups are of an abundance such that the silane deposits as a monolayer, and HCl gas is released. This reaction completes once Si-O-Si bonds between adjacent surface silanes form from condensation reactions [59]. By slowly introducing the silane to the chamber, rare covalent bonds form directly onto the photopolymer. A schematic of this is shown in Figure 5.11. Once the surface

sites are covered, silane continues to react forming a polymer above the surface.

In the first instance, the surface was analysed using x-ray photoelectron spectroscopy. Photopolymer flats, treated in the same manner and instance as the grating samples, were examined. Two silicon peaks were observed in all treated samples, but were absent in the control sample. This indicates that the XPS sees the silane on the surface but does not penetrate the photopolymer to the (borosilicate) glass beneath. Detailed spectra were taken of the Si 2p peaks, and species assigned using literature values. These were judged to be Si-O-Si bonds at 102.5 eV and SiO_2 bonds at 103.3 eV. Examples of the broad and detailed spectra, including fitted peaks, are included in Figure 5.12. We are able to conclude that the silane condensation reaction was complete in each case, as no peaks were seen for Cl_2, indicating all chlorine escaped as a gas. The density of silane across the surface as a function of exposure time correlates well with the anchoring strengths (Figure 5.12(c)). Hence, the silanation time is directly correlated with silane surface density which is linearly related to the measured anchoring strength.

Considering the mechanism of the silanation reaction across the photopolymer surface, there are two possible models. In an 'island' model [60], any initial bonding sites seed islands of strong anchoring, interspersed with bare photopolymer (Figure 5.13(a)). Increasing the exposure time increases the relative size of the islands with respect to uncoated photopolymer, and so the anchoring strength increases. Due to the microscopic scale of the domains, their anchoring is averaged in the liquid crystal surface interaction, giving homeotropic alignment directly proportional to the surface density of the pendant silane groups. In an 'epitaxial' model [61], the silane attaches uniformly across the surface area of exposure (Figure 5.13(b)). The density then increases with exposure time.

Tapping-mode AFM data, as shown in Figure 5.14, indicates a decrease in surface roughness with increasing exposure time, from an initial value of 1 nm to below 0.5 nm. On the 500 nm lengthscale, there is no evidence for silane domains. Additionally, roughness would initially increase following the first model, and so the AFM data leads us to accept the uniform epitaxial growth model. Further

(a) (b)

(c)
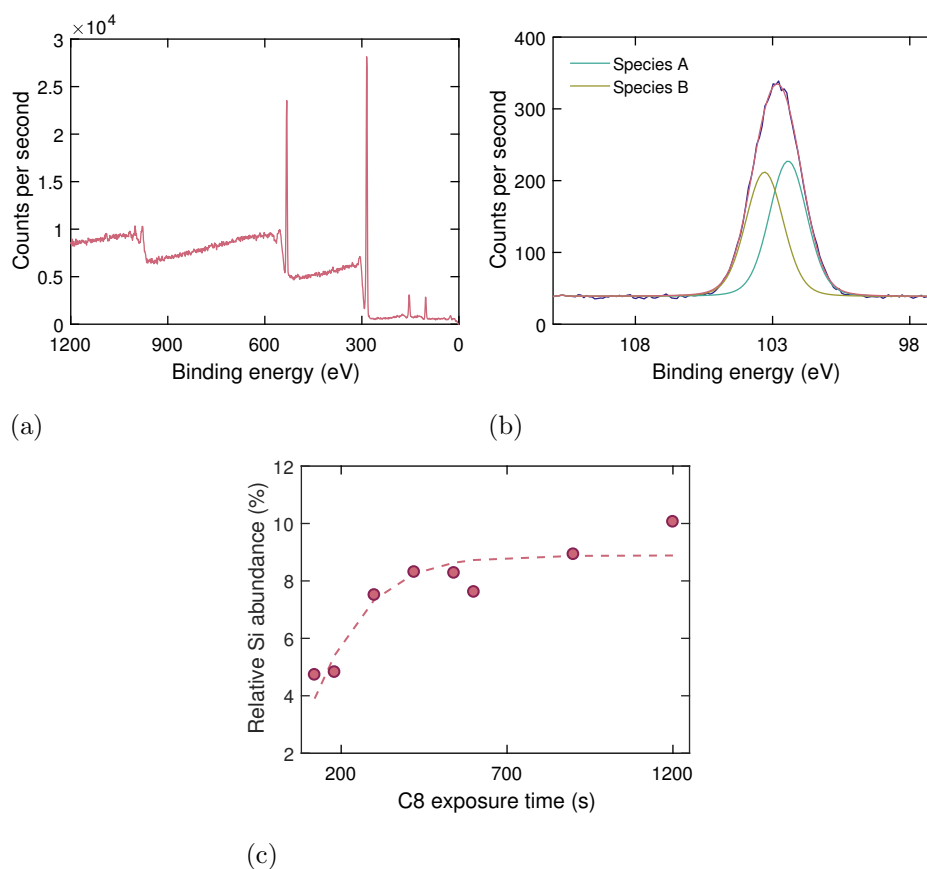
Figure 5.12: XPS data taken for photopolymer flats surface treated with C8 silane. (a) shows the full survey of the sample exposed to 540 s silane. (b) shows the detailed spectra for the Si 2p counts, including envelope and two species fitting (assigned to species A - Si-O-Si and species B - SiO_2). (c) gives the measured Si abundance plotted against treatment time, including a hyberbolic tangent fit of the form of Equation 5.4 with $Si_{max} = 8.8 \pm 0.5$ %, $t_0 = 0$ s, and $k = 260 \pm 20$ s.

(a) (b)
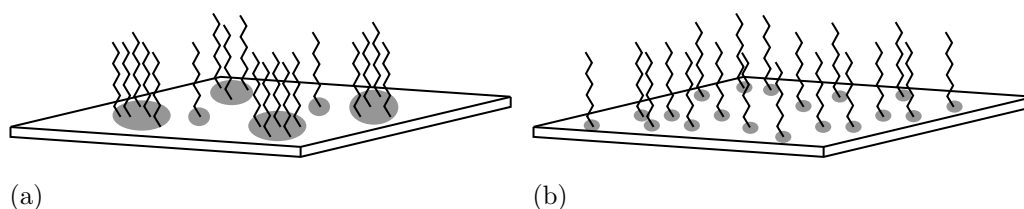
Figure 5.13: Diagrams of (a) island growth silanation and (b) epitaxial. Grey circles are used to indicate total surface coverage.
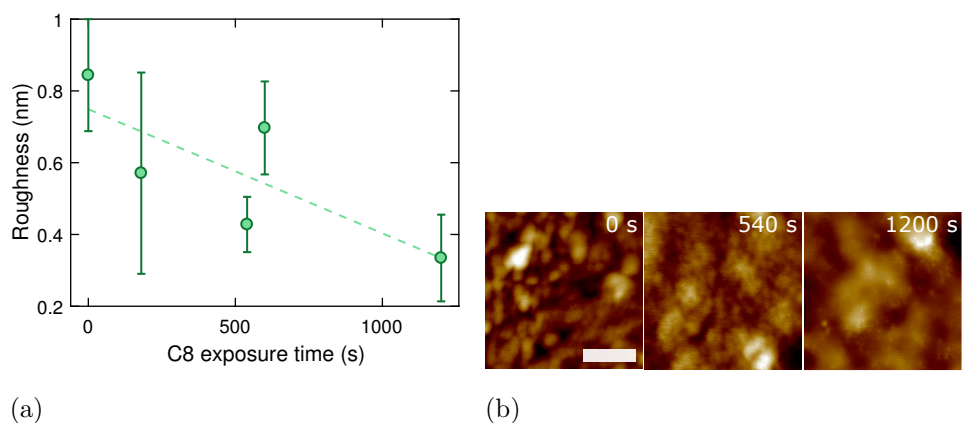
Figure 5.14: (a) shows the measured surface roughness with silane exposure time. Included is a linear fit as a guide: $rough = -3.5 \times 10^{-4}t + 0.7$. (b) displays AFM micrographs of the polymer flats, 500 nm × 500 nm, flattened for analysis. Surface roughness was calculated by averaging multiple 100 nm × 100 nm areas within each sample. A 100 nm scale bar and a colourmap denoting +5 nm (white) to −5 nm (black) are included.

work could test whether this is a property found in any polymer surface, or if it is unique to the sparse hydroxyl groups included in PP2.

5.3 The liquid slip parameter

In addition to using the latching characteristic to measure the anchoring strength at the grating surface, we are also fitting for a parameter known as the liquid slip. This is a term related to the surface viscosity which goes with the inverse of viscosity - viscous fluids have a lower liquid slip value, measured in length units. In liquid crystal systems, the no slip boundary condition is assumed with such regularity it is often not stated. A no slip boundary corresponds to a liquid slip of 0 nm. However, when there is flow at a surface, it can be characterised by an extrapolation length within the surface related to the flow at which a no-slip boundary could be imposed (Figure 5.15)[42]. Previous measurements of the liquid slip parameter within a liquid crystal system are unavailable.
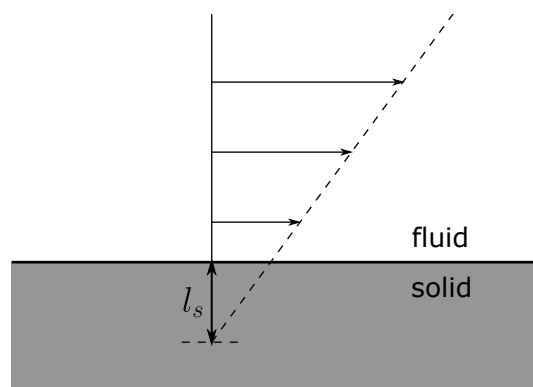
Figure 5.15: A diagram showing the extrapolation of flow to the liquid slip length.

The value is calculated analogously to the anchoring strength, this time using the fitting parameter for the 'slope' of the reciprocal rather than the threshold. This can be seen using Equation 5.1, $A = \frac{\gamma_1 l_s d}{(e_{11} + e_{33})}$.

When calculated for the proprietary photopolymers, PPA and PPB, the liquid slip values are on the order of tens of nanometres (Figure 5.16(a)). They decrease slightly with increasing concentration of the stronger photopolymer, but this reduction is not significant within the range of the errors on the measurement. The slip measured is sufficiently small that it supports the typical assumption for liquid crystals of no slip at the boundaries.

The silane treated photopolymer has measured slip values on the order of hundreds of nanometres; no longer negligible (Figure 5.16(b)). Again they are seen to decrease slightly with increasing exposure time; this time, the decrease is clearer and more significant with respect to the relative errors on the data and the fit. It is hypothesised that the higher values for slip length here indicate a surface region of silane/liquid crystal inclusion, where rarefied silane molecules allow the flow of liquid crystals among them. This flow then decreases as the silane density increases, effectively pushing out the liquid crystal molecules.

These values for the liquid slip should be relevant to other homeotropic liquid

66

(a)   (b)
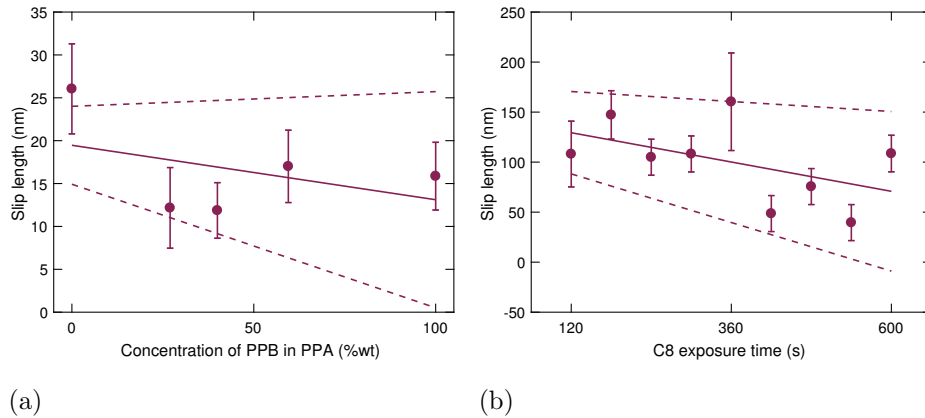
Figure 5.16: Slip length plots for (a) the proprietary photopolymers as a function of concentration and (b) the silanated photopolymer as a function of exposure time. In (a), a linear guide fit is shown as $l_s = -0.06t + 19$ and in (b), $l_s = -0.12t + 144$.

crystal devices, including TV and monitors.

5.4   Conclusion

In the first section, the electro-optic characterisation of ZBD devices was explored in more depth. The characteristic latching values were explored alongside material choice to give a picture for the relative impact of two key material properties in the device: optical and dielectric anisotropy. It was shown that among the three materials considered, MLC6204-000 offered the best balance of performance at the two temperatures considered.

In the second section, the role of anchoring strength was investigated under two different alignment methods at the grating surface. This serves to both indicate the importance of controlled anchoring at the grating surface and to further illuminate the mechanisms involved. This work was possible due to the use of 5CB. The wealth of characterisation literature available meant that values for the material parameters were available at multiple temperatures. Use of mix-

tures of two homeotropically-aligning photopolymers resulted in linearly tuneable anchoring strength in the range $0.2 - 1.0 \times 10^{-4}$ J/m^2. Silanation of another photopolymer surface resulted in a non-linear range of anchoring strengths under variation of exposure time from $0.5 - 2.0 \times 10^{-4}$ J/m^2. An empirical relationship was found that fit this behaviour and correlated well with silane density as measured by X-ray photoelectron spectroscopy. The growth of silane domains was determined to be epitaxial using AFM. Together these two anchoring methods provide a range of anchoring strengths for the device which may be applied to other systems, especially where alignment is required on microstructures in liquid crystal devices.

Finally the third section looked at the liquid slip length for the two anchoring methods. This was found to be negligible in the photopolymer mixtures, on the order of tens of nanometres, and invariant within error to the mixture concentration. In contrast, the silane method gave slip lengths on the order of 100 nm and negatively correlated to silane exposure time. This lends to a conclusion that the slip length is measuring the slip of the liquid crystal molecules between the silane chains, as this would indicate the longer length compared to the photopolymer mixture and would decrease with increasing silane density.

Chapter 6

Defect dynamics in bistable latching

The operation of the zenithal bistable device is accomplished through manipulation of nematic defects. The nucleation and annihilation of $\pm\frac{1}{2}$ defect loops is responsible for latching between the two stable states. However, the scale and position of these defects mean that under standard operation and optical microscopy, it is not possible to actively observe and confirm the defect behaviour. Experimentally, distinguishing the latched states in the partial latch regime can give clues to the dynamics as will be discussed in Section 6.3; otherwise, computational modelling provides an option for 'observing' the defects.

The following chapter represents the bulk of the work done in characterising the defect dynamics of latching in ZBD. Literature on the precise mechanisms during latching which result in defect nucleation or annihilation is scarce, though the theory is well established (Chapter 3). The work on the defects is presented here in four parts through both modelling and experimental efforts. Preceding these is an introduction to the modelling methods using the program QLC3D.

First, the standard latching curves were calculated using the modelling software, and these results compared to experiment. Secondly, a macroscopic view of the defect dynamics is given through experimental examination of the partial latch behaviour of ZBD. Thirdly, a section introduces non-flexoelectric latching,

seen from D-C state, in both modelling and experiment. Finally, the last section provides an in depth look at the behaviour of the ZBD defects in an electric field.

6.1 QLC3D for defect modelling

A modelling program known as QLC3D, developed by Eero Willman during his PhD at University College London [62], was used to investigate defect dynamics in latching. It implements three-dimensional finite element method to model the Q-tensor field in small scale LC devices. As a reminder, the Q-tensor is a tensor order parameter in liquid crystal systems (Chapter 2). The software is specifically refined to model topological defects and to deal with cases of weak anchoring. This program has been used previously to model bistability in the Post-Aligned Bistable Nematic device (PABN) [63], and it has been used to examine the 3-D behaviour of the defect loops in ZBD at grating slips [47].

QLC3D takes inputs of the liquid crystal parameters, the initial liquid crystal orientation, anchoring (direction and strength) at the surfaces, time-dependent electrical potentials, and the properties of any dielectric medium within the device - in this case, the grating. Settings were selected such that the program would simulate the desired time period in full. This was dependent upon the electrical pulses used, but was typically less than 10 ms. Time steps are adjusted at every iteration in order to maintain a constant change in the Q-tensor. When the tensor varies rapidly, the time step is decreased to maintain accuracy, and when it varies slowly, longer time steps ensure efficient running times. The mesh used, which represents a 5 µm ZBD cell with periodic boundaries in x and y (infinite grating), was created by the group at UCL. A diagram of the modelling volume is presented in Figure 6.1. The modelling progresses in three dimensions; however, for the most part the y direction is not considered in this thesis and results are presented as though for a two-dimensional problem. Results presented are of 'slices' taken of the problem in the x-z plane. Hence, the disclination loops will be referred to as two dimensional defects. The program was set to output the director field at every tenth iteration in an effort to reduce data sizes. This was
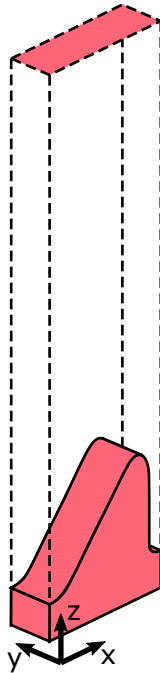
Figure 6.1: Diagram of the modelling volume. Boundaries in x and y are periodic and the top surface in z has homeotropic anchoring.

not found to significantly impact the level of detail found from the simulations, and lent more understanding than simply outputting the final state. Static state evaluations typically took fewer than 100 iterations to complete. Dynamic state evaluations (such as during latching) took up to 5000 iterations, depending on the impulse used. Once the simulation finished, the results were evaluated in the data analysis and visualisation program ParaView.

The primary liquid crystal parameters used are those used in the previous ZBD modelling by Day *et al.* [47], which are taken from the papers by Spencer *et al.* and Jones *et al.* [40, 1]. They represent a material known as mixture B, formulated to out-perform the commercial display mixture MLC6204-000. The parameters are presented in Table 6.1.

Before electrical behaviour could be simulated, the static continuous and de-

71

K_{11}	12.5	pN
K_{33}	7.3	pN
γ_1	0.155	kg m^{-1} s^{-1}
$\epsilon_\parallel$	62.5	
$\epsilon_\perp$	23.5	
$\Delta\epsilon$	39.0	
e_{11}	69	pC m^{-1}
e_{33}	45	pC m^{-1}
a	65 000	J m^{-3} K^{-1}
b	530 000	J m^{-3}
c	980 000	J m^{-3}

Table 6.1: Material parameters for mixture B as used in the modelling, taken from [1, 64]. From top to bottom, they are the elastic constants, the rotational viscosity, the dielectric constants and anisotropy, the flexoelectric coefficients, and the Landau thermotropic coefficients.

fect states were evaluated. For C-state, the bulk director field was initialised as fully homeotropic, with intermediate homeotropic anchoring on the grating surface and infinite homeotropic anchoring on the top surface, and the simulation set to reorient for 5 ms. An analogous process was followed for D-state, except the bulk director was set to fully horizontal (planar) alignment and reoriented for 50 ms. The resulting HAN state, as a hybrid alignment state, took longer to reorient. The resultant director configurations around the grating are shown in Figure 6.2.

(a)   (b)
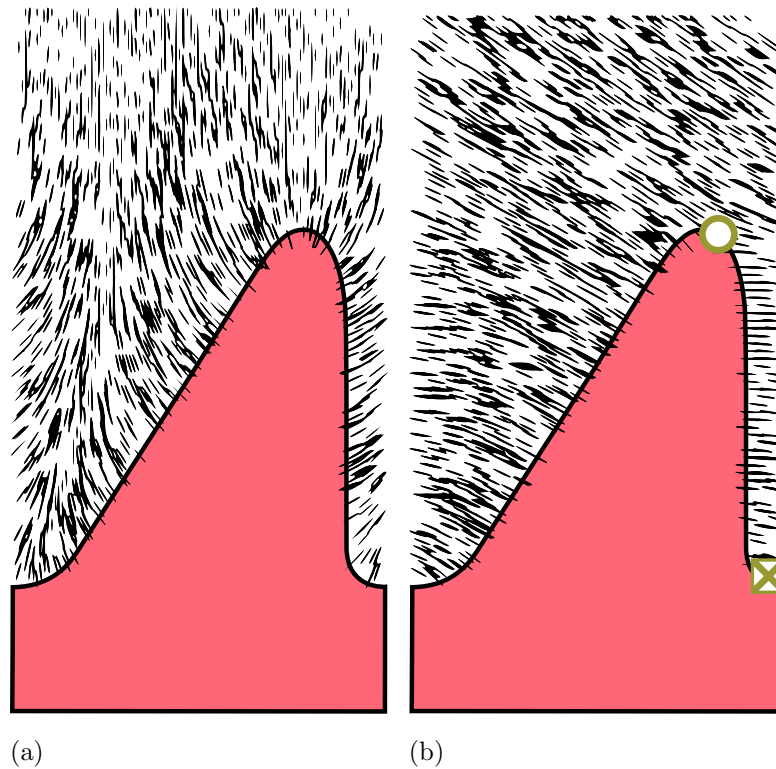
Figure 6.2: Static state director alignments for (a) C and (b) D state as given from modelling in QLC3D. The images were taken as the final iterations in ParaView, showing the director as lines plotted at mesh points at fixed density to increase visibility. Director profiles and the form of the grating were highlighted using image software Inkscape for further visibility. In (b), the two defect cores are highlighted.

6.2 Comparison of latching: computation and experiment

The program makes it possible to input electrical waveforms in much the same way as during experiments. In order to give simulated τV curves, the problem is set at a fixed pulse width and run repeatedly with gradually increasing voltage. The threshold for latch is recorded as a voltage midway between the highest voltage without latch and the lowest voltage with latch. Error bars are included

which fill this span and depend on the voltage steps examined. This process is then repeated for different pulse durations, in much the same fashion as during experimental latching.

6.2.1 Defect annihilation: D-C

To begin, the D-C latch was tested. The problem was initialised using the static D state director profile as shown in Figure 6.2 and three successive electrical potential profiles were applied. This consisted of a positive pulse of length τ and amplitude V, followed by a second pulse of the same duration τ and opposite polarity $-V$. The final 'pulse' is of 0 V for the duration required for the system to relax. This varies by problem type, but for D-C latch this was typically on the order of τ. The final frame of the simulation can be used to determine the latch state by inspection, or else the latching process can be examined. If the defects from the initial state are seen to annihilate during the simulation then the device has latched and the final state will be continuous.
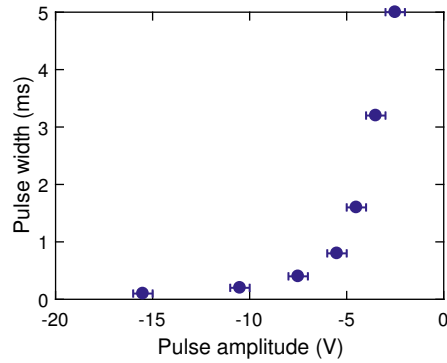
Figure 6.3: Plot of the threshold impulses required to latch in the modelling from the defect to the continuous state. Error bars of ± 0.5 V are included, representing the span from no latch to latch.

The D-C latching curve for the modelling is presented in Figure 6.3. The D-C pulse, which has a leading positive potential followed by a trailing negative pulse,

74

ending with the field removed, is thought to annihilate the two defects found at the top and bottom of the grating grooves. What we see in the modelling (Figure 6.4) is that the $-\frac{1}{2}$ defect, which sits at the point of highest (positive) curvature on the grating, is pushed into the bulk with the leading positive pulse. During the positive pulse, the $+\frac{1}{2}$ defect moves very little, if at all.
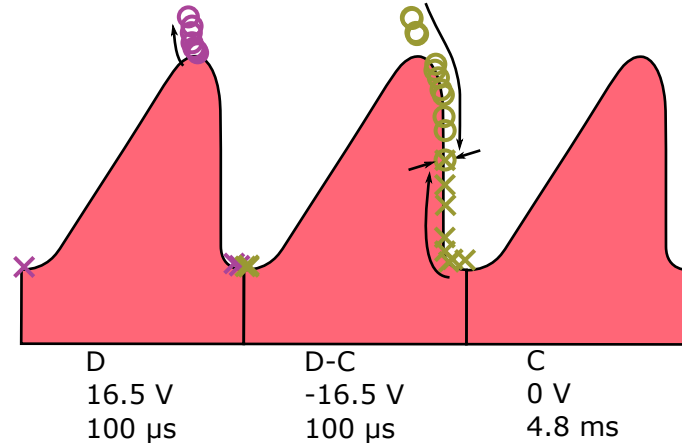
Figure 6.4: Pictoral representation of the movement of defects during latch within the modelling on application of a bipolar (pos/neg) pulse. The $-\frac{1}{2}$ defect is indicated by cirlces, and the $+\frac{1}{2}$ defect by crosses. Movement during the positive pulse is indicated with purple defect symbols, during negative pulse with green, and any movement during relaxation using blue. The instance shown represents the application of a 16.5 V / 100 µs pulse.

During the negative pulse, the $-\frac{1}{2}$ defect returns to the grating surface, and begins to travel down the grating sidewall. The $+\frac{1}{2}$ defect moves from its place at the lowest (negative) curvature and begins travelling up the grating sidewall. Again, distance depends on factors of voltage and pulse duration.

Latching in the DC regime occurs if the defects are close enough together, either during the negative latching pulse or once the field is removed, to annihilate. Otherwise, they return to their positions at the top and bottom of the grating grooves. Once the defects are annihilated and the field removed from the device,

the director field will reorient to adopt the C-state configuration.

6.2.2 Defect nucleation: C-D

Next, the C-D latch was investigated. The initial director profile was set to that of the continuous state as seen in Figure 6.2. In the C-D latch, the pulse used consists of a negative pulse followed by a positive, the opposite to that of D-C. The relaxation time for C-D is much longer than in D-C, typically $> 2\tau$. This is due to the time scale associated with the defects adopting their D-state positions after the pulse is removed.
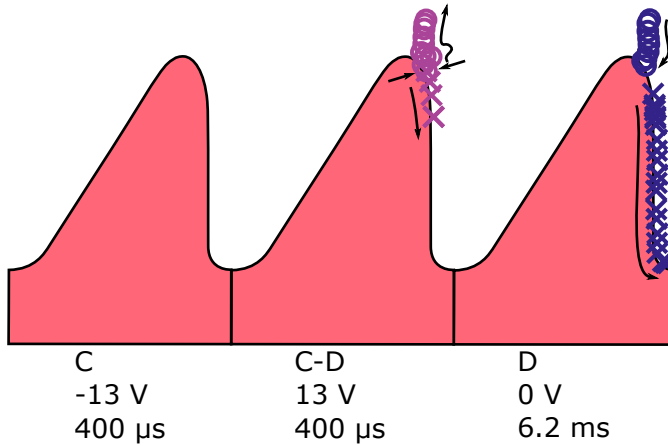
Figure 6.5: Pictoral representation of the movement of defects during latch within the modelling on application of a bipolar (neg/pos) pulse. The $-\frac{1}{2}$ defect is indicated by cirlces, and the $+\frac{1}{2}$ defect by crosses. Movement during the positive pulse is indicated with purple defect symbols, during negative pulse with green, and any movement during relaxation using blue. The instance shown represents the application of a 13 V / 400 µs pulse.

Latching progresses as expected with pulses shorter than 1 ms, summarised in Figure 6.5. Here, we see the leading negative pulse reorient the director field. The trailing positive pulse sees the creation of two defects on the steeper sidewall. Much like in DC latching, the positive pulse draws the $-\frac{1}{2}$ defect off the grating

surface and into the bulk. The $+\frac{1}{2}$ defect moves very little. Once the pulse is removed, the $-\frac{1}{2}$ defect will return to the grating surface and the $+\frac{1}{2}$ defect will begin to travel down the sidewall. If the device latches, neither will interact with the other and will instead adopt their D state positions at the top and bottom of the grooves. However, if the $-\frac{1}{2}$ defect returns quickly to the grating surface, i.e. at lower voltages when it does not go far into the bulk, it will be close enough to the $+\frac{1}{2}$ defect on its return to annihilate with it.
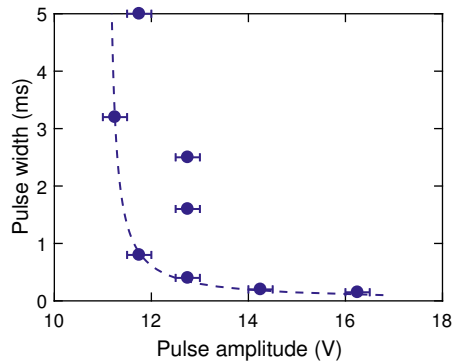
Figure 6.6: Plot of the threshold latch impulses found in modelling to latch from continuous to defect state. Error bars of ± 0.25 V are included. A reciprocal fit calculated from data points at 3.2 ms and below 1 ms is shown. It is of the form $\tau = \frac{(0.6\pm0.1)}{V-(11.07\pm0.04)}$. The scattered points are a result of a separate latch mechanism discussed in the text.

We see the latching curve deviate from the expected reciprocal behaviour at longer pulse widths, requiring higher-than-expected latching voltages (Figure 6.6). Eventually the needed voltages reduce again, before spiking once more, in a cycle as the pulse width increases. Once we examine the defect behaviour within this regime, the cause becomes apparent.

Within the first increased-voltage latch regime, at, for instance, pulses of 1.6 ms, it is the $+\frac{1}{2}$ defect that is found to be responsible for the increase in latching threshold. At sufficiently long pulse widths, the director around the grating is able to distort such that the $+\frac{1}{2}$ defect is pulled from the surface into
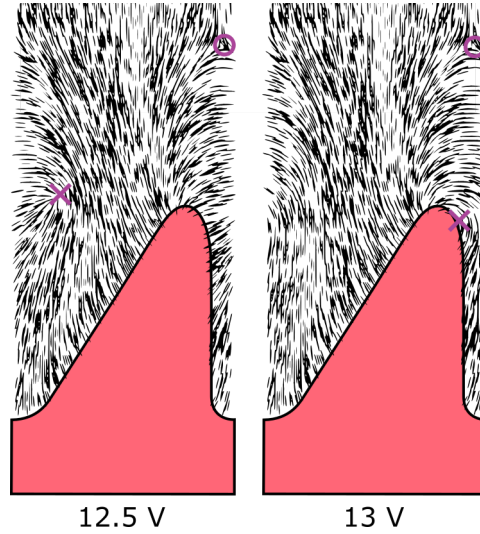
Figure 6.7: Comparison of the final frame during application for CD 1.6 ms pulse. The differing positions of the $+\frac{1}{2}$ defect (marked by an 'X') should be noted.

the bulk, following the $-\frac{1}{2}$ defect. It takes a mostly-horizontal trajectory when travelling, crossing the periodic boundary in x. The latch threshold is increased as these two defects are now able to annihilate in the bulk, in some cases before the positive pulse is removed. Higher voltages prevent the $+\frac{1}{2}$ defect from leaving the surface, and we see the threshold pushed to higher voltages (Figure 6.7).

We see the latch threshold reduce again with the 3.2 ms pulse. In this case, the trailing pulse is long enough that the two defects are far into the bulk and their contributions are no longer significant to the director distortion around the grating. A second defect pair is able to nucleate at the site on the steep grating sidewall. As for short pulse widths, these defects are now the 'latch pair' and, depending on the pulse duration and amplitude (how far the negative defect travels into the bulk), may cause the device to latch. The first pair will annihilate each other in the bulk. This process, an initial pair of defects travelling into the bulk and suppressing latch until another pair nucleate to become the latch pair, may presumably continue as the latching pulses increase ad infinitum, with the device latching with first, second, third etc. generation defects. However, pulse widths above 5 ms require significantly increased simulation time and so were

Figure 6.8: Experimental τV curve for 5CB in a strong anchoring cell held at 30 °C.

prohibitive. At most, the third generation of defects were found.

This long-pulse latching regime of higher and lower voltages has been found experimentally. One such result is shown in Figure 6.8. It was first seen in 5CB, and while the pulse widths are not exactly the same, and could not be explained with current theory from literature. However, combined with the defect dynamics we have seen in the modelling here, we conclude that the experimental behaviour follows the modelling.

6.3 Defect dynamics from experimental observations

We previously stated that at the level of optical microscopy, defect dynamics cannot be determined experimentally in the case of ZBD. At best, observations can successfully distinguish the latched state of each section of grating individually. These grating sections are defined by a single pitch of the grating bounded by the slips on either side. The speed and scale of the latching dynamics are still prohibitive of meaningful observation experimentally; however, macroscopic observations of the static behaviour still informs the overall defect dynamics.

For the purpose of studying defect loop behaviour, it is possible to observe the behaviour of the 'partial latch.' Due to minute variations across a cell, such as in cell gap or discrepancies in the grating replication, the entire active area of a ZBD will not latch at once. Between latch onset and full latch, grating sections will be latched to either state side by side, in different proportions depending on voltage. This introduces a hysteresis to the latch; the energy input required to latch a cell from 50 % D state to 100 % is lower than from full C. It is in exploring this hysteresis that we observe behaviours ascribable to the defect behaviour at the macroscopic scale.

Broadly, we observe two different partial-latch regimes in continuous-to-defect latching when applying successively higher-voltage pulses without blanking back to C in between. In the first, regions of D state are seen to transition in 'epitaxially' - that is, individual grating sections latch or remain C, and increasing the voltage merely increases the density of latched sections until the area is covered. This happens quickly at first, but the last few unlatched regions persist. This mode is seen particularly for pulses longer than 0.5 ms. In the second regime, latch regions at increasing voltages grow as islands of D state, typically beginning at spacer beads or other defects. The islands initially grow along a single slip, and then outward. To begin with, island growth is slow, but after a critical density completion is swift. Shorter pulses display this regime. Both regimes are presented diagramatically in Figure 6.9.

Following this observation, quantisation was considered. Since the two latch states correspond to VAN/HAN cell configurations, we can distinguish between them using their capacitance. We hypothesise that different partial latch regimes will show different progressions in capacitance between the values for either total latch.

A cell of intermediate anchoring strength filled with MLC6204-000 was addressed using bipolar pulses at five different pulse durations while held at 30 ℃. For each pulse duration, the onset and total latch values were found. From the

(a)

(b)

(c)
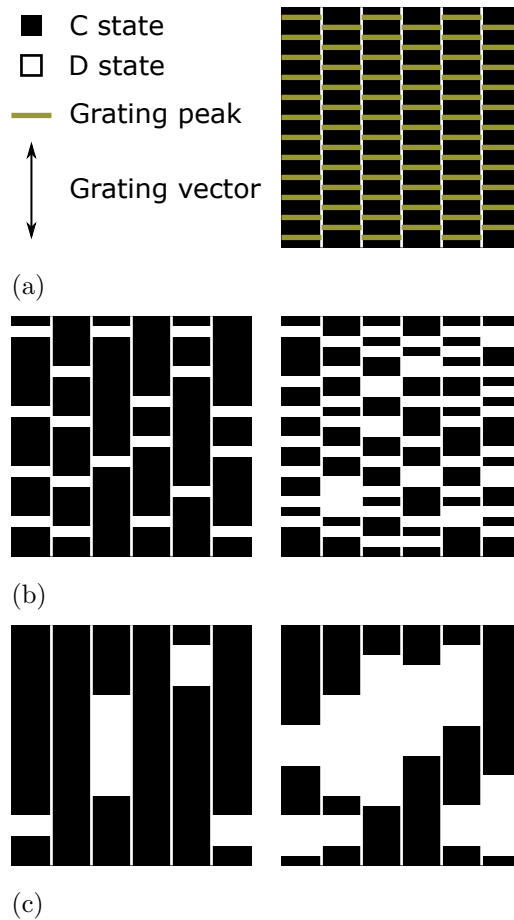
Figure 6.9: Diagrams of POM views of partial latch in ZBD (C to D). (a) gives a schematic of the slips and grating grooves represented in (b) and (c), as well as a legend with C state being black, D state white, and the grating vector oriented north-south in the plane of the page. (b) gives the observed 'eptixial' partial latch, at onset and progression. As the latch progresses from left image to right, sparse latched D regions increase in density over the pictured region. (c) shows 'island growth' partial latching. As the latch progresses from left image to right, lines of D state which have already latch expand, both up/downwards and outward. The ratio of D to C state regions in the final picture for each regime is the same.
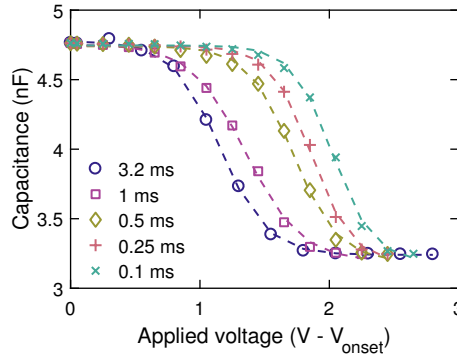
Figure 6.10: Plot of capacitance in nF versus applied voltage (rescaled to account for different onset latch thresholds). The data are fit with logistic curves.

C state, and in steps of 0.2 V until total latch, the capacitance of the cell was measured. This was done using a dielectric bridge (Wayne Kerr 6430A) upon removal of the latch pulse, using a low AC probe voltage: 0.05 V at 1 kHz. The probe voltage is much too low to affect the latch state of the cell or even switch the liquid crystal. The capacitance of the cell was seen to increase logistically, and was fit accordingly (Figure 6.10). The fit follows the equation:

$$Cap = \frac{k_1}{1 + \exp(-k_2(V - k_3))} + k_4 \qquad (6.1)$$

where k_4 is the minimum capacitance (that of the D-state, HAN), $k_1 + k_4$ is the maximum capacitance (that of the C-state, VAN), k_2 is the 'steepness' of the curve, and k_3 is the sigmoid's midpoint, representing 50 % latch. When the fitting values were compared across the variable space, each was found to be approximately invariant to pulse duration except for the midpoint k_3. It was found to decrease with increasing pulse duration (Figure 6.11). This corresponds to the observations of the relative 'speeds' of the two regimes.

The transitions also appear smooth from the data. By comparing to POM images, we see that instead of a regime change at 0.5 ms as originally thought, the two latching behaviours actually coexist and the transition between them is continuous. Pulses of different durations favour each of the regimes in changing proportion but both coexist in each case. This can be seen in Figure 6.12, where
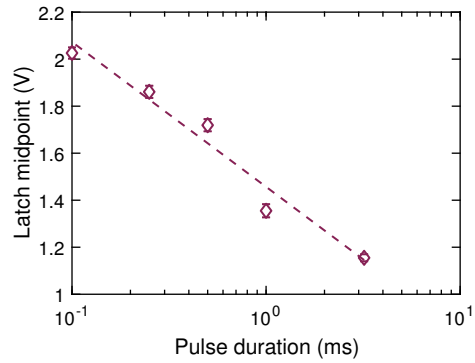
Figure 6.11: Plot of capacitance fit midpoint (from Equation 6.1) versus pulse duration in milliseconds. Included is a fit of the form $c = (-0.62 \pm 0.08) \log \tau + (1.46 \pm 0.05)$
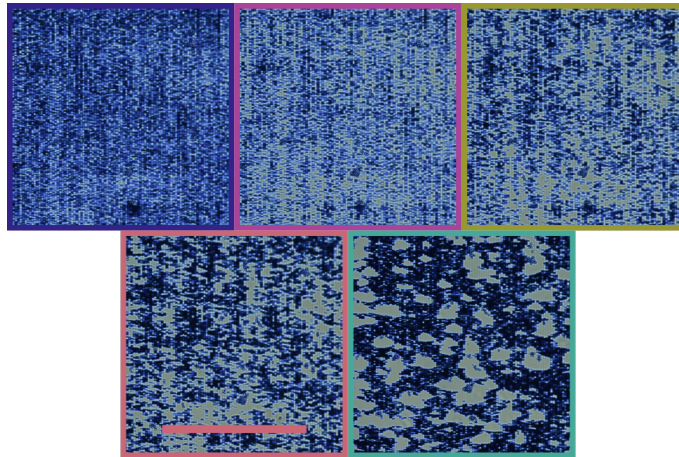
Figure 6.12: POM images of the latch midpoint for the five measured pulse durations. Image borders correspond to the legend from Fig 6.10; from left to right, top to bottom: 3.2 ms, 1 ms, 0.5 ms, 0.25 ms, and 0.1 ms. The scale bar included on the fourth image represents 0.5 mm.

POM images were taken at the midpoint of each partial latch. These correspond to approximately equal capacitances (indicating equal split of C and D states) but are optically distinct, showing unique mixes of single-grating latch and island growth.

Underlying these observations is the conclusion that the defect dynamics involved in the C-D latch are strongly dependent upon the pulse duration. This behaviour happens in three dimensions and involves the grating slips. Overall we conclude that for shorter pulse durations, it is energetically favourable for a C-state region near to D-state to latch to D. To state the reverse, for longer pulse durations any one grating section, regardless of neighbours, has an equivalent latch energy.

To relate this to the modelling, we see in the C-D results (Figure 6.7) that longer pulse widths introduce more complicated defect dynamics, including migration of defects between grating sections (seen in modelling as the defect crossing a periodic boundary to appear on the opposite side). In a partially latched state, these defect movements could work to suppress latch in neighbouring grating sections leading to a random distribution of latched sections across the cell.

The shorter pulse durations seem to indicate that the presence of other defect loops nearby favours a latch at a particular grating section. It's currently unknown how the defect loops behave across multiple pitches and slip boundaries; does each individual grating section have its own loop, or is there a single outer loop encompassing the islands as we see them? Does a grating section next to one of these loops represent the expansion of the outer loop, or the creation of a new loop? A new model simulation representing multiple pitches and slip boundaries is necessary to explore the 3-D behaviour in this case.

6.4 Non-flexoelectric latching

A third latching regime exists in ZBD experimentally. Rather than applying single bipolar pulses, the D state can latch to C after application of an RMS field (Figure 6.13). Below the RMS latch, the LC is switched accordingly with its dielectric anisotropy as would happen in a regular cell, relaxing to its original state once the field is removed. Above a threshold, the bright state is not retained on removal and instead the cell remains 'switched,' i.e. latched. Unlike the bipolar

(a)   (b)
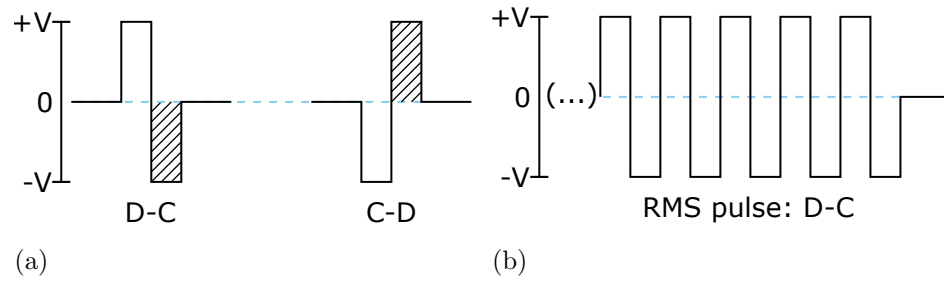
Figure 6.13: Schematics of (a) bipolar latching pulses and (b) RMS latching pulse. Where the bipolar pulses latch between states according to the trailing pulse (highlighted), the RMS pulse will only latch D-C.

latching, this is not a polar response and cannot latch in both directions. As such, it is assumed to be the result of dielectric rather than flexoelectric properties.
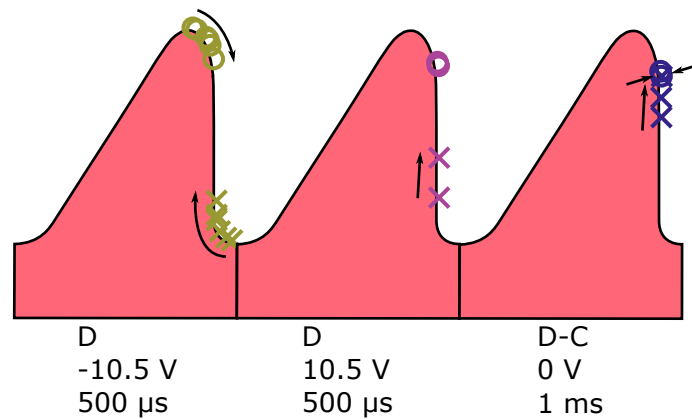
Figure 6.14: Schematic diagram of defect movement in 'RMS' latching from the modelling, where the flexoelectric terms are removed from the simulation. The polarity of the pulses as applied are included; since the flexoelectric terms have been removed, these do not affect the movement of the defects. The $-\frac{1}{2}$ defect is indicated by cirlces, and the $+\frac{1}{2}$ defect by crosses. Movement during the positive pulse is indicated with purple defect symbols, during negative pulse with green, and any movement during relaxation using blue.

Experimentally, this latching can be investigated easily by applying an RMS

pulse using a function generator. However, the simulation times required to apply significant numbers of pulses to indicate an RMS field were prohibitive. Instead, so called 'RMS latching' was simulated by removing the flexoelectric coefficients in the problem setup. A single bipolar pulse is applied (as in the other latching tests) and the results are assessed the same way. Without the flexoelectric terms, the $-\frac{1}{2}$ defect never leaves the surface, but the pair are still brought together to annihilate and give C state, should the voltage be sufficiently high (Figure 6.14).
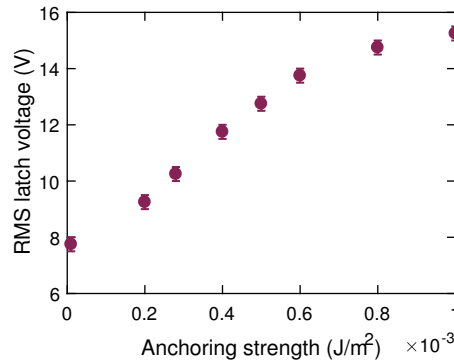
Figure 6.15: Plot of modelled RMS latching voltages against the input anchoring strength. Data points centred around 1×10^{-4} J/m^2 have been omitted, due to the modelling program taking these values as a default for 'strong' anchoring.

In the modelling, we applied a 1 ms bipolar pulse, representing a 1 kHz RMS waveform, varying the voltage as before to find the threshold latch values. Since RMS latching is independent of frequency or pulse width, we instead investigate the effect of varying the anchoring strength. This is something we are also able to investigate experimentally using the photopolymer mixtures for variable anchoring strength. The modelling results are given in Figure 6.15. We see an initial increasing linear trend which saturates towards 16 V$_{RMS}$ as we increase anchoring toward infinite.

A similar trend is found in experiment (Figure 6.16). The photopolymers represent a much narrower range of anchoring strengths than the modelling program can reproduce, but according to our measurements in [41], they represent
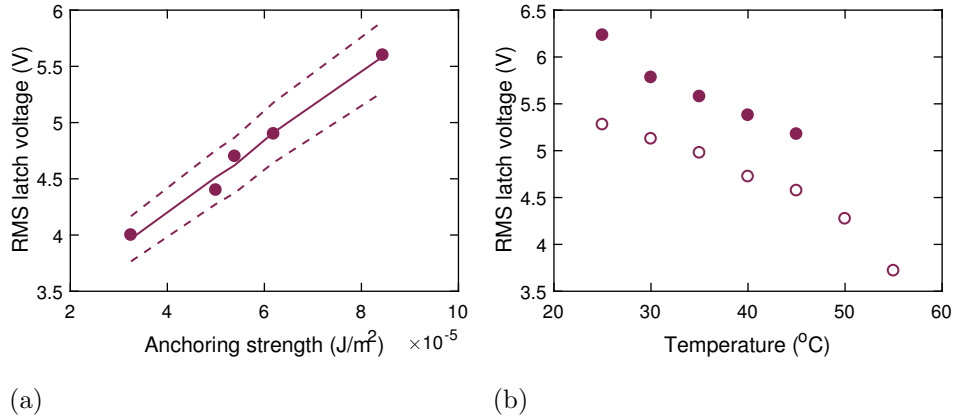
Figure 6.16: Plots of experimental RMS latching voltages against (a) anchoring strength and (b) temperature. In (a), the upper and lower fits represent the total and onset latch values, whereas the data represents the midpoint of the RMS latch. In (b), open circles show the onset of latch, and solid circles show total latch.

	Latch threshold (V)		
	Modelling	Experiment	Difference
C-D latch	11-16	5-10	6
RMS	8+	5+	3

Table 6.2: Comparison of thresholds for modelling and experiments. Experiments refer to those done using MLC6204-000, a close analogue of the model's 'mixture B'. The modelling consistently overestimate latching values.

anchoring strengths up to 1×10^{-4} J/m^2. Our simulations would predict an RMS latch at around 9 V for this anchoring range, overestimating the ~ 5 V value we see in experiment. This might partly be explained by the removal of the flexoelectric terms; even with an oscillating waveform, flexoelectricity is still present in the experimental system. A more significant contribution seems to be the model itself. Even for τV curves, the model consistently overestimates the voltages necessary to latch (Table 6.2). From [1], we know that 'mixture B' which

the model simulates outperforms MLC6204-000 in experiment, so the actual differences are more significant. The values for latching from the model are judged to be inaccurate; however, the behaviours seen are replicated in experiment and so the defect dynamics are accepted.

6.5 Defect speed

The movement of defects under electric field is critical to ZBD operation. From observations of the latching during modelling, we now know that a positive voltage applied below the grating surface forces $-\frac{1}{2}$ defects off the grating surface and into the bulk, whereas negative voltages draw the same defect back towards the grating surface and the $+\frac{1}{2}$ defects up the grating sidewall. This can be conceptualised by considering the defects 'charged,' although reversed to what might be expected with electrical charges. The positive voltage appears to repel the $-\frac{1}{2}$ defect and attract the $+\frac{1}{2}$ (causing it to remain stationary at the surface); the negative voltage seems to attract the $-\frac{1}{2}$ defect and repel the $+\frac{1}{2}$, causing annihilation in D-C latching.

It is also readily observed that the movement of the defects, specifically the distance travelled, is related both to the pulse amplitude and duration. This effect is easiest to track in movement of the $-\frac{1}{2}$ defect from the top of the grating with positive voltage. In ParaView, the ruler feature was used to track the distance travelled. Within the full application of a single pulse, the defects were tracked in steps of 50-200 iterations, rather than directly from start to end. In this way, we account for the non-linear trajectory of the defects.

Data were taken from the latching tests of six pulse durations at a variety of voltages, all positive. By considering defect speed, rather than distance travelled, we are able to account for distance, pulse duration, and voltage at once. Results are given in Figure 6.17. To do this, the distance travelled was divided by the pulse duration in each instance, giving the average speed during travel. When multiple pulse durations are taken together, this gives an approximate linear relationship, given by the equation $speed = (7.8 \pm 0.9) \times 10^{-5}V + (-5 \pm 1) \times 10^{-4}$.
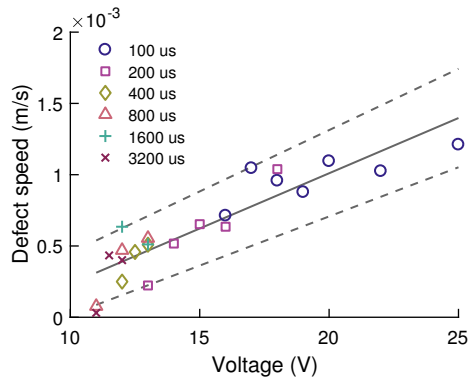
Figure 6.17: Plot of $-\frac{1}{2}$ defect speed in m s^{-1} versus voltage for a number of pulse durations. Three linear fits are included to guide the eye: $speed = (7.8 \pm 0.9) \times 10^{-5}V + (-5 \pm 1) \times 10^{-4}$.

This further lends credence to the effective 'charge' of the defects as mentioned before.

The data given in Figure 6.17 were taken from the latching tests already conducted. After finding this linear relationship, tests were conducted specifically aiming to look at defect speed across a range of voltages, using a constant pulse width of 400 µs. In this way, the large uncertainty in the fit was to be mitigated.
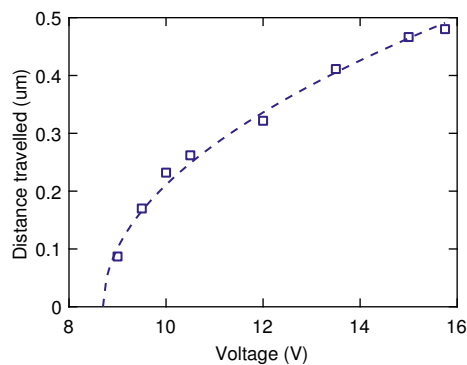
Figure 6.18: Plot of defect distance versus voltage for a 400 µs pulse. A fit of the form $dist = (0.185 \pm 0.009)\sqrt{V - (8.7 \pm 0.2)}$ is included.

89

6. DEFECT DYNAMICS IN BISTABLE LATCHING

To begin, the D state was initialised, and a series of voltages applied in the range 3 - 25 V, all positive with respect to the grating surface. The $+\frac{1}{2}$ defect was tracked as before. Voltages tested below 9 V did not cause the defect to leave the surface. An initial set of data is shown in Figure 6.18. A square root relationship is found up to 15.75 V. Since the pulse applied is constant throughout, this relationship has a direct correlation to defect speed. When evaluated, this reduces to $v = (4.6 \pm 0.2) \times 10^{-4} \sqrt{V - (8.7 \pm 0.2)}$ where v is speed in m/s. Considering electrical potential energy,

$$\frac{1}{2}Mv^2 = q(V - V_o). \tag{6.2}$$

This is including an offset voltage V_o which represents the critical voltage at which the defect will leave the grating surface. We can then compare this to our fit equation by rearranging:

$$v = \sqrt{\frac{2q}{M}}\sqrt{V - V_o}. \tag{6.3}$$

From this analysis we deduce that our offset voltage is 8.7 ± 0.2 V and $\frac{q}{M}$ is $(1.058 \pm 0.002) \times 10^{-7}$ C/kg. The latter value seems un-physical for defects, which as regions of disorder do not inherently carry charge or have mass. Instead, this quantity is hypothesised to be related to viscous inertia and flexoelectric effects.

This first region ties up the physics quite nicely; however, if we increase the voltages applied above the values here, different behaviours emerge.

Above 15.75 V, two further regimes are seen: the first of linear decreasing distance/speed with voltage (16.5 - 21 V), and the second of a plateau (from 21 V) to around 400 nm total travel distance or a speed of 1 mm/s .

Observing the dynamics in the simulations gives the cause of these changes in behaviour. Two factors complicate matters: first, the $+\frac{1}{2}$ defect, and second, further nucleated defect pairs. At pulses significantly higher in amplitude than typical latch values (at 400 µs, the latch voltage is 12.75 V), the $+\frac{1}{2}$ defect does begin to move. As it approaches the other defect, the latter's trajectory is altered
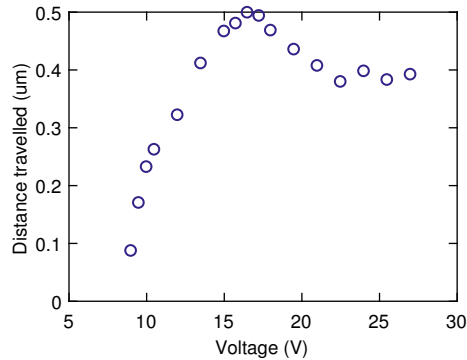
Figure 6.19: Plot of defect distance versus voltage for a 400 µs pulse.

and subsequently its speed is negatively impacted. No longer is the prevalent force pushing it toward the bulk; it now draws back to the grating surface. The defect trajectories for an 18 V pulse are shown in Figure 6.20. In order to quantify this effect, the final defect separation was plotted as a function of applied voltage (Figure 6.21). There are three obvious regimes. In the first, defect separation increases with an approximate square root relationship with applied voltage, up until the critical applied voltage of 15.75 V. A rapid decrease in separation is seen from here to 18 V. From 18 - 19.5 V there is a discontinuity, followed by a second, less extreme decreasing regime. The first regime corresponds to the defect moving farther into the bulk under the applied field; the second involves frustration of the director field and the nucleation of further defect pairs; in the third regime, the director frustration is mostly resolved. The increasing voltage relates to how quickly the $+\frac{1}{2}$ defect moves up the sidewall towards the $-\frac{1}{2}$ defect. This leads to the topological attraction overcoming the electrical effects.

Following the analysis of defect speed and separation, data were gathered for the number of observed defect pairs against voltage. Nucleation and trajectories for the four pairs case at 18 V are shown in Figure 6.20. Pairs seen numbered either one, two, or four. This indicates a regime of little-to-no frustration, a regime of increasing frustration, and a final regime of constant, heightened frustration. The middle regime correlates well with regions of greatest change in the other two plots. The frustration stems from the competition between the increasing

91
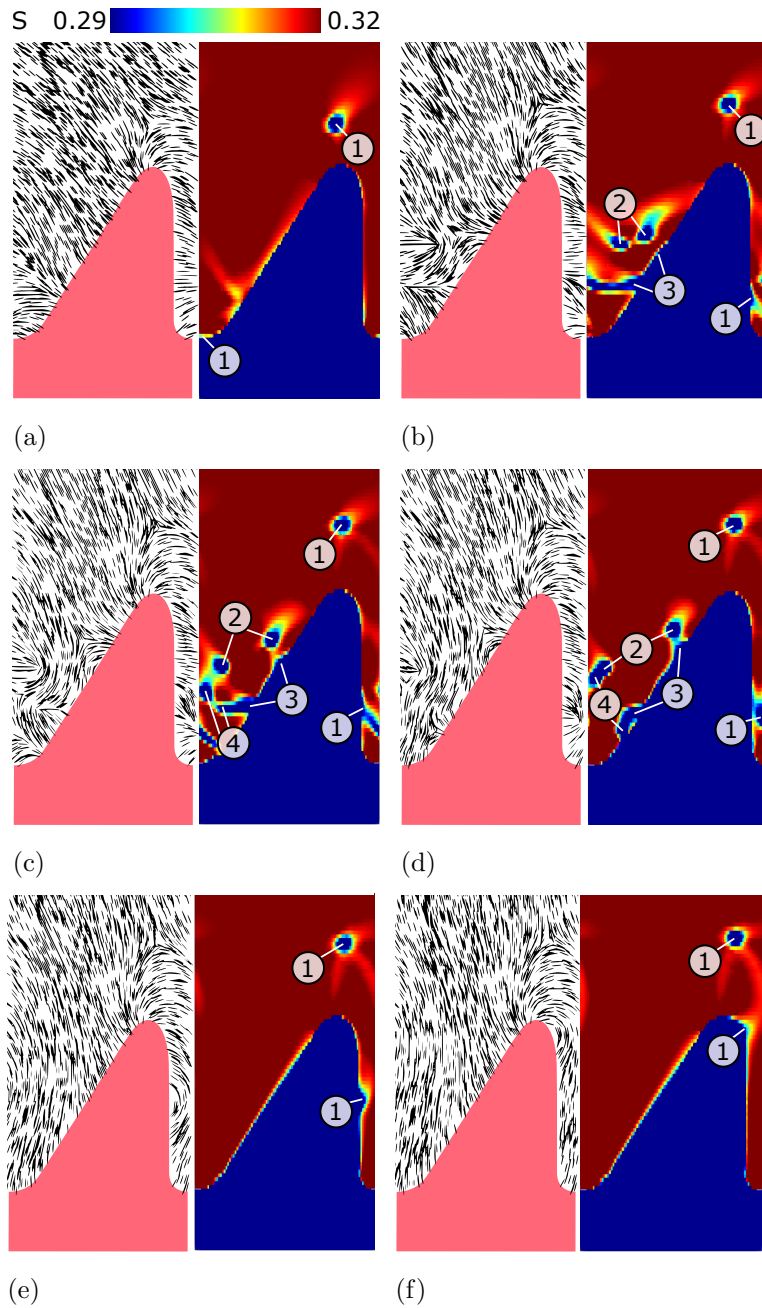
Figure 6.20: (a)-(f) A progression of defect creation and annihilation for +18 V applied for 400 µs. For each instance, the director field and a map of the order parameter is included. The colourmap for the latter is included in the first image (a).
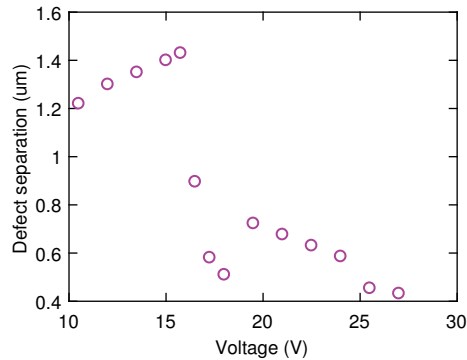
Figure 6.21: Plot of simulation-end defect separation versus voltage for a 400 µs pulse.
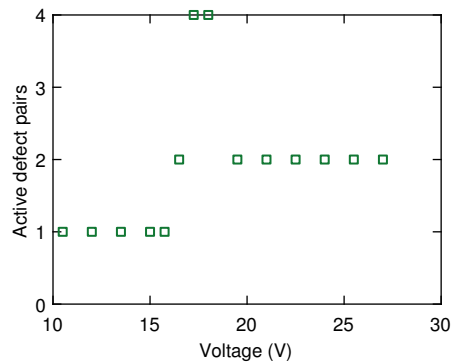
Figure 6.22: Plot of the number of defect pairs against voltage for the modelled system.

electrical reorientation force and the elastic contributions of the anchoring for the D-state.

By lining up the three datasets considered, of defect speed, separation, and number of active defect pairs (Figure 6.23), we can settle on two regime boundaries, at 15.75 V and between 18 and 19.5 V. The first regime boundary represents the limit for the linear speed behaviour we noted previously. Crossing from the first regime into the second is a continuous shift for distance/speed and defect separation. From the modelling, this boundary appears to correspond to the limit after which the electrical reorientation begins to overcome the elastic align-

93
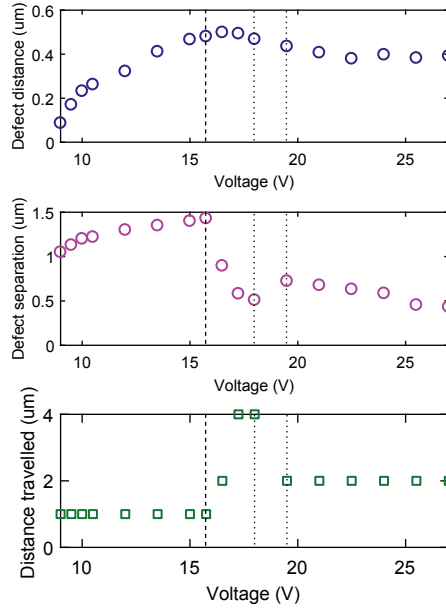
Figure 6.23: Plot of defect behaviours stacks so as to highlight correlations. The most prevalent regime boundaries are indicated with dotted lines.

ment. This leads to the $+\frac{1}{2}$ defect approaching the $-\frac{1}{2}$ defect, decelerating it and significantly reducing defect separation. At sufficiently high fields, the electrical reorientation was able to overcome the elastic without nucleating multiple new defects. The second regime boundary indicates this, and represents a discontinuous shift for the defect separation. They are further apart at the beginning of the third regime, and grow closer again, but slower, with increasing voltage.

At these higher voltages, what we are seeing is the annihilation of the D state defects under application of a positive pulse. This means we are seeing a latch from D to C state, without using a negative pulse. In experiment, at voltages sufficiently higher than the C-D latch, a positive pulse will reverse-latch D-C. Data for the reverse latch has previously been presented in literature [1], Figure 6.24; the onset of reverse latching marks the upper limit for operating voltages in devices. While the multiple newly-nucleated defect pairs may not be physical, and might in fact be artefacts of the modelling, there is sufficient evidence to suggest that the competition between the electric and elastic forces causing movement of

94
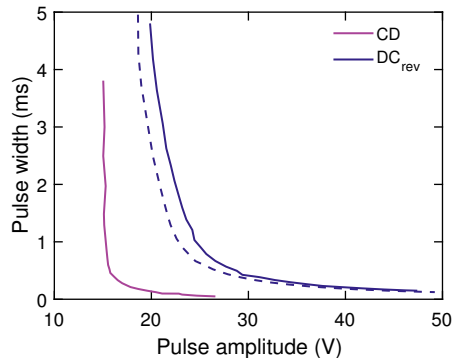
Figure 6.24: τV data for MLC6204-000 in a 3.6 µm cell including reverse latch. The dashed line shows the onset of reverse latching, and the solid line the full reverse latch. Data were taken from [1].

the $+\frac{1}{2}$ defect towards the negative at high voltages is what causes or contributes to the reverse latching. Ionic effects were previously indicated to be the sole source.

Critical fields V/d (V/m)			
[1], MLC6204-000		Modelling, Mixture B	
Reverse onset	3.99×10^6	First regime change	3.15×10^6
Reverse total	4.23×10^6	Second regime change	$(3.75 \pm 0.15) \times 10^6$

Table 6.3: Table of critical field values, comparing the 3.6 µm MLC6204-000 cell from experiment [1] and the 5.0 µm cell from modelling at 400 µs pulse width.

In order to further verify this hypothesis, we compare the fields for the reverse latch from experiment and modelling. The two samples are of different cell gaps and material so comparing the fields allows us to account partially for the differences. Experimental reverse latch data is taken from MLC6204-000 in a 3.6 µm cell; the modelling data is from a 5 µm cell of mixture B, as previously discussed. Our critical points for comparison are the onset of reverse latching and the completion in the experiment (Figure 6.24), and from the modelling, the

95

15.75 V regime shift and the regime shift which occurs between 18 and 19.5 V. The field values are listed in Table 6.3. Between modelling and experiment, each are comparable, and lend credence to the conclusion that these regime changes, and the movement of the defects, contribute to the reverse latching seen in experiment. Most significantly, the second regime change overlaps with the critical field for the onset of reverse latching. This indicates that once the electrical forces overcome the elastic within the grating grooves, we will see reverse latching in the device.

6.6   Conclusion

Defect dynamics in ZBD were explored in four parts, and new latch modes were presented in detail: the suppressed C-D latch, the partial latch, RMS latch, and the reverse latch. These are modes which are found experimentally but rarely focused on in literature. Through both modelling and experiment, we were able to observe the defect dynamics in latching between states in each of these modes. QLC3D was found to model behaviour of the device well, but without access to the material modelled, the precision of the model numerically is as yet undetermined. Explanations were found for phenomena previously observed but thus far unattributed.

Chapter 7

Improved performance through designer LCs

Critical to the performance of the ZBD is flexoelectric latching. Following the latching theory, operation of the device at lower voltages may be achieved through increasing the flexoelectric sum, $(e_1 + e_3)$. This is a quantity which is not trivial to measure [65, 66, 67, 68]; however, following the physical principles behind flexoelectricity, we can target materials whose properties should lend to increased flexoelectric polarisation.
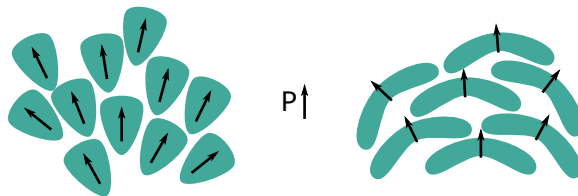
Figure 7.1: A schematic of how nematic packing of pear- and banana-shaped molecules can lead to flexoelectric polarisation. Reproduced from Chapter 2.

Cylindrical symmetry is a useful skeleton model for calamitic LCs. However, no molecule has perfect cyclindrical symmetry. Molecular symmetries which are more inherently bent or wedged can give rise to macroscopic physical effects when a sample is elastically distorted. Thus, small flexoelectric polarisations arise from

molecular shape. As discussed previously in Chapter 5, large splay and bend flexoelectric polarisations are present in materials whose molecules pack in a particularly splay or bent way, such as pear- and banana-shaped molecules (Figure 7.1). Local flexoelectric polarisation can also be induced by distortions in the director field, such as around included structures. Bent-core liquid crystals most immediately fit the 'banana-shape' ideal for flexoelectric polarisation. Indeed, relatively strong flexoelectric effects have been measured in these materials [68, 69, 70]. Liquid crystal dimers, a sort of structural inversion of bent-core liquid crystals, are a branch of molecules currently investigated for their exhibition of the twist-bend nematic phase N_{tb}. This phase is present when the connecting chain, a flexible carbon chain connecting two rod-like end groups, is made up of an odd number of carbons. This gives the overall dimer the desired bent shape. These materials have been indicated alongside bent-core LCs as having large flexoelectric properties [71, 72, 73].

In this thesis we investigate the effect of the addition of several odd dimers into the display mixture MLC6204-000 for use in ZBD. By determining the latching curves, we were able to examine how they affect the display performance, and to an extent determined by our knowledge of other device parameters, indirectly measure the flexoelectric sum of the mixtures.

7.1 The materials

Four dimers constituted the primary investigation. Their chemical structures are given in Figure 7.2. CB7CB and CB9CB are well known as exhibitors of the N_{tb} phase and literature regarding them is well established and expanding [74, 75, 76, 77, 73]. They are structurally homologous, consisting of two cyano-biphenyl groups attached by a 7- or 9-carbon chain respectively. Two more dimers, built upon the structures of the first two, were also investigated. RM1704 has a 9-carbon chain as in CB9CB, but it is both shortened and stiffened by two triple bonds at either end of the carbon chain. The final material, RM1914, also has a 9-carbon chain, with included fluorine groups alongside the

(a)

(b)

(c)

(d)
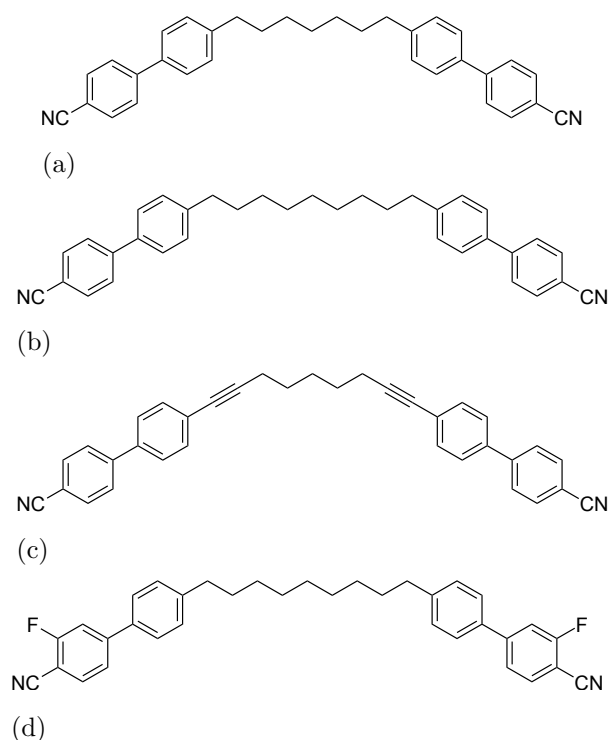
Figure 7.2: Chemical structures for the dimers (a) CB7CB, (b) CB9CB, (c) RM1704, and (d) RM1914.

cyano groups. These were added to target an improved $\Delta\epsilon$ in order to make a more display-friendly material.

The materials in question were synthesised at the University of York by Richard Mandle.

7.2 Dimers as dopants in ZBD

Each dimer was added at 10 % by weight into MLC6204. Additionally, the effect of concentration was measured on CB9CB and RM1914 up to concentrations of 15 % by weight. This was found to approach the solubility limit for these compounds in the mixture. Phase transitions were found for each mixture and are

	Concentration (%wt)			
	5	10	15	100
MLC6204				64
CB7CB		65		117
CB9CB	65	64	67	122
RM1914	62	62	63	66
RM1704		64		n/a

Table 7.1: Table of T_{NI} for the mixtures and compounds as measured on cooling. The final dimer RM1704 does not exhibit a nematic phase in its pure form.

presented in Table 7.1. τV curves were then taken for each mixture composition.

	Concentration (%wt)			
	0	5	10	15
MLC6204	0.5			
CB7CB			1.0*	
CB9CB		0.75	2.0*	2.0*
RM1914		0.5	1.0	2.0*
RM1704			1.0*	

Table 7.2: Table of shortest pulse duration in ms which results in a full C-state latch for the different dimer mixtures. Asterisks mark cells of higher anchoring.

Experiments began using cells of approximately 2 µm cell gap and intermediate anchoring ($(5.4 \pm 0.8) \times 10^{-5}$ J m^{-2}). During electrical testing the cells were held at a constant 30 °C. This represents $T = 0.9T_{NI}$ for MLC6204-000, and due to the minimal changes (< 1 %) to T_{NI} among the mixtures (Table 7.1) the reduced temperature remains approximately constant. The addition of the dimers was seen to affect the formation of the C state to some extent at this anchoring strength. Namely, using D-C pulses the cells struggle to achieve C state at shorter

pulse widths (0.5 ms and lower). This worsened at higher concentrations, until the C state was no longer fully stable. Regions of C state could be latched but these never covered the full observation area. The shortest pulse widths in ms able to latch fully to C state for each mixture are presented in Table 7.2. Some cells used would only latch to C state using pulses of at least 2 ms; not shown is the intermediate-anchoring 10 %wt CB9CB cell which did not give a full C state latch at any pulse width. To counteract this instability, higher anchoring cells were used for certain mixtures ($(6.2 \pm 0.9) \times 10^{-5}$ J m^{-2}) - these are indicated using asterisks (*) in the table. In τV curves, these higher anchoring cells are indicated with triangular markers, in contrast with circular markers for the intermediate anchoring cells. The higher anchoring leads to overall higher latching thresholds; we'll take steps to account for this difference later on.

7.2.1   Latching data
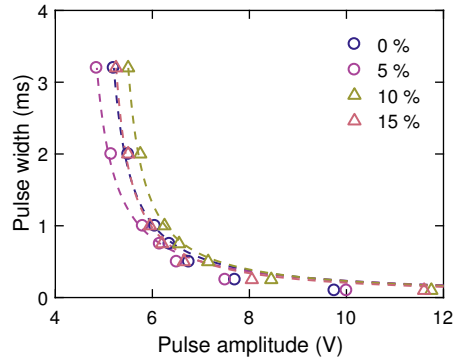
Figure 7.3: τV data as taken for different % wt mixtures of CB9CB in MLC6204. Stronger anchoring cells are represented with triangular markers. Included are the fits of the reciprocal form $\tau = \frac{A}{V-B}$.

Figure 7.3 shows the effect of increasing concentration on the latching thresholds for CB9CB/MLC6204 mixtures. Included is the latching curve for pure MLC6204, indicated as the 0 %wt mixture. The thresholds decrease at longer pulse widths from 0 to 5 %wt, and from 10 to 15 %wt. The decreases are not

dramatic, but neither are the concentrations significantly large. From 5 to 10 % we see an expected increase alongside the switch to higher anchoring cells. We can offset this increase by the measured anchoring strengths (see Chapter 5) and also control for the variations in cell gap. After dividing through by both anchoring strength (J m^{-2}) and cell gap (m), our new x-axis has units of m C^{-1}.
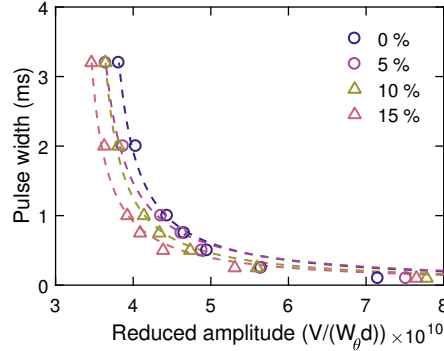
Figure 7.4: τV data as taken for different % wt mixtures of CB9CB in MLC6204, adjusted for differences in cell gap and anchoring strength. Stronger anchoring cells are represented with triangular markers. Included are the fits of the reciprocal form $\tau = \frac{A}{V-B}$.

Figure 7.4 shows the data after adjusting for these factors. The adjusted data show a consistent decrease in threshold voltage across increasing concentration, although the steps are small. From 5 to 10 %wt the thresholds are almost indiscriminate, except at pulse widths below 1 ms, where the 10 % slightly outperforms the 5 % sample.

Figure 7.5 gives the raw and adjusted data for RM1914, the fluorinated dimer. Once more we see a decrease in threshold values for increasing concentration of the dimer in MLC6204. From 10 to 15 % the effect seems to saturate as the values are equivalent after adjusting for anchoring strength and cell gap.

Figure 7.6 compares the four dimers' effects on threshold values at 10 %wt. CB7CB and RM1704 appear to be equivalent at this concentration. CB9CB

(a)   (b)
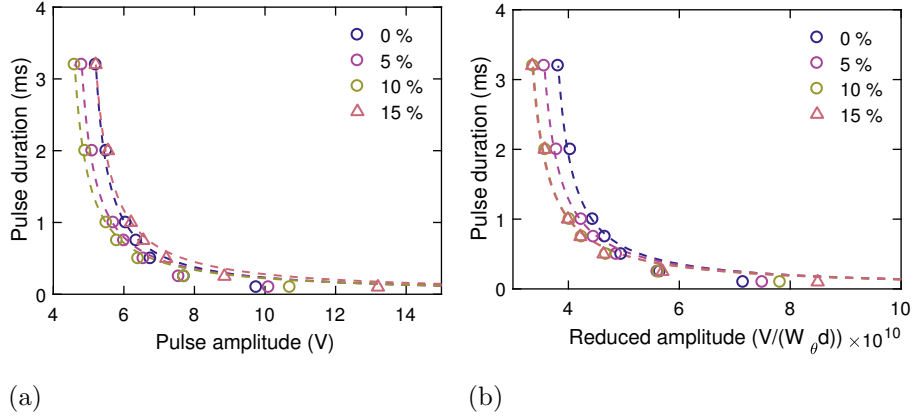
Figure 7.5: (a) raw and (b) adjusted τV data for RM1914 mixtures in MLC6204. Stronger anchoring cells are represented with triangular markers. Included are the fits of the reciprocal form $\tau = \frac{A}{V-B}$.

(a)   (b)
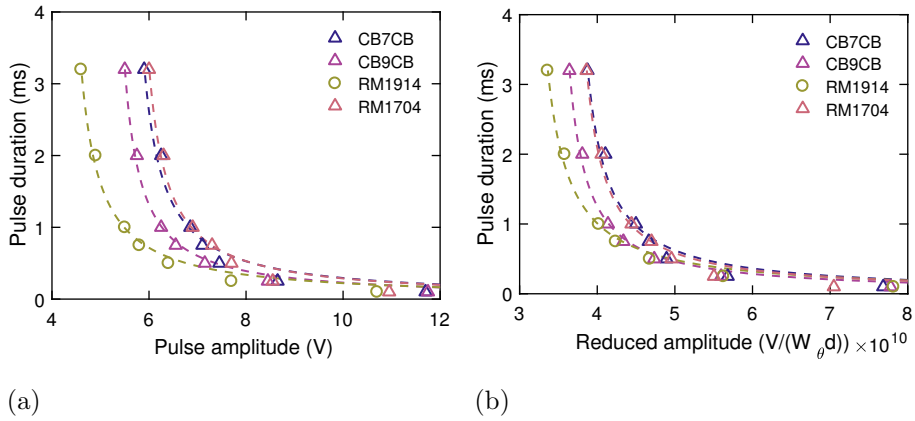
Figure 7.6: (a) raw and (b) adjusted τV data for each dimer mixture at 10 % by weight in MLC6204. Stronger anchoring cells are represented with triangular markers. Included are the fits of the reciprocal form $\tau = \frac{A}{V-B}$.

gives lower thresholds to both, and RM1914 has the lowest threshold overall. The trends are essentially the same before adjusting for anchoring strength and cell gap, but become less pronounced after the adjustment.

At this stage of analysis, we see a general benefit to the threshold voltage for addition of each dimer. At 10 %, RM1914 has the most pronounced effect at

lowering the threshold voltage.

7.2.2 Fitting parameter analysis

Each of the τV curves were fitted to the reciprocal form as in previous chapters, following the equations from Davidson and Mottram [13] and Spencer *et al.* [40]. This gives us two parameters, the shape factor:

$$A = \frac{\gamma_1 l_s d}{(e_1 + e_3)}, \tag{7.1}$$

and the threshold voltage:

$$B = V_{th} = \frac{2W_\theta d}{(e_1 + e_3) + \sqrt{\epsilon_o \Delta \epsilon K_{33}}}. \tag{7.2}$$

The cell gaps were measured in each instance, and the liquid slip and anchoring strengths are known from the work presented in Chapter 5 [41]. After accounting for these known quantities, we are able to compare a value for each parameter which more closely resembles the flexoelectric sum. For A (Eq 7.1), we look at $A/(l_s d)$ or $\gamma_1/(e_1 + e_3)$ (kg C^{-1} s^{-1}). We'll refer to this going forward as the visco-flexoelectric term. For V_{th} (Eq 7.2), we look at $V_{th}/(W_\theta d)$, or $2/((e_1 + e_3) + \sqrt{\epsilon_o \Delta \epsilon K_{33}})$ (m C^{-1}). This will be referred to as the reduced threshold. Combining the relative uncertainties from the fitting itself for the threshold (up to 2 %) and for the other factor (up to 10 %), the experimental errors from measuring the cell gap (3-5 %), we get an uncertainty in our reduced values in A of 15 % and in V_{th} of 5 %. With these in mind, we compare among our data.

Both terms for both dimers are seen to decrease with increasing concentration of the dimer. Figure 7.7(a) indicates that improvements in the visco-flexoelectric term are greater in CB9CB than in RM1914. This may be attributed to either the viscosity or the flexoelectric sum. The reduced threshold value is dependent on the flexoelectric sum, dielectric anisotropy, and bend elastic constant. Reduction in this value would follow from an increase in these values, however we expect the bend elastic constant to be reduced. This is supported by work in the literature
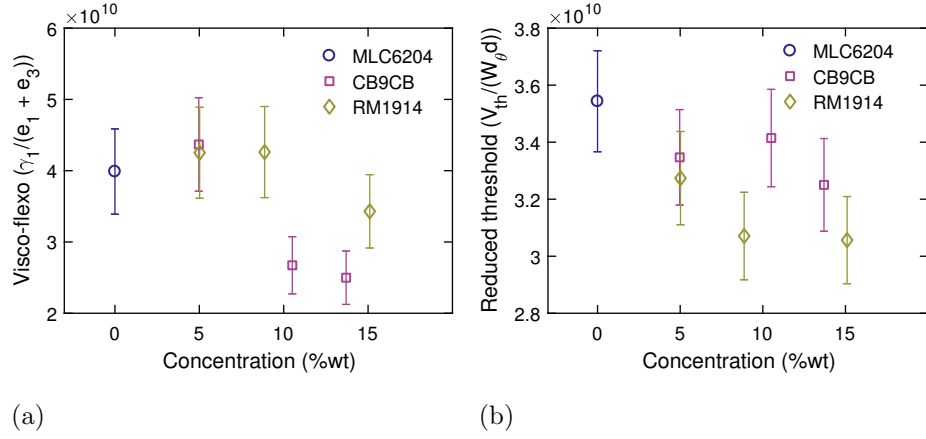
Figure 7.7: (a) reduced shape factor and (b) reduced threshold voltage by concentration for CB9CB and RM1914. Included at 0 % are the fitted values for MLC6204.

on bent-core materials added to calamitic nematics: these mixtures at 10 %wt typically measured as 60 % of the value for the calamitic alone [78, 79, 80]. Literature on odd dimers also predicts low bend elastic constants, which would in turn lower those as found in mixtures [72]. This reduced threshold is improved slightly with the addition of both dimers, each to a similar degree within error. If we assume the dielectric anisotropy to be dominated by the host mixture and therefore comparable within each mixture, this small reduction suggests a larger increase in the flexoelectric sum, due to the expected reduction in K_{33}. A low confidence linear fit may be performed for each dimer for each parameter in order to extrapolate to 100 %wt. The values from this extrapolation are presented in Table 7.3. Due to the associated errors and the limited points available to the fits,

Dimer	$\frac{\gamma_1}{(e_{11}+e_{33})}$ (kg C^{-1} s^{-1})	$\frac{V_{th}}{W_\theta d}$ (m C^{-1})
CB9CB	$(-9 \pm 6) \times 10^{10}$	$(1.8 \pm 0.9) \times 10^{10}$
RM1914	$(1 \pm 4) \times 10^{10}$	$(0 \pm 1) \times 10^{10}$

Table 7.3: Table of 100 %wt extrapolations for dimers CB9CB and RM1914.

this extrapolation is not well regarded but may offer at least order of magnitude

confidence for the values.
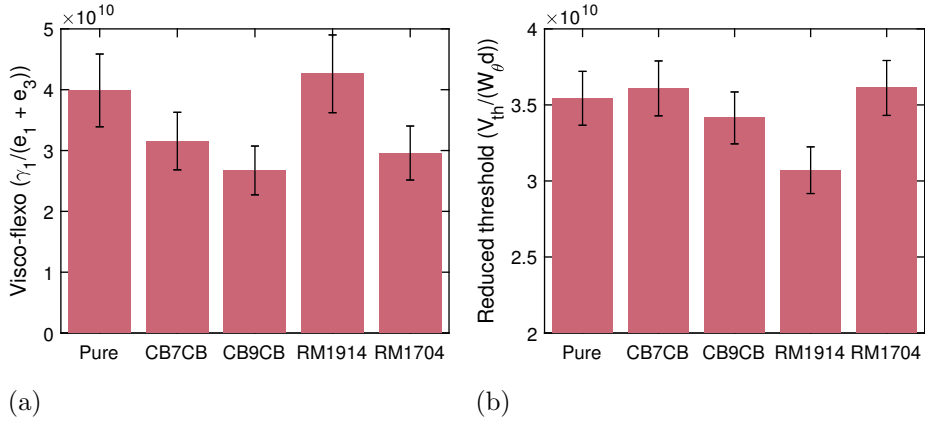
Figure 7.8: (a) reduced shape factor and (b) reduced threshold voltage for the 10 % mixtures of each dimer and for the pure MLC6204.

At 10 %wt concentrations (Figure 7.8(a)), RM1914 offers no improvement to the visco-flexoelectric value, which we saw previously. Each other dimer reduces this value slightly, and are within error equivalent to each other. In Figure 7.8(b), we see that the reductions found in most dimer's threshold voltages (Figure 7.6) disappear within error after accounting for anchoring strength and cell gap. The only exception to this could be the fluorinated dimer RM1914. This mixture shows a small reduction in comparison to the others, however still constant to within two standard deviations. This reduced threshold voltage depends on three values (Eq 7.2): the flexoelectric sum, the dielectric anisotropy, and the bend elastic constant. The bent dimers in theory have decreased bend elastic constants and increased flexoelectric sums, and as far as we know, these could be balanced within each dimer. The fluorinated dimer stands out as having a presumably higher dipole moment, leading to a larger dielectric anisotropy and thus a more-significantly reduced threshold voltage.

7.3 Discussion

7.3.1 Material properties

At the outset, we assumed that the bent dimers would have increased flexo-electric polarisation, decreased bend elastic constants, and their addition into mixtures would increase the rotational viscosity. The data tends to corroborate these structurally-informed assumptions. Overall, the rotational viscosity seems to increase in tandem with the flexoelectric sum. Judging by the less-significant changes in the threshold voltage, decreases in both dielectric anisotropy and bend elastic constant approximately match the total increase in the flexoelectric sum. This is the case in all dimers except the fluorinated RM1914, due to its presumably higher $\Delta\epsilon$.

Between the four dimers, each represents a small structural alteration from another. From CB7CB to CB9CB we see an increase in the carbon chain length. This leads to a small decrease in the visco-flexoelectric parameter and in the reduced threshold voltage for the longer chain dimer, however both of these differences are within error. The longer chain could possibly provide greater flexibility and so reduced rotational viscosity. It also may contribute to a slightly higher bend elastic constant. The effect is, however, not significant at this level. RM1704 has a 9-carbon chain which is stiffened and shortened by two triple bonds. The raw and adjusted τV data suggest that it most closely matches the properties of CB7CB rather than CB9CB, but from fitting analysis we once again see that the differences are insignificant within error. Its visco-flexoelectric parameter more closely matches CB9CB, as in it is lower than CB7CB, but these deviations are within error. All three have a reduced visco-flexoelectric parameter when compared to the un-doped MLC6204-000 but an insignificant change in the adjusted threshold voltage. RM1914, the fluorinated 9-carbon chain dimer, exhibits different behaviour to the other dimers at the 10 %wt level. Its visco-flexoelectric parameter is higher, closer to the pure material, but the reduction in its threshold voltage is significant within error.

7.3.2 Device performance

At the core of this work was the assumption that improved flexoelectric coefficients from the bent dimers would improve display performance in ZBD. The flexoelectric sum affects both parameters in the τV fitting - the "visco-flexoelectric parameter," which impacts the short-pulse behaviour of the device, and the threshold voltage, which determines the lower limit for latching voltage in the device at long pulse durations. Pre-accounting for the anchoring strength in the cells, we see limited improvement in both values, though not concurrently. Three dimers, CB7CB, CB9CB, and RM1704, improve (lower) the first parameter, meaning reduced operating voltages at short pulse durations. The final dimer offers no improvement in this regard but does appear to lower the threshold voltage, which gives lower overall latching voltages across the range for equivalent visco-flexoelectric behaviour. The increased viscosity would slow response times; however in a bistable device the response times are less crucial than in other, active-matrix devices.

None of the dimers worsen performance in the aspects of these two parameters; however, they do worsen performance overall by requiring the use of higher anchoring strength gratings. It is notoriously difficult to anchor bent molecules homeotropically [81, 82] and this system is no exception. At concentrations up to 15 %wt we saw reductions in C-state stability in each mixture, leading to the use of higher anchoring strength cells to maintain latching at a range of pulse widths. Even with this allowance, latching into the C-state was not possible in most mixtures at pulses shorter than 2 ms. Combined with this instability, the use of the higher anchoring increased the fields needed to latch in each instance. For analysis' sake, we were able to compensate for this effect, but for the most part higher anchoring means higher latching fields over the same cell gap. Increasing the concentration of the dimers to increase their flexoelectric benefits only exacerbates the anchoring problem. To take advantage of the benefits of doping with flexoelectric dimers would require a mixture- or anchoring-design which properly compensates for this detriment. The fluorinated dimer RM1914

is the best candidate to begin further investigation.

7.4   Conclusion

An exploratory experiment was conducted to determine the efficacy of adding odd-chain dimers as flexoelectric dopants for increased performance in ZBD. A number of issues were present which limit the potential benefits.

On the surface, the dimer mixtures appeared to improve the threshold voltage somewhat, a primary measure of performance for the device. However larger improvements required stronger homeotropic anchoring in order to maintain bistability, which in turn increased the threshold voltage. Additionally, once the uncertainties were examined, this improvement disappeared within error. The likely cause of this is the reduction of the bend elastic constant, as this serves to increase the threshold voltage. Additionally, the dimers as dopants were soluble only up to 15 %wt within the chosen host mixture.

There is enough promise with respect to the results to consider building a bespoke mixture from the ground up, including these dimers. Care would need to be taken to mitigate the effects of a decreasing bend elastic constant, solubility, and the disruption of homeotropic anchoring.

Chapter 8

Altering the grating profile

8.1 Justification

The key to the ZBD technology is the surface alignment grating. It is the root of bistability within the device. Beyond being the source of bistability, its properties govern the energy profile of the bistable states, the propagation of applied electric fields, and affect the optics of the final product.

Commercially available ZBDs contain an 800 nm pitch, 1000 nm amplitude near-sinusoidal grating with a small degree of blaze. The grating is composed of a cured photopolymer embossed to give negligible or zero offset from the ITO glass surface. A schematic grating example is included in Figure 8.1. In this configuration, the D state is of lower overall free energy than the C state for
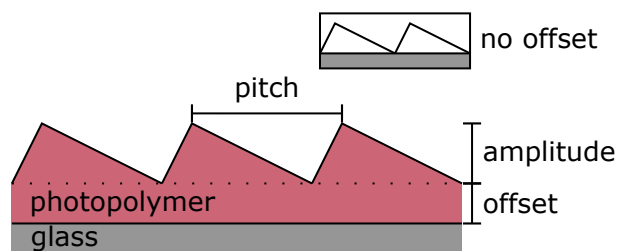
Figure 8.1: Diagram of an example grating, indicating pitch, amplitude, and offset. The grating pictured is a blazed sawtooth; ZBD gratings are near-sinusoidal.

nematic LCs, meaning it takes lower voltages to blank to this state during device addressing. The inclusion of a dielectric medium within the device leads to field losses when considering the liquid crystal material; these losses increase with increasing applied voltage, and can lead to the grating experiencing the majority of the electrical potential. Additionally, the high amplitude of the grating and the scale of the pitch lead to significant optical diffraction in the visible range; only by index matching the liquid crystal material to the refractive index of the grating photopolymer can this be ameliorated. Without such matching, the grating contributes significantly to optical losses.

During this research we were able to explore the implications of modifying the grating structure. If we can maintain bistability at lower pitch gratings, we can reduce the adverse interactions. Lower amplitudes decrease diffractive effects and reduce dielectric losses, leading to lower operating voltages and higher optical quality.

Single polariser mode ZBD would benefit greatly from reduced diffractive effects. In this mode, a linear polariser fronts the grating substrate and the device has a rear reflector for reflective or transflective operation (Figure 8.2). Three device configurations for this mode are given in [39]: two retardation modes using VAN/HAN and a polarisation-rotation mode using TN/HAN. In the paper, their optics are solved for bright and dark states using Jones' matrices through manipulation of the polariser angle to the grating β, birefringence $\Delta\varepsilon$, cell gap d, and the twist angle φ in the case of TN/HAN. Each of the three requires an angle β to the grating which will result in diffraction from the grating substrate. The combination of high reflectivity and low power is ideal for portable displays; by mitigating the diffraction at the grating, single polariser operation will be available for ZBD.

Electron beam lithography was chosen to attempt this. This uses a focused beam to expose an electron-sensitive resist, analogous to direct write laser (DWL) lithography and photoresists. With the right processing, E-beam lithography can achieve nanoscale gratings to a high standard. Depending on application, these can then be transferred to a desired substrate. For our uses, we wished to transfer
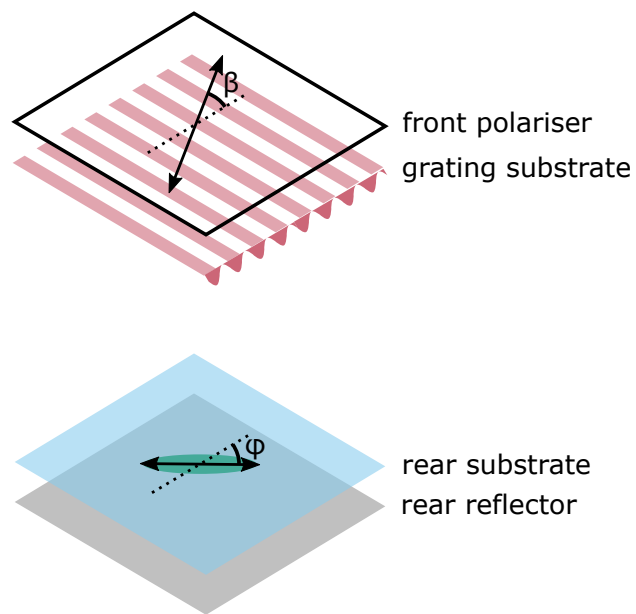
Figure 8.2: Example setup for TN/HAN single-polariser operation. Equivalently, the rear substrate can have homeotropic alignment to demonstrate VAN/HAN operation. β gives the angle between the polariser and the grating vector and φ gives the twist angle.
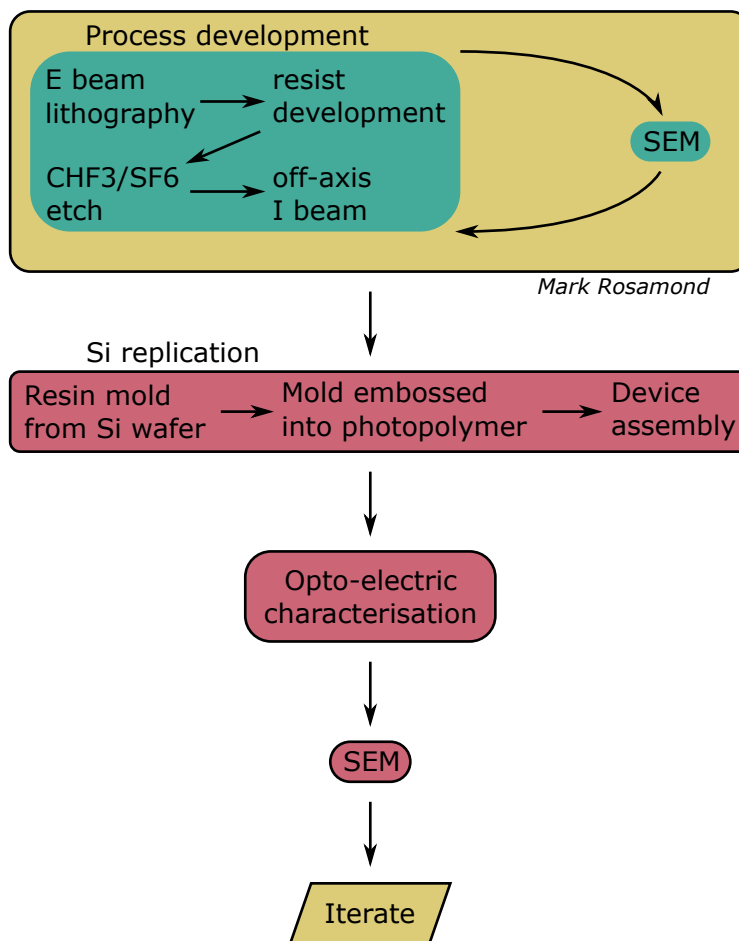
Figure 8.3: Flowchart detailing the processes involved in the initial round of novel grating fabrication.

the grating into silicon to give a hard material for use as a master. This would be achieved through etching.

8.2 Grating fabrication

Grating fabrication was done in collaboration with the Electrical and Electronic Engineering department. Primary to the collaboration was the work of Dr. Mark Rosamond, who developed the processing to give desired results and delivered on silicon masters to begin the work. It proceeded in four parts:

- Fabrication process development [M. R.],

- Silicon master fabrication [M. R.],

- Replication from master to device [S. J.], and

- Device analysis [S. J.].

Further detail of the device development is presented as a flowchart in Figure 8.3. Once the fabrication process was developed to a satisfactory standard, the masters were produced and delivered to the labs in the physics department. From here, gratings were replicated and included in device prototypes.

No specific grating shape was targeted. The pitch was controllable during the initial E-beam write and the amplitude was maximised to the best capability of the processing. A small amount of blaze was added using ion beam milling as this is necessary to prevent frustration in the latch. Therefore, the final shapes of the gratings were a consequence of the specific processing parameters and not a desired architecture.

Naming convention

From here forward, samples will be referred to by number. These are the numbers which were assigned during processing and which persisted through replication and testing. 'Sample 1' refers to the Si master as fabricated; 'Sample 01_001' or 'Cell 01_001' refers to the first replication from sample 1, '01_002' to the second replication, and so on. To put it another way, they are written #sample number#_#replication number#. The frontward zeroes in the sample part of the cell number serve only for consistency in file names; the frontward zeroes for replication number serve the same purpose somewhat optimistically. These are consistent from fabrication to replication.

115
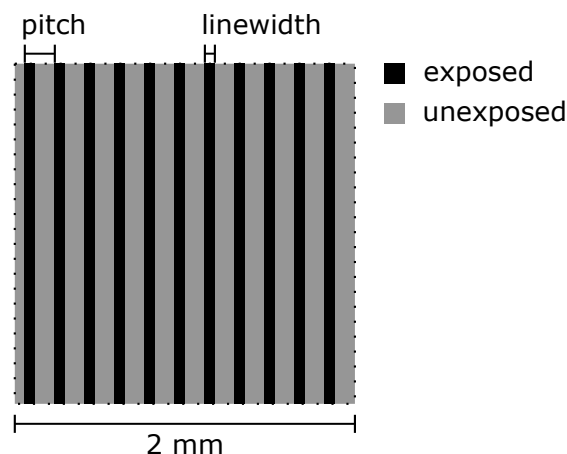
Figure 8.4: Diagram of the E beam write area. Labels are included for the pitch as defined from the write and the linewidth of the exposed lines. Not to scale.

8.2.1   Si masters: final development

The gratings were fabricated in the nanoscale using a combination of E-beam lithography, reactive ion etching (RIE), and ion-beam milling. At each stage of processing, results were taken in the form of SEM micrographs performed on the cross-sectioned samples. The positive E-beam resist, ZEP520A, was spun down onto a 3" silicon wafer at 3.5 krpm to a thickness of 390 nm. The E-beam write lines were defined separately for each of the different samples by the line width and the pitch of the desired grating (Figure 8.4). All were exposed at 2.0 nA with a 10 nm shot pitch. The box dose was 206 µC/cm^2 and each 2 mm $\times$ 2 mm area was exposed twice in different fields. Current and deflector gain were reconfigured every half hour.

After exposure, the resist was developed in n-amylacetate, removing the exposed regions (Figure 8.5). At this stage, the wafer was scribed to separate the different sample chips. Different line widths etch at different rates due to a microloading effect so it is essential that each sample is etched separately. The etch rate is dependent on the total exposed Si area (the loading effect); during etch, local variations in the etch rate are seen corresponding with local variations in the pattern density. This is caused by the local depletion of reactive species [83].

116

The wafers were etched using RIE (Figure 8.6). During etch, each chip was placed on a 2" carrier wafer to maintain a constant exposed Si area. Gas flow was set to 32 sccm CHF_3 and 15 sccm SF_6; power to 100 W; chamber pressure to 27 mTorr. The majority of the samples were etched for 2 min 15 s; however, samples 4, 5, and 6 were etched for 2 min only and samples 1, 2, and 3 were etched for 2 min 30 s. Post-etch, the remaining resist was removed using Microposit remover 1165, and the samples cleaned in 3:1 by volume of H_2SO_4 and H_2O_2 (Figure 8.7).

In order to introduce blaze and prevent frustration of the director field, the samples were milled using an ion beam off-axis (Figure 8.7). Samples 5, 7, 9, 10, and 12 were milled 10 ° from the surface normal and the rest were milled at 20 °. The ion source was set to 250 W for all samples, with an accelerating voltage of 715 V, a 500 V beam and 200 mA neutraliser. Gas was introduced at 6 sccm plus 15 sccm Ar. 7 mbar He was used for cooling to 20 °C on the back of the sample. Current was set to 0.48 mA/cm^2.
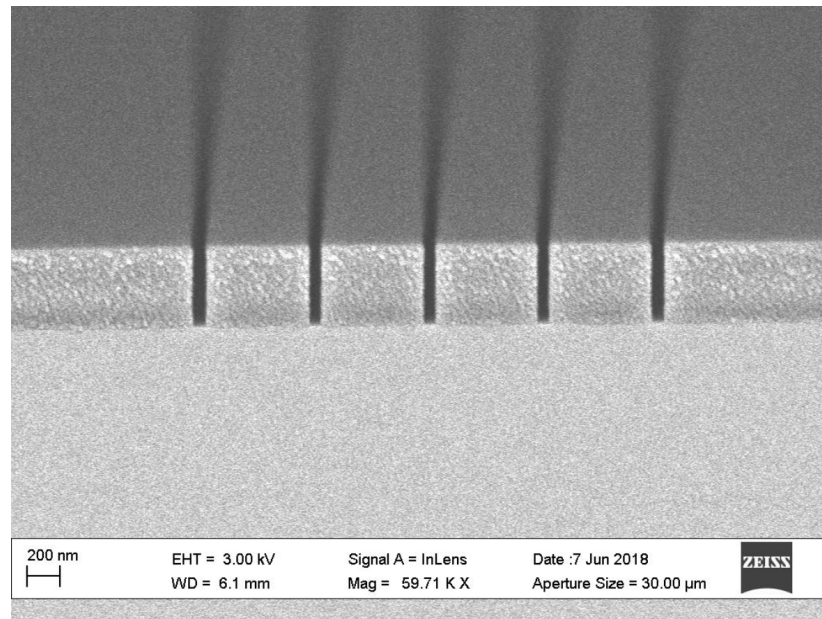
Figure 8.5: SEM image of a process development test sample. Interstitial regions of exposed resist have been removed to give grooves. SEM taken by Mark Rosamund.

117
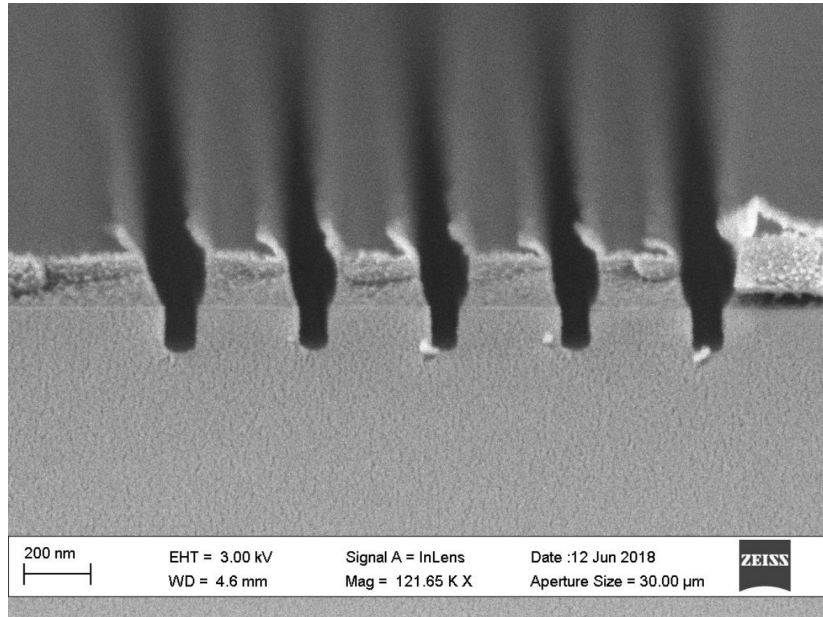
Figure 8.6: SEM image of a process development test sample. RIE has etched through the resist and into the silicon wafer below. SEM taken by Mark Rosamund.

Only samples 1, 4, 5, 7, 8, 9, 10, 11, and 12 were delivered from engineering following processing. The fate of the remaining samples is unknown.

In Table 8.1, processing parameters are summarised and matched to appropriate measurable values from Si sample SEMs. Pitch and linewidth are as defined from the E beam write; blaze angle was measured from the surface plane.

The longer etch time corresponds with the lowest amplitude (68 nm). At the shorter etch time, we see a range of amplitudes 180-250 nm. The higher mill angle from the I-beam step appears to correspond overall with a lower blaze angle; ordinarily between 65-80 nm although sample 1 milled at 20 ° has a much lower blaze angle possibly due to its longer etch time. The written linewidth is seen to have a negative correlation to the measured FWHM of the grating, as expected; the linewidth defines the gaps in the resist into which the etchant acts.
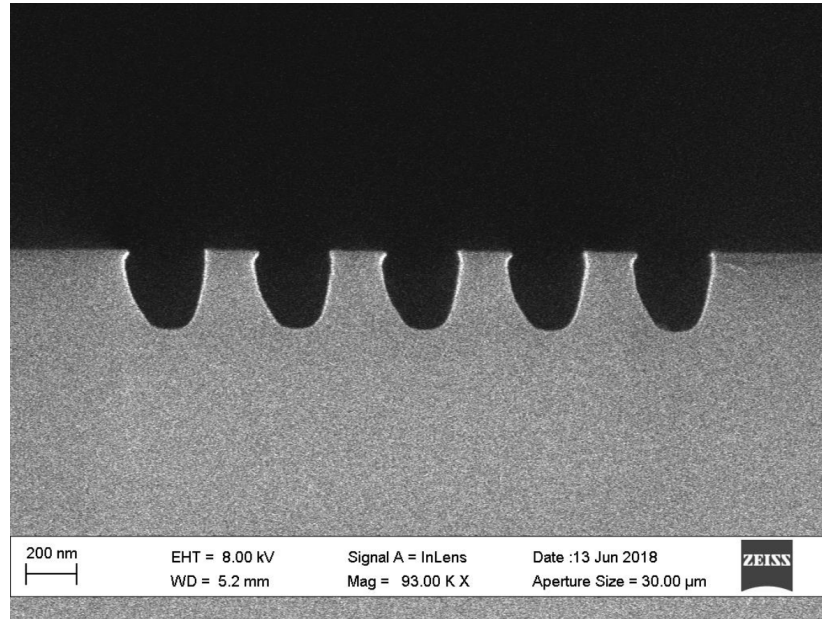
Figure 8.7: SEM image of a process development test sample. A 45 ° ion beam exposure has introduced blaze to the Si grating. SEM taken by Mark Rosamund.

Sample	Pitch (nm)	Linewidth (nm)	FWHM (nm)	Etch time (s)	Amplitude (nm)	Mill angle (°)	Blaze (°)
1	300	100	97	150	68	20	52
7	300	40	119	120	182	10	72
8	400	75	196	120	226	20	67
9	400	150	63	120	248	10	70
10	400	50	232	120	223	10	76
11	400	100	132	120	233	20	66
12	300	40	89	120	225	10	66

Table 8.1: Table of processing parameters and corresponding SEM measured values from the etched Si gratings.

This correlation differs by pitch and is found to be linear for the 400 nm samples - $FWHM = (320 \pm 70) - (1.7 \pm 0.6) * linewidth$.

119
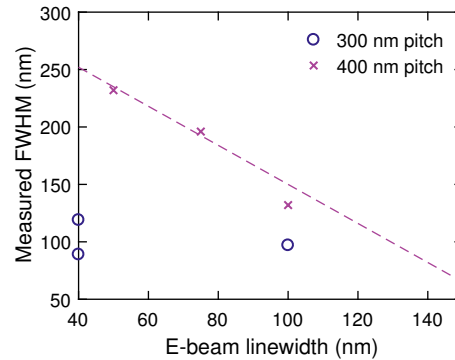
Figure 8.8: Plot of E beam linewidth vs the Si gratings' measured FWHM. The included linear fit for the 400 nm samples is defined by FWHM $= (320 \pm 70) - (1.7 \pm 0.6)$linewidth.

8.3 Grating replication from Si masters

The next stage in the process was to transfer the master grating into photopolymer and onto ITO in order to perform optical and electrical analysis of the assembled device. From the master, it was possible to create a positive or negative replication. Use of a single intermediary replicant would give a replication of the grating as it was etched; use of two intermediaries would give the inverse replication. Both of these routes were attempted, however only the single intermediary route proved robust enough to carry forward.

The process was as follows:

- Si chip cleaned in methanol and dried using compressed nitrogen,

- Mellinex 506 (125 µm) film washed in de-ionised water and dried using compressed nitrogen,

- 0.5 µL resin (4 % photo-initiator added to a 3:2 mixture by weight of TMPTMA (trimethylolporopane trimethacrylate) and Actilane 420) applied to the master grating,

- Mellinex film applied to resin-topped Si chip,

- Three minute UV cure of the resin,

Figure 8.9: An example of the layers present in the replicated samples' SEMs. This image is of sample 07_001; the scale bar represents 100 nm. The tell-tale orange peel texture of sputtered gold is most obvious on the underlying glass. EHT = 20 kV, WD = 3.1 mm, SignalA = InLens, aperture size = 30 µm.

- ITO glass cleaned in UV-O$_3$ and treated with adhesion promoter,

- 2 µL homeotropic-anchoring photopolymer applied to ITO glass,

- Resin-on-film grating embossed into photopolymer-on-glass at 4 bar, 1 mm/s,

- Embossed substrate cured for 4 mins, and

- 5 µm cells assembled opposite homeotropic (Nissan SE1211) surface.

The alternative two stage replication process involved a PDMS intermediary taken from the Si master, and the resin replication taken from that. Even under vacuum, it wasn't possible to reliably fill the nanometre-scale grooves with the uncured PDMS, giving poor replication. Additionally, the PDMS left residue in the masters after lift-off. Clean up after the resin step was relatively straightforward.

Replication was examined by fracturing the Si masters and the replicated samples after use. The photopolymer samples were also sputtered with approximately 5 nm of gold to reduce charging effects. The sputtered gold can be seen in the SEMs as an orange-peel texture. This texture, and the photopolymer/ITO/glass layers are typified in Figure 8.9. SEM images are included for both the Si masters and the example replicated samples in Figures 8.10, 8.11, and 8.12. Overall, we
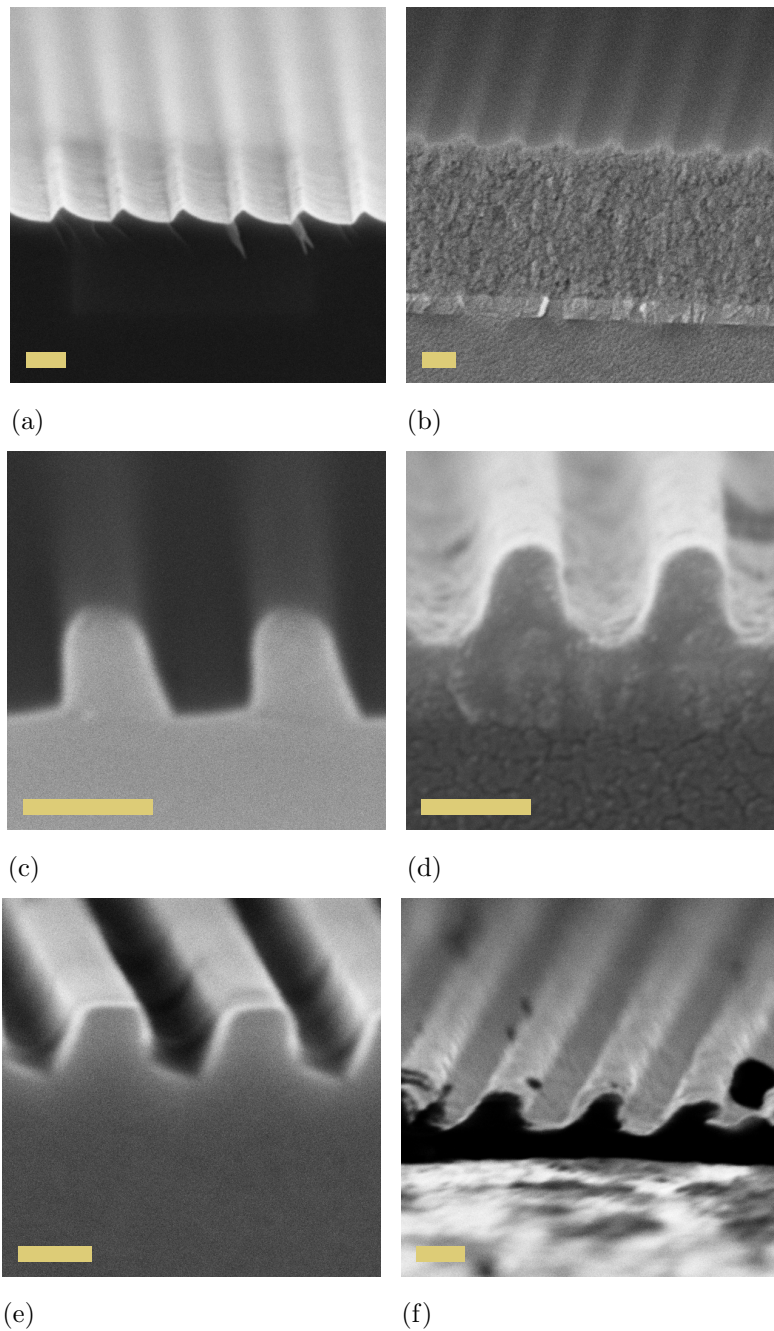
Figure 8.10: SEM images of sample 1 (a) Si master and (b) replication, sample 7 (c) Si master and (d) replication, and sample 8 (e) Si master and (f) replication. Included scale bars represent 200 nm. In the replicants we see three distinct layers: first the glass, then the ITO, then the photopolymer layer embossed with the grating. SEM parameters are given in Table 8.2 at the close of this section.

(a)

(b)

(c)

(d)

(e)

(f)
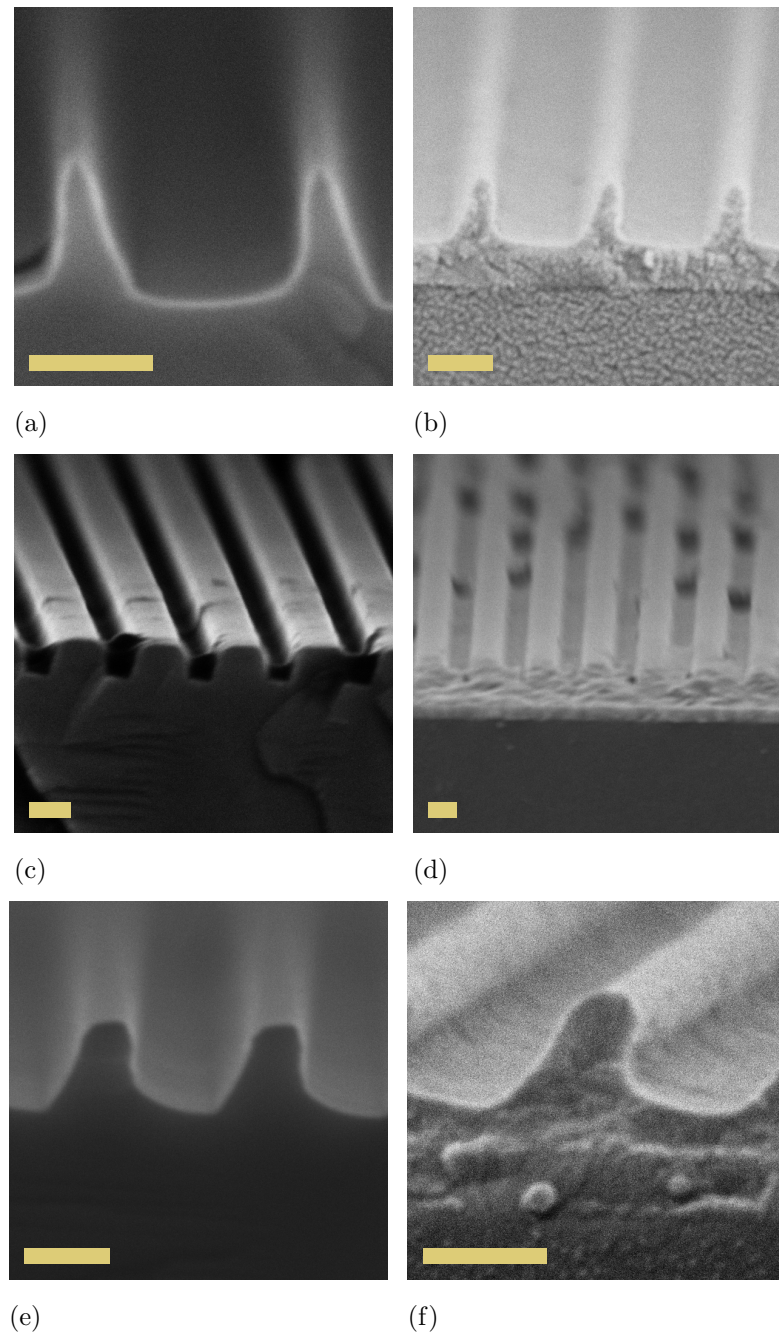
Figure 8.11: SEM images of sample 9 (a) Si master and (b) replication, sample 10 (c) Si master and (d) replication, and sample 11 (e) Si master and (f) replication. Included scale bars represent 200 nm. In the replicants we see three distinct layers: first the glass, then the ITO, then the photopolymer layer embossed with the grating. SEM parameters are given in Table 8.2 at the close of this section.
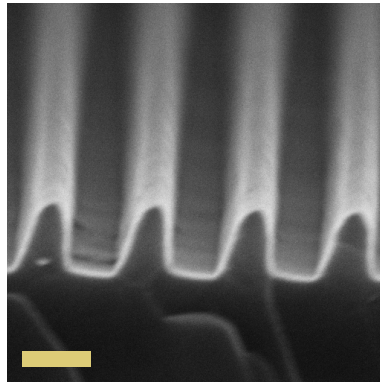
Figure 8.12: SEM image of sample 12 Si master. Included scale bar represents 200 nm. EHT = 5 kV, WD = 2.5 mm, SignalA = InLens, aperture size = 30 µm.

see good replication of the etched grating shape. The replicated samples show minimal offset, of the order of 50 - 100 nm; that is, except for sample 1 (Figure 8.10(b)), whose replicated grating has a measured average offset of 900 nm from the ITO surface. In general, the replication method given above achieves a workable offset level. The profile of the replicated gratings match well the Si gratings, with minor differences in the fidelity of sharp corners, especially at the base of the grooves (see Figure 8.10(d) as an example). Some samples were unfortunately damaged during fracture for SEM (Figure 8.10(f) and 8.11(d)).

Figure 8.13 gives examples of different aberrations which were found to occur in a minority of the replications. In Figure 8.13(a) and (b) we see minor and major photopolymer bridging across the grating grooves. We hypothesise that this is caused by reduced fidelity in the master, possibly due to a build up of uncured resin or other contaminants on the grating surface, as the major bridging occurs in the fourth replication taken from sample 10. In Figure 8.13(c) we see a replication of sample 9 that is not uniform over the area, and in fact there are large regions over which either the grating did not replicate or else did not adhere properly to the surface. Once more, this occurred in a later generation replication. The masters appear to lose viability after around the third replication.

In the majority of cases, replication exceeded expectations.
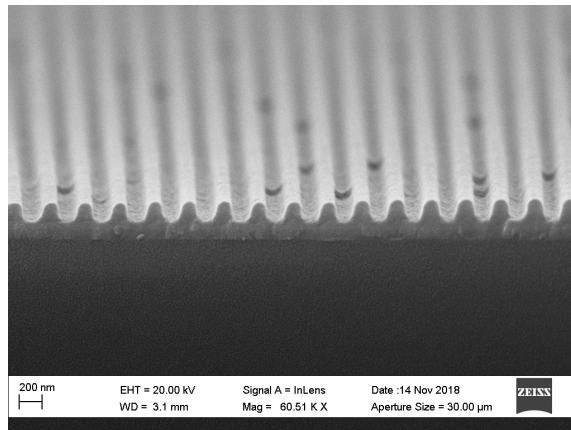
(a)
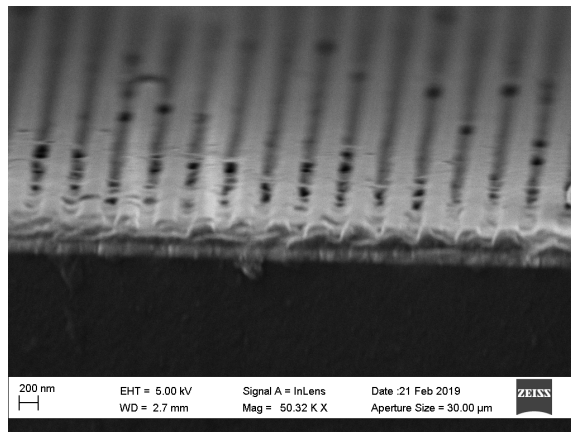
(b)
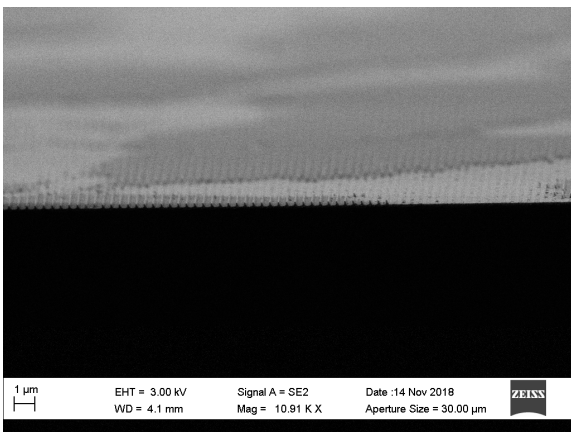
(c)

Figure 8.13: SEM images of replications from (a) sample 7, (b) sample 10, and (c) sample 9, representing different replication defects.

125

Sample		EHT (kV)	WD (mm)	Sample		EHT (kV)	WD (mm)
1	m	3	2.5	9	m	3	3.3
	r	3	3.4		r	3	2
7	m	3	4.5	10	m	5	3.9
	r	20	3.1		r	5	3
8	m	4	3.4	11	m	4	2.4
	r	4	2.4		r	20	3.8

Table 8.2: Summary of SEM accelerating voltage (EHT) and working distance (WD) for the images presented in Figures 8.10 and 8.11. Each had an aperture of 30 µm. Values are given separately for the Si master (m) and the photopolymer replicant (r).

8.4 Electro-optical testing

After replication, the 5 µm HAN/VAN cells were filled with MLC6204-000 and examined using POM. The nematic fill state was noted, the cell heated to clearing point and subsequently cooled to 30 °C. At this temperature, electrical tests were performed in a similar manner as for τV curves. Bipolar pulses of duration 3.2 ms were applied at increasing voltages to determine if the state would latch. If the state did not latch, higher temperatures were tested in turn. This was done to reduce elastic suppression of the latch. If the state did latch, in either of these two circumstances, the reverse latch was also tested for.

Filling with the nematic state is a good way to check the preferred alignment state of the grating. On cooling, the D state will always be adopted immediately below the nematic to isotropic phase transition due to what is essentially the condensation of defects within the grooves as nematic order propagates through the bulk. Depending on the temperature, i.e. the elastic profile of the nematic, the cooling cell may transition to C state if the grating shape favours it significantly.
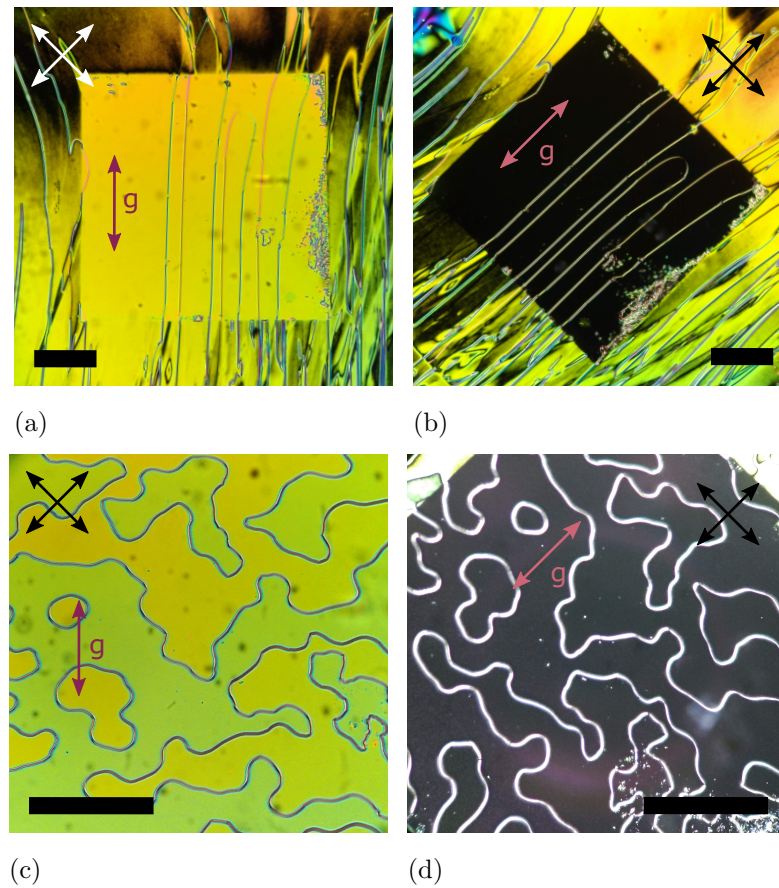
Figure 8.14: POM examples for fill alignment (a) and (b) and isotropic to nematic cooling alignment (c) and (d). Each were taken from sample 07_002; 500 µm scale bars are included, as are the grating vector and polariser/analyser alignments.

The fill state is a snapshot of the grating alignment outside of the influence of the isotropic-to-nematic defects. It should be noted that the fill state may be influenced by flow alignment also; for the most part final observations were taken minutes after filling, which will compensate for the flow alignment in some regard but might not allow for full relaxation. Examples for both alignment checks are shown in Figure 8.14. In this sample and in others, the cooled alignment showed two regions separated by disclinations (clearest in Figure 8.14(c)). These represent different splay directions for the hybrid-aligned D state. The presence of these domains can be suppressed by cooling slowly, or removed entirely by properly constructing the grating such to consistently favour one over the other.

127

From the initial test samples, three different stability profiles were found. Two samples exhibited C state monostability, where they cooled into the continuous state and could not be latched into the defect state. Three more were D state monostable, in that they would adopt and maintain the D state on cooling but would not latch. A final set of three samples did achieve latch; these were attributed as D state metastable due to their ability to remain in D state on cooling but an inability, once latched, to return to D state through electrical means. Each of these cases will be discussed in their respective sections.

8.4.1 C-state monostability

One sample, designated sample 1, was found to be monostable in the continuous state. On cooling, directly below the clearing temperature, the cell adopted the continuous state and would not latch. Another, sample 11, adopted a tilted C state (C*) only. This state appeared brighter than sample 1, but had very low birefringence, and again would not latch.

| Name | Replication | State | | Latch | Profile (nm) | | A.R. |
		Filling	Cooling		Linewidth	Pitch	
01_001	Yes	C	C	No			
01_002	No	-	-	-	100	300	0.24
11_001	Yes	C*	C*	No			
11_002	Yes	C*	D	No	100	400	0.57
11_003	Yes	C*	C*	No			

Table 8.3: Table of observations from sample 1 and 11 replications.

Due to the very low aspect ratio (A.R.) of grating 1 - 0.24 amplitude/pitch - the D state cannot be supported. Of all the 400 nm pitch gratings, the rest of

which will be discussed shortly, sample 11 is the only one which does not latch at all. This is due to its inability to support the D state but the origin of this factor is unclear.

8.4.2 D-state monostability

Samples 5, 7, and 12 filled and cooled into D state but did not latch. Samples 7 and 12, incidentally, had the same linewidth (40 nm) and pitch (300 nm) from the E-beam step. The Si master for sample 12 was a chip from the corner of the Si wafer. Replication was difficult, and no replication of the full area was achieved.

| Name | Replication | State | | Latch | Profile (nm) | | |
		Filling	Cooling		Linewidth	Pitch	A.R.
05_001	Yes	D	D	No	50	300	No data
07_001	No	-	-	-	40	300	0.56
07_002	Yes	D	D	No			
12_001	Yes	D	D/C*	No	40	300	0.74
12_002	Yes	D	D	No			

Table 8.4: Table of observations from sample 5, 7, and 12 replications.

The determining factor for these samples' lack of latch is assumed to be their low pitch. Each has 300 nm pitch, and latching is only seen in the 400 nm pitch samples. Sample 12 has a higher aspect ratio which is preferable, however with its replication difficulties and without a latch, it does not appear to have benefited the sample.

8.4.3   D-state metastablity

Samples 8, 9, and 10 each had at least one replication which latched from D to C state. They mostly cooled into D state, often with very good alignment, and portions of the grating would latch under bistable pulses. However, those samples which latched to C state would not latch back. The reverse bipolar pulse for selecting C state, even up to 75 V, showed only minute regions of D state latch. Samples which latched did so at 30 °C; temperature increases did not increase latching success.

| Name | Replication | State | | | Profile (nm) | | |
		Filling	Cooling	Latch	Linewidth	Pitch	A.R.
08_001	No	-	-	-			
08_002	Yes	D	C	Unstable	75	400	0.46
08_003	Yes	D	D	Partial			
08_004	Yes	D	D	No			
09_001	Yes	D/C	D	Total			
09_002	Yes	None	D	No	150	400	0.62
09_003	Yes	C	C	Total			
10_001	Yes	D	D	Partial			
10_002	Yes	D/C	D	Partial	50	400	0.53
10_003	Yes	None	D	No			
10_004	Yes	D	D	No			

Table 8.5: Table of observations from sample 8, 9, and 10 replications.

Of each of the cells above that latched, only 08_003 had a demonstrable latch from C to D (Figure 8.16). Even this was over small regions, and did not fully reverse the regions that latched D to C. We even see, from 20 V to 30 V, some small regions of reverse latch back to C state (Figure 8.16(c) and (d)).

130
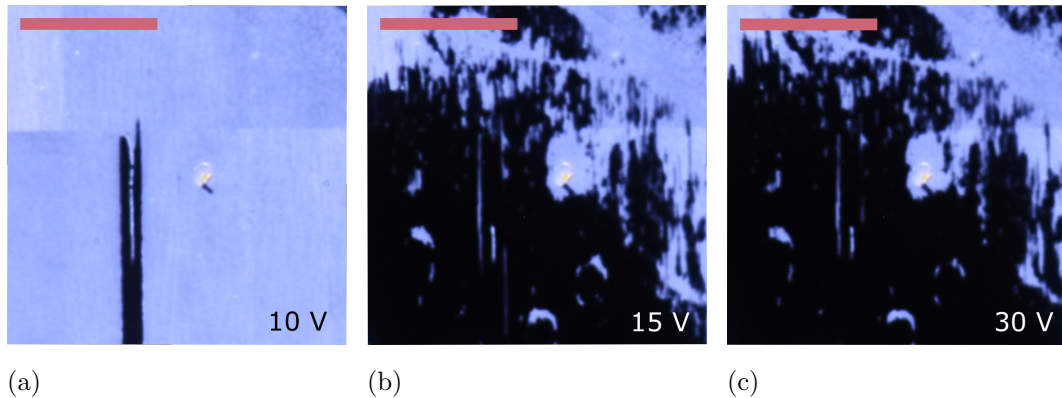
Figure 8.15: POM images of sample 08_003 latching from D to C state. Polarisers were crossed at 45 ° to the grating vector giving bright HAN (D) and dark VAN (C) states. The voltage indicated represents the amplitude of the bipolar pulse; for D-C latching the trailing (latch) pulse is negative. Scale bars indicate 100 µm.

The success of the latching samples is overall attributed to their longer pitch of 400 nm. They are judged to be metastable in D: the state is stable enough to remain on cooling, however under electrical impulse any C state which latches sticks except on heating. There are two possible causes for a strongly favoured C state: too-strong anchoring at the grating surface or low aspect ratio.

At the outset, the replications were all done using the highest anchoring strength photopolymer (PPB, $W_\theta = 8.4 \times 10^{-5}$ J/m^2, Chapter 5), due to the assumption of higher elastic distortion energy resulting from the smaller gratings. Once the D state metastability was observed in these samples, subsequent replications were performed using a lower anchoring strength (5.4×10^{-5} J/m^2). The cells which used this lower anchoring strength were: 08_003, 08_004, 09_002, 09_003, 10_003, and 10_004. No improvement was seen.

After discounting anchoring strength as the cause, we can infer that the gratings made have too low an amplitude in accordance with their pitch, leading to C state stability over the D state. For comparison with the calculated aspect ratios given above, the grating in commercial ZBDs has an A.R. (amplitude/pitch) of 1.25. A direct comparison of the grating profiles of each sample is given for the

131
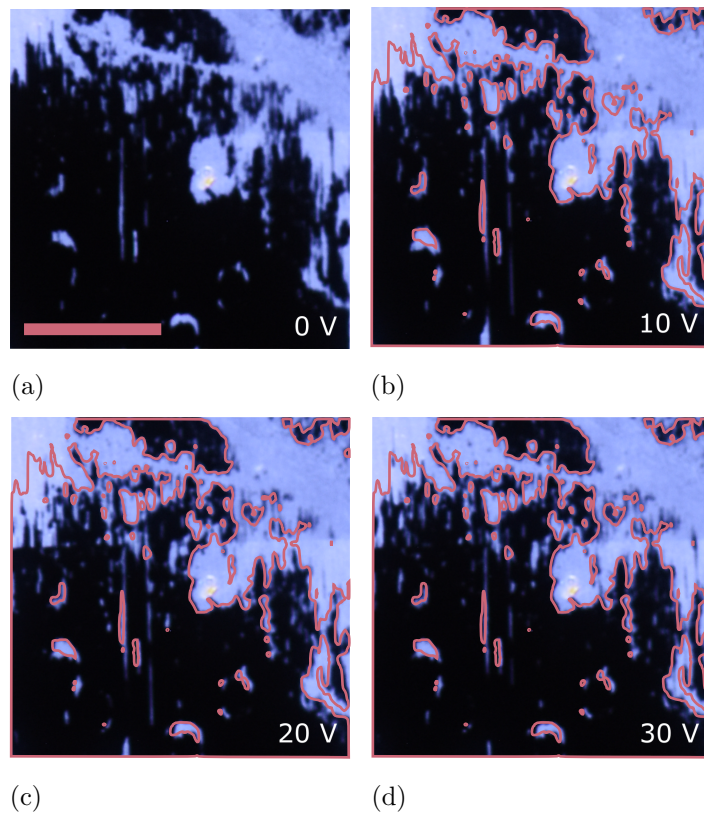
Figure 8.16: POM images of sample 08_003 latching from C to D state. Polarisers were crossed at 45 ° to the grating vector giving bright HAN (D) and dark VAN (C) states. The voltage indicated represents the amplitude of the bipolar pulse; for C-D latching the trailing (latch) pulse is positive. The D/C state boundary from the 0 V image is included on top of each subsequent image in order to highlight the small regions of latch. Scale bar indicates 100 µm.

300 nm pitch samples in Figure 8.17 and for the 400 nm samples in Figure 8.18.

Sample 4's Si master was broken in the first replication, which was unsuccessful, so no data was gathered.
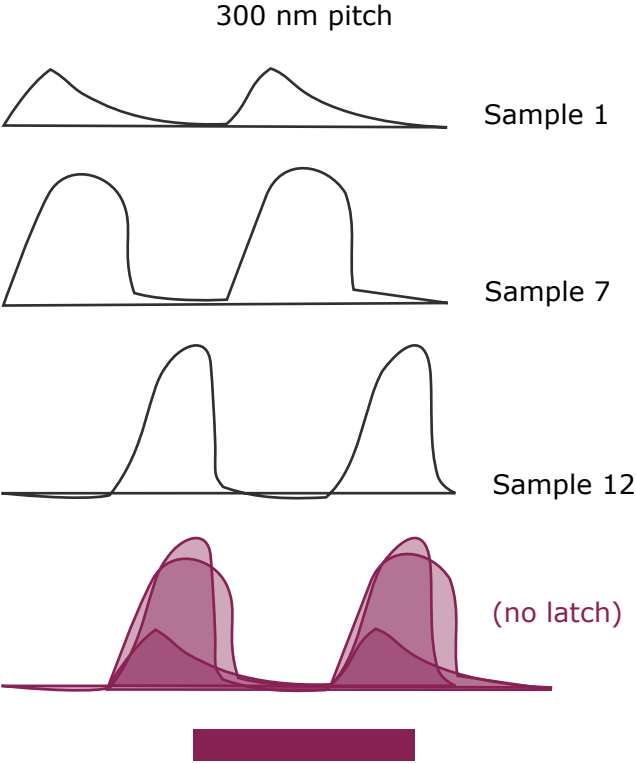
Figure 8.17: Traces of the SEM profiles for each sample, including overlap for comparison. Shown in purple are the profiles which gave no latch; the scale bar corresponds to 300 nm.
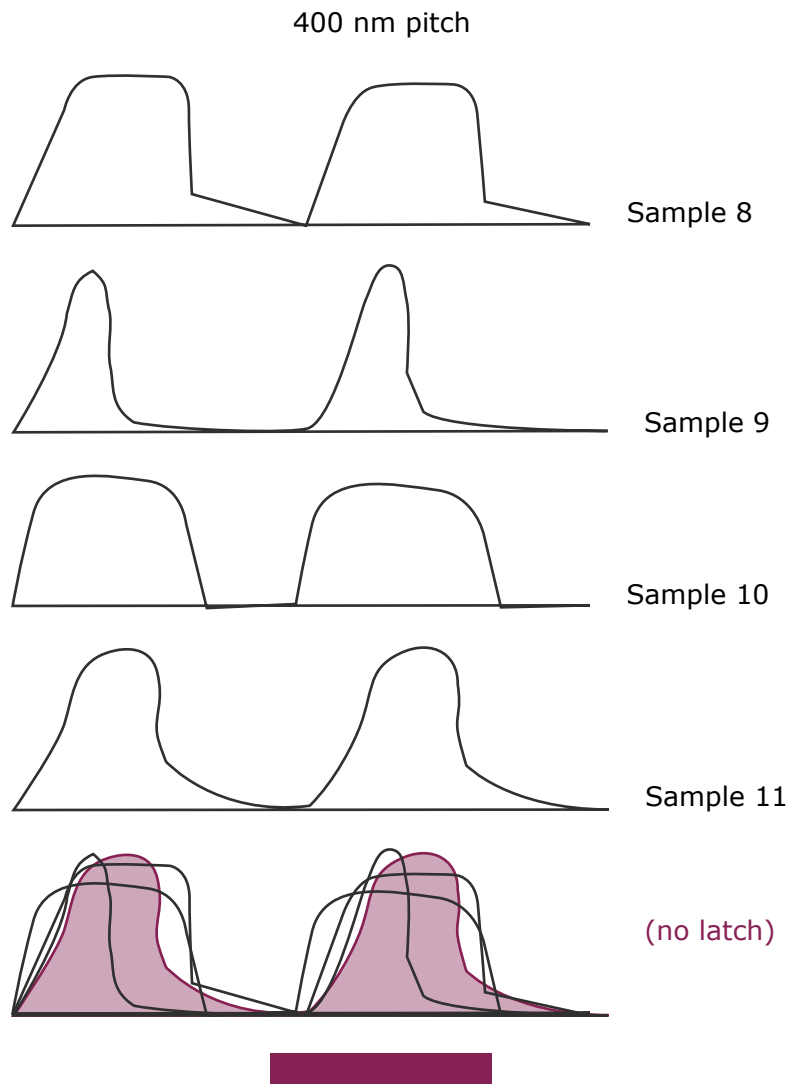
Figure 8.18: Traces of the SEM profiles for each sample, including overlap for comparison. Shown in purple are the profiles which gave no latch; the scale bar corresponds to 300 nm.

8.5   Conclusion

A method for shorter pitch ZBD gratings, targeting 300 - 400 nm, was presented in full. This method is a combination of E-beam lithography, reactive ion etching, and I-beam milling to define masters in a silicon wafer, and nanoscale replication and embossing, to fabricate new ZBD cells for evaluation. SEM image analysis provides evidence for the fidelity of the replication, which was good, but lacking in reproduction of sharp corners and broke down for later generation replications.

In ZBD operation tests, three results were seen among the samples: C state monostability, D state monostability, and D state metastability. In the latter, latching was seen using the bipolar pulse waveforms used in the original device. However, this was only seen from defect to continuous state in any significant capacity. Anchoring strength was ruled out as the mitigating factor, and so we conclude that the aspect ratio of the produced gratings is too low to support both bistable states. In order to produce workable bistable gratings a new process must be developed. Possibilities for this will be discussed in the following section.

8.6   Further work

The key issue with the gratings appears to be that they are not of a high enough aspect ratio and so will not latch both directions, despite two stable states co-existing. The limiting factor here is the selectivity of the E-beam resist to the ion etching; at the current chemistry available in the engineering department, deeper etches are not possible without destroying the resist mask. In order to move forward, different strategies should be considered. The key factors needed are: high aspect ratio (targeting 1:1 and higher amplitude to pitch), mechanical stability for mastering, and pitches of 200 - 400 nm. The E-beam lithography itself can achieve high aspect ratios at the desired length scales, but the resist would not be hard enough for mastering.

8. ALTERING THE GRATING PROFILE

One possible method would be to electroplate nickel onto the developed resist. Process development would need to account for wetting behaviour into the grooves, uniformity of the electro-forming, roughness, overplating, and possible deformations of the resist. The resist itself can achieve between 3:1 and 4:1 aspect ratio before collapse.

Another would be to etch directly into a resist, one which is harder than the ZEP used in this instance. This would involve use of a chrome hard mask and etch with O_2 plasma. Even with a harder resist, this method poses risks of mechanical instability during replication.

A third possibility would be liquid KOH etching of Si. Different crystal planes of Si etch at different rates, allowing for limited structures to be etched directly into the Si wafer. Namely, the (111) plane etches much slower (two orders of magnitude) than the (110) plane, meaning that deep trenches can be etched into the latter plane with (111) sidewalls [84]. The structure limitations discount this method, but it might be worth considering further down the line.

The selected method for the second iteration, which at the time of writing is not yet in progress, is the use of metal-assisted chemical etching (MaCE or MacEtch) [85]. This method is a wet etch, meaning it uses a liquid etchant in contrast with the plasma of dry etching methods like RIE. A noble metal, such as Au, Pt, or Ag, is used as a cathode on the Si anode. The metal acts as a catalyst for a reduction reaction; at the cathode (the metal), this produces ionic silicon Si^{+4}, which is soluble in acids such as HF, where Si is not. This process does not involve significant consumption of the metal and so can progress even to very high aspect ratios, etching only where the metal is deposited. The nanoscale pattern required is 'written' in the metal cathode through methods such as lithography, through patterning or sputtering. While relatively new, MaCE represents a good candidate for fabrication of high-aspect ratio grating masters of the correct scale and of high mechanical stability.

136

A note on process development

This work was made possible only through the expertise of the School of Electronic and Electrical Engineering, most notably Dr. Mark Rosamund, who developed the processing for the first iteration of gratings and will be involved in all further work. The stages and parameters for the final process are included in this thesis, as are notes on alternative processes, for the purposes of reproducibility and future continuation of the work. They represent a great deal of research and experience which is beyond the scope of this thesis.

Chapter 9

Conclusion

The zenithal bistable display is a commercially successful bistable nematic LCD. The technology is distributed by DisplayData as shelf-edge labels for the retail market, including supermarkets and consumer electronics stores. The grating alignment surface is responsible for bistability in the device, and the associated dynamics are of unique interest. However, the grating also introduces optical and electrical losses to the device. This thesis set about to further explore the physics of the ZBD and to initiate research into improvements to its performance.

The problem of the device dynamics were investigated through both experimental and computational methods. This included fabrication of ZBD devices, electro-optical assessments, device modelling, and LC mixture doping. The question of improving upon the grating surface was tackled using novel grating fabrication methods.

Results for each of these aspects of the research were presented in four chapters.

In the first, evaluation of device performance was introduced, and a method of anchoring strength assessment established. Gratings of known silane density were built into devices and tested for their anchoring strength. This was found to correlate strongly to the silane groups present. Anchoring strengths in the range $0.5 - 2 \times 10^{-4}$ J/m^2 were demonstrated. The method is presented in such

a way as to allow for reproducibility in other labs. This also provides a method for controllable-strength homeotropic alignment at microstructures for any LC device.

The second results chapter detailed computational and experimental studies into the defect dynamics within the bistable latching. Three latches were tested through modelling: the C-D latch, D-C latch, and the RMS latch. Each of these were compared to experiment, and previously un-accounted for behaviour, namely the suppression of the C-D latch, was illuminated for the first time. Partial latching behaviour was examined experimentally, and the previous modelling work indicated the cause of this behaviour being linked to the defect dynamics at different timescales. Additionally, defect behaviour under an electric field was modelled in detail and an effective charge/mass quantity was found.

In the third results chapter, LC dimers were doped into a display mixture for use in ZBD. The performance of these doped mixtures were evaluated per the latching behaviour. The materials indicate an improvement to the latching voltages, and were limited ultimately by viscosity effects.

Finally, in the fourth results chapter, initial testing was undertaken on new grating structures manufactured at half the scale of current ZBD gratings. These were replicated into test devices and their performance assessed. Some successful latching was seen, indicating potential for bistable alignment gratings of a scale which mitigates their optical and electrical losses. This research strand has strong directionality for future work.

Through this work, the potential for ZBD in the future has been illuminated. The mixture work and the fabrication of new gratings indicate possibility of ZBDs with lower operating voltages and higher optical quality. Together they could lead to devices with longer lifetimes and new display configurations for wide applications. Single polariser mode and double ZBD were the targets; the research has brought us closer to those applications. Additionally, there remains much to be discovered with regard to the physics of the device. The surface treatment

work allows for other researchers to more easily fabricate ZBDs, opening up more research opportunities. The modelling work indicates a wealth of dynamical observations with regard to the bistable latching and some interesting physics in addition.

Further work could build upon this thesis in a number of ways, particularly the mixture work and that of new grating fabrication. Further work could also be conducted to remove ambiguity in the anchoring strength work and the modelling. The mixture work could be extended by purpose-building a display quality mixture, i.e. with suitable temperature range and dielectric anisotropy, with the dimers in mind as flexoelectric dopants. New mixtures could be tailored to increase solubility of the dimers and compensate for the increased viscosity. The best avenue to begin this work would be to start with binary mixtures of the dimers and comparable calamitic compounds, most likely 5CB. To limit the initial experiments, one dimer should be chosen as a focus. Two obvious choices would be CB7CB, due to the wealth of literature already available, or RM1914, as in this work it showed the most promise in ZBD. This binary mixture would be unlikely to latch well in ZBD and so optimisation of the material properties should be of priority. Mixture development should progress from the binary mixture, possibly following E7 as a skeleton for mixture components.

New iterations of the grating masters process should be undertaken to target gratings with higher aspect ratios in mind. The processing options for such gratings are summarised in Chapter 8, Section 8.6. Once successful latching is performed in both direction at a scale of 300-400 nm, smaller gratings should be investigated. If no latching is successful, then the low amplitude grating structures which achieved metastability in this thesis should be iterated upon. Certain methods, such as polymer stabilisation of the defect state, could induce bistability where none currently exists. Once a bistable prototype is developed at any scale, a full comparison should be undertaken of optical and electrical performance of the small scale grating device and a standard, 800 nm pitch ZBD cell.

9. CONCLUSION

A few issues of note remain regarding the anchoring strength measurements and the modelling work. With respect to the anchoring strength measurements, while the measurement is supported by the literature, it is experimentally unclear if the anchoring strength measured through the latch thresholds is the true anchoring strength or a defect-associated viscosity measurement, related to the mobility of the defects on the homeotropic surface. Use of silanated photopolymer flats, such as were used in the AFM and XPS measurements, should be tested through other means for their anchoring strength to remove this ambiguity. Considering the modelling work, the entirety of the work was performed on a single mesh using parameters for one material. This could be extended to work regarding the new grating shapes if new meshes were created, or to multiple grating pitches to investigate state bordering effects. More thorough comparisons could be made from modelling to experiment if the material parameters were altered to those of a known material.

At this stage, more is known about bistability in ZBD than ever before, and the work is coming closer to new display modes and greatly improved optics through changes to the grating scale.

Notes and references

[1] J. C. Jones, S. Beldon, P. Brett, M. Francis, and M. Goulding. Low Voltage Zenithal Bistable Devices with Wide Operating Windows. *SID Digest*, 2003. xix, 28, 29, 30, 33, 52, 71, 72, 87, 94, 95

[2] P. G. de Gennes and J. Prost. *The physics of liquid crystals*. Oxford University Press, 2nd edition, 1993. 6

[3] F. C. Frank. On the theory of liquid crystals. *Discussions of the Faraday Society*, 25, 1958. 7, 10

[4] S. Copar and Z. Slobodan. Quaternions and hybrid nematic disclinations. *Proceedings of the Royal Society of Mathematical, Physical, and Engineering Sciences*, 469, 2013. 9

[5] A. Yariv and P. Yeh. *Optical waves in crystals*. John Wiley and Sons, 1984. 9

[6] D. Ancdrienko. Introduction to liquid crystals. *J. Mol. Liq.*, 267, 2018. 9

[7] C. W. Oseen. The theory of liquid crystals. *Trans. Faraday Soc.*, 29, 1933. 10

[8] J. C. Jones. Liquid crystal displays. In J. P. Dakin and R. G. W. Brown, editors, *Handbook of Optoelectronics: Enabling Technologies (Volume 2)*. CRC Press, 2017. 11, 15, 23

[9] A. Bogi and S. Faetti. Elastic , dielectric and optical constants of 4 ' - Elastic , dielectric and optical constants of. *Liquid Crystals*, 28:729–739, 2001. 11, 54

NOTES AND REFERENCES

[10] H. Gruler, T. J. Scheffer, and G. Meier. Elastic constants of nematic liquid crystals. *Z. Naturforsch. A*, 27, 1972. 15

[11] H. Gruler and G. Meier. Electric field-induced deformations in oriented liquid crystals of the nematic type. *Mol. Cryst. Liq. Cryst.*, 16, 1972. 15

[12] H. J. Deuling. Deformation of Nematic Liquid Crystals in an Electric Field. *Mol. Cryst. Liq. Cryst*, 19:123–131, 1972. 15

[13] A. J. Davidson and N. J. Mottram. Flexoelectric switching in a bistable nematic device. *Physical Review E - Statistical Physics, Plasmas, Fluids, and Related Interdisciplinary Topics*, 65(5):10, may 2002. 17, 30, 31, 33, 104

[14] J. M. Jacobson. Electronicall addressable microencapsulated ink and display thereof, 1997. US Patent 6,120,588 A. 17

[15] I. N. Dozov, P. R. Martinot-Lagarde, E. Polossat, I. Lelidis, M. Giocondo, and G. E. Durand. Fast Bistable Nematic Display From Coupled Surface Anchoring Breaking. *Proceedings of the SPIE 3015, Liquid Crystal Materials, Devices, and Applications V*, 1997. 17, 27, 54

[16] G. P. Bryan-Brown, C. V. Brown, and J. C. Jones. Bistable nematic liquid crystal device, 1995. 17, 26, 29

[17] J. C. Jones. Novel Geometries of the Zenithal Bistable Device. *SID Digest*, pages 1626–1629, 2006. 18, 27, 28, 29, 32

[18] J. C. Jones and R. M. Amos. Relating Display Performance and Grating Structure of a Zenithal Bistable Display. *Mol. Cryst. Liq. Cryst.*, 543:57, 2011. 18, 28, 29, 31, 33

[19] P. M. Alt and P. Pleshko. Scanning limitations of liquid crystal displays. *IEEE Transactions on Electron Devices*, 21, 1974. 23

[20] J. C. Jones. Bistable nematic liquid crystal devices. In J. W. Goodby, P. J. Collings, T. Kato, C. Tschierske, H. F. Gleeson, and P. Raynes, editors, *Handbook of Liquid Crystals: Volume 8*. Wiley VCH, 2nd edition, 2014. 23, 26

[21] J. C. Jones, G. P. Bryan-Brown, E. L. Wood, A. Graham, P. Brett, and J. R. Hughes. Novel bistable liquid crystal displays based on grating alignment. In Ranganathan Shashidhar and Bruce Gnade, editors, *Electronic Imaging*, pages 84–93. International Society for Optics and Photonics, mar 2000. 23, 26

[22] G. Durand, R. Barberi, M. Giocondo, and P. R. Martinot-Lagarde. Nematic Liquid Crystal Display with Surface Bistability and Control by Flexoelectric Effect., 1990. US Patent US 5,357,358 A. 24, 54

[23] R. Barberi, M. Giocondo, and G. Durand. Flexoelectrically controlled surface bistable switching in nematic liquid crystals. *Appl. Phys. Lett.*, 60, 1992. 26

[24] Y. Chen, F. Peng, T. Yamaguchi, X. Song, and S.-T. Wu. High performance negative dielectric anisotropy liquid crystals for display applications. *Crystals*, 3, 2013. 26

[25] R. Chen, L. Zhao, Z. An, X. Chen, and P. Chen. Synthesis and properties of allyloxy-based tolane liquid crystals with high negative dielectric anisotropy. *Liq. Cryst.*, 44, 2017. 26

[26] G. P. Bryan-Brown, M. J. Towler, M. S. Bancroft, and D. G. McDonnell. Bistable Nematic Liquid Crystal Device., 1994. GB Patent 2,286,467 A. 26, 54

[27] G. P. Bryan-Brown, E. L. Wood, C. V. Brown, J. C. Jones, I. C. Sage, and P. Brett. Grating aligned bistable nematic devices. *Internation Displays Workshop Proceedings*, 1997. 26

[28] I. Dozov, M. Nobili, and G. Durand. Fast bistbale nematic display using monostable surface switching. *Appl. Phys. Lett.*, 70, 1997. 27

[29] I. Dozov, Ph. Martinot-Lagarde, A. Lamarqu-Forget, D. Stoenescu, J. Angele, R. Vercelletto, B. Pecout, and A. Boissier. Recent improvements of bistable nematic displays switched by anchoring breaking (binem(r)). *SID Symp. Tech. Papers*, 32, 2012. 27

NOTES AND REFERENCES

[30] S. C. Kitson and A. D. Geisow. Bistable nematic liquid crystal device, 2000. US Patent 6,903,790 B2. 27

[31] S. C. Kitson and A. D. Geisow. Controllable alignment of nematic liquid crystals around microscopic posts: Stabilization of multiple states. *Appl. Phys. Lett.*, 80, 2002. 27

[32] S. C. Kitson and A. D. Geisow. Bistable alignment of nematic liquid crystals around microscopic posts. *Mol. Cryst. Liq. Cryst.*, 412, 2004. 27

[33] G. P. Bryan-Brown, C. V. Brown, J. C. Jones, E. L. Wood, I. C. Sage, P. Brett, and J Rudin. Grating Aligned Bistable Nematic Device. *SID Digest*, pages 37–40, 1997. 27, 29, 32, 54

[34] E. L. Wood, G. P. Bryan-Brown, P. Brett, A. Graham, J. C. Jones, and J. R. Hughes. Zenithal Bistable Display (ZBD): Suitable for Portable Applications. *SID Digest*, 24, 2000. 27

[35] J. C. Jones and G. P. Bryan-Brown. Low cost zenithal bistable display with improved white state. *SID Digest*, 41, 2010. 28

[36] R. M. Amos, G. P. Bryan-Brown, E. L. Wood, J. C. Jones, and P. T. Worthing. Embossing method and apparatus, 2010. 28

[37] J. C. Jones. The Zenithal Bistable Display: From concept to consumer. *Journal of the Society for Information Display*, 16(1):143, 2008. 28, 33

[38] G. P. Bryan-Brown, D. R. E. Walker, and J. C. Jones. Controlled grating replication for the ZBD technology. *SID Digest*, 40, 2009. 28

[39] J. C. Jones, P. Worthing, G. P. Bryan-brown, and E. Wood. Transflective and Single Polariser Reflective Zenithal Bistable Displays. *SID Digest*, pages 190–193, 2003. 29, 112

[40] T. J. Spencer, C. M. Care, R. M. Amos, and J. C. Jones. Zenithal bistable device: Comparison of modeling and experiment. *Physical Review E*, 82:021702–1 – 021702–13, 2010. 30, 31, 33, 50, 71, 104

146

[41] S. A. Jones, J. Bailey, D. Walker, G. P. Bryan-Brown, and J. C. Jones. Method for tuneable homeotropic anchoring at micro-structures in liquid crystal devices. *Langmuir*, 2018. 31, 33, 53, 86, 104

[42] S. P. McBride and B. M. Law. Viscosity-dependent liquid slip at molecularly smooth hydrophobic surfaces. *Physical Review E - Statistical, Nonlinear, and Soft Matter Physics*, 80(6):2–5, 2009. 32, 65

[43] D. C. Zografopoulos, R. Beccherelli, and E. E. Kriezis. Beam-splitter switches based on zenithal bistable liquid-crystal gratings. *Physical Review E*, 90:1–8, 2014. 32

[44] D. C. Zografopoulos and E. E. Kriezis. Switchable beam steering with zenithal bistable liquid-crystal blazed gratings. *Optics Letters*, 39(20):5842–5845, 2014. 32

[45] D. C. Zografopoulos, Goran I., E. E. Kriezis, and R. Beccherelli. A switchable circular polarizer based on zenithal bistable liquid crystal gratings. *J. Phys. D: Appl. Phys.*, 49, 2016. 32

[46] D. C. Zografopoulos, E. E. Kriezis, and R. Beccherelli. Design of Switchable Guided-Mode Resonant Filters in Zenithal-Bistable Liquid-Crystal Gratings. *IEEE Photonics Technology Letters*, 29(16):1367–1370, 2017. 32

[47] S. E. Day, E. Willman, R. James, and F. A. Fernandez. Defect loops in the zenithal bistable display. *SID Digest*, 2008. 33, 70, 71

[48] ASTM D2240-15e1, Standard Test Method for Rubber Property - Durometer Hardness, 2015. 39

[49] N. A. Clark and S. T. Lagerwall. Submicrosecond bistable electro-optic switching in liquid crystals. *Applied Physics Letters*, 36(11):899–901, 1980. 54

[50] J. Xue, N. A. Clark, and M. R. Meadows. Surface orientation transitions in surface stabilised ferroelectric liquid crystal structures. *Applied Physics Letters*, 53, 1988. 54

NOTES AND REFERENCES

[51] J. G. Fonseca, P. Charue, and Y. Galerne. Zenithal anchoring angle and anchoring strength on oxidised silane plates. *Mol. Cryst. Liq. Cryst.*, 329, 1999. 54

[52] H. Yokoyama. Surface anchoring of nematic liquid crystals. *Mol. Cryst. Liq. Cryst.*, 165, 1988. 54

[53] H Yokoyama. A novel method for determining the anchoring energy function at a nematic liquid crystal-wall interface from director distortions at high fields. *J. Appl. Phys.*, 57(10):4520, 1985. 54

[54] J. G. Fonseca and Y. Galerne. Simple method for measuring the azimuthal anchoring strength of nematic liquid crystals. *Appl. Phys. Lett.*, 79, 2001. 54

[55] M. Vilfan and M. Copci. Azimuthal and zenithal anchoring of nematic liquid crystals. *Phys. Rev. E*, 68, 2003. 54

[56] J. S. Gwag, J. Yi, and J. H. Kwon. Determination of actual surface azimuthal anchoring strength using a wedge-shaped liquid crystal cell. *Opt. Lett.*, 35, 2010. 54

[57] L. M. Blinov, M. I. Barnik, H. Ohoka, M. Ozaki, and K. Yoshino. Surface and flexoelectric polarization in nematic and smectic a phases of liquid crystal 4-octyloxy-4'-cyanobiphenyl. *Jap. J. App. Phys. 1*, 40(8):5011–5018, 2001. 54

[58] R. Basu, A. Garvey, and D. Kinnamon. Effects of graphene on electro-optic response and ion-transport in a nematic liquid crystal. *J. Appl. Phys.*, 117:074301, 2015. 54

[59] G.-Y. Jung, Z. Li, W. Wu, Y. Chen, D. L. Olynick, S.-Y. Wang, W. M. Tong, and R. S. Williams. Vapour-phase self-assembled monolayer for improved mold release in nanoimprint lithography. *Langmuir*, 21, 2005. 62

[60] L. Doudevski, W. A. Hayes, and D. K. Schwartz. Submonolayer island nucleation and growth kinetics during self-assembled monolayer formation. *Phys. Rev. Lett*, 81, 1998. 63

[61] A. Kanta, R. Sedev, and J. Ralston. The formation and stability of self-assembled monolayers of octadecylphosphonic acid on titania. *Colloids Surf., A*, 291, 2006. 63

[62] E. J. Willman. *Three-dimensional finite element modelling of liquid crystal electro-hydrodynamics.* PhD thesis, University College London, 2008. 70

[63] E. Willman, F. A. Fernández, R. James, and S. E. Day. Switching Dynamics of a Post-Aligned Bistable Nematic Liquid Crystal Device. *Journal of Display Technology*, 4(3):276–281, 2008. 70

[64] T. J. Spencer and C. M. Care. Lattice Boltzmann scheme for modeling liquid-crystal dynamics: Zenithal bistable device in the presence of defect motion. *Physical Review E - Statistical, Nonlinear, and Soft Matter Physics*, 2006. 72

[65] T. Takahashi, S. Hashidate, H. Nishjou, and M. Usui. Novel measurement method for flexoelectric coefficients of nematic liquid crystals. *Jpn. J. Appl. Phys.*, 37, 1998. 97

[66] C. Kischka, S. J. Elston, and E. P. Raynes. Measurement of the Sum (e 1 + e 3) of the Flexoelectric Coefficients e 1 and e 3 of Nematic Liquid Crystals using a Hybrid Aligned Nematic (HAN) cell. *Mol. Cryst. Liq. Cryst.*, 494:93–100, 2008. 97

[67] C. Kischka, L. A. Parry-Jones, S. J. Elston, and E. P. Raynes. Measurement of the flexoelectric coefficients e 1 and e 3 in nematic liquid crystals. *Mol. Cryst. Liq. Cryst.*, 480, 2008. 97

[68] A. Jakli, J. Harden, and N. Eber. *Flexoelectricity of bent core molecules.* World Scientific, 2012. 97, 98

[69] J. Harden, B. Mbanga, N. Eber, K. Fodor-Csorba, S. Sprunt, J. T. Gleeson, and A. Jakli. Giant flexoelectricity of bent-core nematic liquid crystals. *Phys. Rev. Lett.*, 97, 2006. 98

149

NOTES AND REFERENCES

[70] S. Kaur, V. P. Panov, C. Greco, A. Ferrarini, V. Gortz, J. W. Goodby, and H. F. Gleeson. Flexoelectricity in an oxadiasole bent-core nematic liquid crystal. *Appl. Phys. Lett.*, 105, 2014. 98

[71] H. J. Coles, M. J. Clarke, S. M. Morris, B. J. Broughton, and A. E. Blatch. Strong flexoelectric behaviour in bimesogenic liquid crystals. *J. Appl. Phys.*, 99, 2005. 98

[72] M. Cestari, E. Frezza, A. Ferrarini, and G. R. Luckhurst. Crucial role of molecular curvature for the bend elastic and flexoelectric properties of liquid crystals: mesogenic dimers as a case study. *J. Mater. Chem.*, 21, 2011. 98, 105

[73] A. Varanytsia and L-C. Chien. Giant flexoelectro-optic effect with liquid crystal dimer CB7CB. *Sci. Rep.*, 7, 2017. 98

[74] J. W. Emsley, M. Lelli, A. Lesage, and G. R. Luckhurst. A comparison of the conformational distributions of the achiral symmetric liquid crystal dimer CB7CB in the achiral nematic and chiral twist-bend nematic phases. *J. Phys. Chem. B*, 117, 2013. 98

[75] N. Sebastian, B. Robles-Hernandez, S. Diez-Berart, J. Salud, G. R. Luckhurst, D. A. Dunmur, D. O. Lopez, and M. R. de la Fuente. Distinctive dielectric properties of nematic liquid crystal dimers. *Liq. Cryst.*, 44, 2016. 98

[76] D. A. Paterson, J. P. Abberley, W. T. A. Harrison, J. M. D. Storey, and C. T. Imrie. Cyanobiphenyl-based liquid crystal dimers and the twist-bend nematic phase. *Liq. Cryst.*, 44, 2017. 98

[77] N. Trbojevic, D. J. Read, and M. Nagaraj. Dielectric properties of liquid crystalline dimer mixtures exhibiting the nematic and twist-bend nematic phases. *Phys. Rev. E*, 96, 2017. 98

[78] M. R. Dodge, C. Rosenblatt, R. G. Petschek, M. E. Neubert, and M. E. Walsh. Bend elasticity of mixtures of v-shaped molecules in ordinary nematogens. *Phys. Rev. E.*, 62, 2000. 105

[79] M. R. Dodge, R. G.Petschek, C. Rosenblatt, M. E. Neubert, and M. E. Walsh. Light scattering investigation above the nematic-smectic-A phase transition in binary mixtures of calamitic and bent-core mesogens. *Phys. Rev. E.*, 68, 2003. 105

[80] P. Sathyanarayana, B. K. Sadashiva, and S. Dhara. Splay-bend elasticity and rotational viscosity of liquid crystal mixtures of rod-like and bent-core liquid crystals. *Soft Matter*, 7, 2012. 105

[81] S. Kaur, L. Tian, H. Liu, C. Greco, A. Ferrarini, J. Seltmann, M. Lehmann, and H. F. Gleeson. The elastic and optical properties of a bent-core thiadiazole nematic liquid crystal: the role of the bend angle. *J. Mater. Chem. C*, 2, 2013. 108

[82] S. Srigengan, M. Nagaraj, A. Ferrarini, R. Mandle, S. J. Cowling, M. A. Osipov, G. Pajak, J. W. Goodby, and H. F. Gleeson. Anomalously low twist and bend elastic constants in an oxadiazole-based bent-core nematic liquid crystal and its mixtures; contributions of spontaneous chirality and polarity. *J. Mater. Chem. C*, 6, 2018. 108

[83] C. Hedlund, H.-O. Blom, and S. Berg. Microloading effect in reactive ion etching. *Journal of Vacuum Science and Technology A*, 12, 1994. 116

[84] B. Wu, A. Kumar, and S. Pamarthy. High aspect ratio silicon etch: a review. *J. Appl. Phys.*, 2010. 136

[85] X. Li. Metal assisted chemical etching for high aspect ratio nanostructures: A review of characteristics and applications in photovoltaics. *Current opinion in solid state and materials science*, 16, 2012. 136